University of Alberta

THERMAL MANAGEMENT STRATEGIES

FOR MICROFLUIDIC DEVICES

by

Viet Nguyen Hoang

A thesis submitted to the Faculty of Graduate Studies and Research
in partial fulfillment of the requirements for the degree of

Master of Science

Department of Electrical & Computer Engineering

Edmonton, Alberta
Spring 2008

Library and
Archives Canada

Published Heritage
Branch

395 Wellington Street
Ottawa ON K1A 0N4
Canada

Bibliothèque et
Archives Canada

Direction du
Patrimoine de l'édition

395, rue Wellington
Ottawa ON K1A 0N4
Canada

Canada

ABSTRACT

Microfluidic lab-on-a-chip technology can be designed to overcome the cost and practicality barriers currently limiting conventional genetic analysis techniques to the laboratory setting. Since accurate temperature control is critical for several of these techniques, the goal of this project is to design, fabricate and test a more effective microfluidic thermal management scheme. To improve amenability to integration, a single resistive element is used to perform both heating and temperature sensing simultaneously, rather than using two separate elements, effectively halving the interfacing requirements of the thermal module. The developed approach to thermal management is applied mainly in the context of microchip-based polymerase chain reaction (a central step in performing genetic tests), though other applications, such as thermoelectrically-actuated microvalves, are explored as well. The thermal module is well characterized and can serve as a building block for developing practical microchip-based diagnostic tools suitable for routine and widespread use in the clinical setting.

To my parents
Thank you for your unending love and support

ACKNOWLEDGEMENTS

TABLE OF CONTENTS

List of Tables

List of Figures

List of Abbreviations

ACDC   Alberta Cancer Diagnostics Consortium

AML   Applied Miniaturization Laboratory

β2M   β2 Microglobulin

BSA   Bovine Serum Albumin

CCD   Charge-Coupled Device

CE   Capillary Electrophoresis

cDNA   Complementary Deoxyribonucleic Acid

DNA   Deoxyribonucleic Acid

dNTP   Deoxyribonucleotide triphosphate

FE   Finite Element

FEM   Finite Element Modeling

FISH   Fluorescence In-Situ Hybridization

FWHM   Full Width at Half Maximum

HA   Heteroduplex Analysis

LED   Light Emitting Diode

LIBS   Laser Induced Breakdown Spectroscopy

LOC   Lab-on-a-chip

mRNA   Messenger RNA

μTK   Microfluidic Tool Kit

NASBA   Nucleic Acid Sequence-Based Amplification

PCR   Polymerase Chain Reaction

PD   Proportional-Derivative

PDE   Partial Differential Equation

PDMS	Polydimethylsiloxane
PI	Proportional-Integral
Pt	Platinum
RNA	Ribonucleic Acid
RT	Reverse Transcription
SSCP	Single-Stranded Conformational Polymorphism
TCR	Temperature Coefficient of Resistivity
Ti	Titanium
TiW	Tungsten titanium alloy
TLC	Thermochromic Liquid Crystal
TTK	Tricorder Tool Kit

List of Notations

α	Temperature coefficient of resistance
B_{max}	Maximum relative blue intensity reached throughout a TLC run
ρ	Resistivity
t	Time
T	Temperature
T_c	Temperature at the reaction chamber
T_{ext}	Room temperature
T_h	Temperature at the resistive element
T_s	Temperature at the top surface of the microchip (above the chamber)
T_{sink}	Temperature of the heat sink

Chapter 1

Introduction to microchip-based genetic amplification

1.1 INTRODUCTION

DNA is often referred to as the blueprint or the recipe book of a cell since it contains the vital instructions for producing all the proteins and enzymes a cell requires in order to live and function. If DNA is damaged, these instructions can be lost or altered, resulting in mutations that lead to abnormal changes in the functions of the cell. Certain mutations can initiate cancer, a disease that claims many lives every year. Cancerous cells often contain abnormalities in certain key genes. Hence, the ability to study DNA is crucial to understanding and dealing with cancer. Many biomedical techniques have been developed for the processing and analysis of DNA. These techniques fall under a field known as molecular biology and have allowed researchers to make much progress in uncovering the mechanisms behind the development of cancer. However, in their current form, their complexity and high cost (both in time and in money) make them impractical for use outside of the laboratory environment. Nonetheless, if they can be brought into clinical setting, these DNA analyzing techniques can potentially be very powerful tools for diagnosing cancer and monitoring its progression. With information from the DNA of their patients, doctors would be able to identify those who have a high risk of developing cancer and also tailor more specific and effective treatments for those suffering from cancer.

Lab-on-a-chip technology is a relatively new and rapidly advancing field that aims to make DNA analyzing techniques more practical for widespread use by miniaturizing them. A similar transformation has already occurred for computers. The development of the transistor and of microchip technology has allowed computer systems to evolve from the early complicated, room-sized machines to the much more practical, powerful, and user-friendly forms of today, such as the personal desktop computer, the laptop, and the hand-held PDA (personal digital assistant). Computers now have a wide and growing range of roles and are inexpensive enough to be used by many people in their every day lives. In a similar manner, adapting DNA analyzing techniques to microfluidic chip (microchip)-based platforms promises to make them much faster, less labour intensive, less expensive, and possibly even more powerful than their conventional forms.

One of the most important molecular biology techniques for analyzing DNA is the polymerase chain reaction (PCR). It is essentially a technique used to make a large number of copies of DNA. Since obtained samples often contain too little DNA to be detected or analyzed, PCR is performed on them to greatly increase the amount of DNA available, allowing them to be studied. Hence, PCR is a crucial step to many DNA tests and has proven to be an invaluable tool for medical science, helping to reveal many of the mysteries behind the mechanisms of cancer and other genetic diseases. Additionally, PCR has also played a major role in forensics, genome sequencing, and the study of ancient DNA [1-3].

PCR consists of preparing a sample consisting of the target DNA to be replicated along with various buffers and reagents. This PCR sample is then thermally cycled through three temperature stages repeatedly: denaturation, primer annealing, and extension. DNA consists of two complementary strands that are usually bound to each other like a zipper (Figure 1-1a). Both strands carry the recipes used by the cell to produce proteins, but when the two strands are bound together, this information is not accessible in the same way a recipe book cannot be read if it is closed. During denaturation, the first stage of PCR, the PCR sample is heated up to 94°C to denature, or "unzip", the paired DNA strands, separating them to allow access to the information they carry (Figure 1-1b). In the next PCR stage, primer annealing, the temperature of the PCR sample is lowered to allow short strands

of DNA called primers to attach to the separated DNA strands (Figure 1-1c). These primers, which are included in the PCR sample, are designed and synthesized such that they attach to the DNA only at specifically chosen places. The temperature at which they bind to the DNA can vary, but is typically around 55°C-65°C. The primers act like bookmarks, allowing researchers to choose and mark the part of the DNA they would like to read and copy. Once the primers are bound to the DNA strands, the temperature of the PCR sample is raised to 72°C and the third stage, extension, takes place. In this last stage, DNA polymerase, a replicating enzyme included in the PCR sample, copies the separated DNA strands by assembling new, complementary DNA strands that attach to the original strands (Figure 1-1d). The original DNA "zipper" is therefore duplicated (Figure 1-1e), with the new strands made from nucleotides (DNA building blocks) supplied in the PCR sample. The PCR sample is

Figure 1-1. Steps involved in PCR.

then heated back up to 94°C to unzip the newly made DNA, and the cycle of three temperature stages is repeated to copy the DNA again.

Typically, thirty to forty PCR cycles are used, exponentially increasing the amount of DNA in the sample. Ideally, each cycle doubles the amount of target DNA in the sample, but the actual efficiency and yield are lower and depend on many variables such as the quality and concentration of the reagents as well as the temperature and duration of each PCR stage [1]. Accurate temperature control is crucial for high quality PCR. For efficient and accurate PCR, the temperature distribution in the PCR sample must be kept as uniform as possible. Variations of more than 1°C can cause errors to be made during the copying process and

thus give incorrect results [4, 5]. Temperature overshoots can lead to faster deactivation of the polymerase or even boiling of the PCR sample, resulting in false negatives, while temperature undershoots can lead to primers binding to incorrect places (non-specific binding), amplifying the wrong DNA fragment. The temperature of the PCR sample must
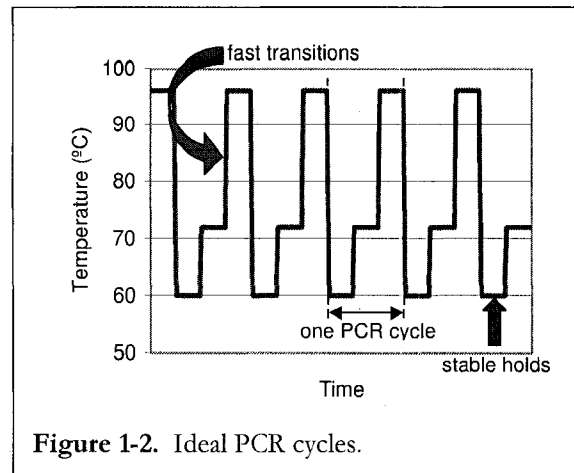
Figure 1-2. Ideal PCR cycles.

remain as constant as possible during each temperature stage, but rise or fall as quickly as possible during the transitions between them (Figure 1-2). Furthermore, PCR reagents, particularly the polymerase (half-life of ~40 min. at ~95°C), gradually degrade over time [4]. Hence, by shortening the time required to run the PCR, fast temperature ramping rates can also increase its yield.

Conventionally, PCR is performed by preparing the PCR sample in small polypropylene tubes and using a programmable, desktop sized Peltier-based system to do the temperature cycling. These thermal cyclers can typically hold up to 96 tubes and perform PCR on them simultaneously. However, due to their large size and hence heat capacity, heating and cooling rates of only about 1-2°C/s can be achieved. PCR using these thermal cyclers therefore typically takes about 1.5 to 3 hours to complete. Furthermore, studies have revealed that PCR results can vary greatly between different tube positions in a typical thermal cycler since the temperature distribution in the thermal cycler is not very uniform [6]. Large temperature differences of up to 10°C, which can greatly hinder PCR accuracy and efficiency, have also been observed inside the PCR tubes themselves [1]. Nevertheless, this conventional method of performing PCR has been used extensively in molecular biology research. However, since it is costly (relatively expensive reagents), time-consuming (requires hours), and labor-intensive (requires well-trained personnel), conventional PCR is rather impractical for routine and widespread use outside of the laboratory setting [3].

4

Miniaturizing the thermal cycler into a chip-based platform the size of a microscope slide (referred to interchangeably as a microfluidic chip or a microchip in this thesis) entails several advantages [1-3, 7]. The much smaller size of on-chip PCR systems makes it easier to maintain highly uniform PCR sample temperatures. Since the heat capacity is also lowered, higher heating and cooling rates are made possible as well. Due to this faster speed and more accurate temperature control, chip-based thermal cyclers can potentially perform PCR with higher accuracy and yield than their conventional desktop sized counterparts [4]. In addition to improving performance, the smaller size allows on-chip PCR to use smaller amounts of reagents, while the faster speed translates into less time consuming tests. On-chip PCR systems can also run on much less power than conventional systems. These cost reducing advantages are key to rendering PCR practical enough to be available and widely used, for example, in the clinical setting as a powerful tool for diagnosing cancer, monitoring disease progression, and tailoring more effective patient-specific treatments.

1.2 REVIEW OF ON-CHIP PCR

A number of research groups have developed on-chip PCR systems in an effort to make PCR feasible for use outside of the laboratory setting. Two general design approaches have been used, termed space domain PCR and time domain PCR by Kricka and Wilding [3]. In space domain PCR, thermal cycling is performed by actively moving the PCR sample through different fixed temperature zones [8-15]. In contrast, in time domain PCR, the PCR sample is kept stationary in a reaction chamber whose temperature is dynamically cycled [16-40]. Space domain PCR has the advantage of faster thermal cycling since temperatures in the system do not have to be changed. On the other hand, time domain PCR systems can be made much smaller and are thus more suitable for array-based systems that can perform PCR on a large number of samples in parallel.

Particularly in earlier demonstrations of on-chip PCR, silicon was a common choice of substrate since it offers flexibility in terms of fabrication as well as a high thermal

conductivity that allows for rapid heat transfer [9-11, 14, 16-18, 21, 24-26, 29, 32, 35]. To ensure localized heating though, thermally isolating structures such as trenches [11, 14, 18, 24, 32] and membranes [25, 26, 29, 32] must be used. These structures greatly reduce the parasitic thermal capacitance of the system, leading to substantially lower power consumption and faster temperature ramping rates. Finite element analysis is often used to optimize their design, and heating rates as high as 80°C/s have been achieved [25]. However, despite its advantages for PCR, silicon is not always a suitable material for other molecular biology techniques used in conjunction with PCR to process and analyze DNA. For example, capillary electrophoresis (CE), a common and highly effective technique for analyzing DNA after it has been amplified by PCR, involves the use of high electric fields to manipulate DNA and the use of fluorescence at visible wavelengths to detect it. Silicon will not sustain such high electric fields and is opaque to visible wavelengths, and as a result, is rather unsuitable for on-chip CE [2, 20].

On the other hand, glass is much more suitable for CE as it can withstand high electric fields and is transparent over a wide range of wavelengths, including the visible range. Hence, as the direction for on-chip PCR shifted towards integration rather than speed, more recent demonstrations of on-chip PCR, and particularly PCR-CE systems, have been glass-based [8, 12-14, 19, 20, 22, 23, 27, 28, 31, 33, 34, 36-40]. Since glass is much less thermally conductive than silicon (~150 times), very fast temperature ramping rates are typically sacrificed for enhanced functional integration. Another advantage glass has over silicon is the fact that it is more compatible with a much wider range of molecular biology techniques, including PCR. The adsorption of polymerase to silicon can inhibit PCR, and therefore the PCR sample needs to be isolated from silicon, typically through the use of a thin layer of silicon dioxide [3, 9, 17, 21, 24-26, 29, 30, 32, 35]. Glass is therefore more suitable for on-chip PCR and lab-on-a-chip devices in general.

Nevertheless, it is important to note that fabrication processes can still render inherently PCR-friendly surfaces incompatible. For example, residual chromium from etch masks can still inhibit PCR [3]. Furthermore, the very high surface area to volume ratio of miniaturized on-chip PCR systems can lead to greatly increased surface adsorption of the PCR sample

components, resulting in unsuccessful replication. This problem is typically remedied by adding a protein such as bovine serum albumin (BSA) to the PCR sample to bind preferentially to the walls of the chip and thus prevent the PCR components from binding [3, 17, 20, 30, 34, 39, 40].

Polymers such as polyimide, SU-8, and polydimethylsiloxane (PDMS) have also proven to be useful materials in on-chip PCR devices since they are relatively inexpensive, PCR compatible, and simple in terms of fabrication processes [2, 3, 10, 13, 16, 22, 23, 28, 31, 33, 36-40]. As a result of their flexible nature, they also lend themselves well to forming integrated microfluidic valves and pumps for manipulating and confining the PCR sample.

Thermal cycling in on-chip PCR systems has been accomplished most commonly using Peltier cells [8, 9, 17, 19-22, 30, 39, 40], integrated thin film resistive heaters [10-16, 18, 23-26, 28-35, 38], and infrared lasers [27, 36, 37]. Of these, the thin film resistive heater, typically made of polysilicon or platinum, is quickly becoming the preferred choice as a result of its high performance and simple implementation. Compared to the conventionally used Peltier cell, thin film resistive heaters operate much faster and much more efficiently in terms of power consumption as a result of their much smaller size and hence thermal inertia [24, 30]. Furthermore, thin film resistive heaters are more versatile in terms of design, allowing researchers to tailor the shape of their heater for optimum temperature uniformity and precise, localized heating. Finite element modeling is typically used for such purposes. Since bulk heating is avoided, thin film resistive heaters also readily lend themselves to array-based systems where a large number of reactions can be run in parallel, but with differing thermal cycling profiles [31].

Thin metal films are also typically used as resistive temperature sensors for monitoring and providing feedback on the temperature of the PCR sample [11, 12, 14-16, 18, 23-26, 28-35, 38]. The ability to place such sensors in close proximity with the reaction chamber allows for improved accuracy in temperature control. Platinum is a particularly suitable material since its resistivity exhibits a strong linear dependence on temperature. The temperature coefficient of resistance of platinum is also relatively high, giving it a good sensitivity to

temperature [2]. As for determining and evaluating temperature uniformity, infrared photography [3] and thermochromic liquid crystals (liquid crystals that change color with temperature) [3, 10, 19, 35] have been used. Both these techniques allow the temperature distribution in the on-chip PCR system to be characterized with minimal perturbations.

Although successful on-chip PCR devices have been demonstrated [2, 3, 7-40], PCR is usually only one of many steps involved in carrying out a test on DNA. Other techniques are required to extract and prepare the DNA sample before performing PCR and to detect and analyze the DNA after performing PCR. Many research groups are currently miniaturizing these other techniques onto chip-based platforms as well in order to obtain similar improvements to those outlined here for PCR [2, 3, 7, 16, 20, 22, 27, 31, 36-38]. Ultimately, the goal is to combine all the techniques required to carry out a DNA analysis onto a single chip. Such a system would be highly beneficial since the DNA sample would remain inside the chip during the whole test, reducing the possibility of contamination. The increased automation would also eliminate much of the tedious labor usually involved with DNA analyzing techniques and thus enhance their practicality. Clearly, miniaturization is the key to making DNA analysis practical for widespread use. Within the next decade, lab-on-a-chip devices will become powerful tools in the clinical setting, especially in the fight against cancer and other genetic diseases.

1.3 OUTLINE OF PROPOSED RESEARCH

The objective of this project was to design, fabricate, and test an on-chip PCR system using a single patterned platinum thin film as both a heater for thermal cycling and a temperature sensor. As discussed earlier, to successfully perform PCR, the system must be able to provide fast temperature transients between the three PCR temperature stages, but still hold the temperature of the sample as constantly as possible at each stage. The PCR sample must also be heated as uniformly as possible. Furthermore, in order to use the platinum thin film simultaneously as a heater and as a temperature sensor, the temperature distribution of the thin film must be kept uniform as well so that its resistance accurately reflects its

8

temperature. The relationship between the temperature of the PCR sample and the temperature of the platinum thin film must also be well characterized in order to properly control the temperature of the PCR sample indirectly using feedback from the temperature of the thin film. The definitive test for the on-chip PCR system was to demonstrate reliably successful genetic amplification.

Though a number of on-chip PCR systems using thin film heaters have been developed, they have all required a second, separate thin film for temperature sensing. The thin film heater itself typically does not maintain a uniform temperature distribution when it undergoes resistive heating, and is therefore unsuitable for use as a temperature sensor. Nonetheless, if the thin film heater could be designed such that it does heat up uniformly, the need to incorporate a second thin film for temperature sensing would be eliminated. As a result, interfacing to the microchip would require half as many electrical connections, improving its amenability to integration. This advantage becomes a considerable one for array-based systems designed to perform PCR on a large number of samples in parallel, or for systems integrating numerous thermal modules (not necessarily PCR chambers).

As discussed earlier, the miniaturization of PCR leads to lower costs, reduced power consumption, improved performance, more automation, and higher portability, rendering it more feasible for widespread use outside of the laboratory setting. On-chip PCR can be a very powerful and useful tool for battling cancer, particularly if it is integrated with other molecular biology techniques (e.g. for sample preparation and analysis). In this context, additional goals were considered for the design of the developed microfluidic thermal module. The module should be thermally independent of its surroundings so that it may be placed in different microchip designs without greatly affecting its own operation or the operation of other integrated components. It should also be readily scalable in size since further miniaturization is expected to reduce power consumption and increase thermal transition speeds, and would also lead to higher device densities. With these considerations, the developed microfluidic thermal module becomes a highly versatile building block that is readily adaptable for use in more complex microfluidic lab-on-a-chip systems in the future.

9

1.4 REFERENCES

[1] de Mello, A.J., "DNA amplification: does 'small' really mean 'efficient'?" *Lab on a Chip*, 2001. **1**: p. 24N-29N.

[2] Lagally, E.T. and R.A. Mathies, "Integrated genetic analysis microsystems", *Journal of Applied Physics D: Applied Physics*, 2004. **37**: p. R245-R261.

[3] Kricka, L.J. and P. Wilding, "Microchip PCR", *Analytical and Bioanalytical Chemistry*, 2003. **377**: p. 820-825.

[4] Wittwer, C.T. and D.J. Garling, "Rapid cycle DNA amplification: time and temperature optimization", *Biotechniques*, 1991. **10**(1): p. 76-83.

[5] Sadler, D.J., R. Changrani, P. Roberts, C.-F. Chou, and F. Zenhausern, "Thermal management in bioMEMS: temperature control for ceramic-based PCR and DNA detection devices", *IEEE Transactions on Components and Packaging Technology*, 2003. **26**(2): p. 309-316.

[6] Saunders, G.C., J. Dukies, H.C. Parkes, and J.H. Cornett, "Interlaboratory study on thermal cycler performance in controlled PCR and random amplified polymorphic DNA analyses", *Clinical Chemistry*, 2001. **47**(1): p. 47-55.

[7] Erickson, D. and D. Li, "Integrated microfluidic devices", *Analytica Chimica Acta*, 2004. **507**: p. 11-26.

[8] Kopp, M.U., A.J. de Mello, and A. Manz, "Chemical amplification: Continuous-flow PCR on a chip", *Science*, 1998. **280**(5366): p. 1046-1048.

[9] Zhang, Q., W. Wang, H. Zhang, and Y. Wang, "Temperature analysis of continuous-flow micro-PCR based on FEA", *Sensors and Actuators B*, 2002. **82**: p. 75-81.

[10] Liu, J., M. Enzelberger, and S. Quake, "A nanoliter rotary device for polymerase chain reaction", *Electrophoresis*, 2002. **23**(10): p. 1531-1536.

[11] Bu, M., T. Melvin, G. Ensell, J.S. Wilkinson, and A.G.R. Evans, "Design and theoretical evaluation of a novel microfluidic device to be used for PCR", *Journal of Micromechanics and Microengineering*, 2003. **13**: p. S125-S130.

[12] Li, S. and S. Chen, "Design, simulation, and microfabrication of a heat-conduction DNA chip with integrated microheaters", *Journal of Manufacturing Processes*, 2004. **6**(1): p. 81-87.

[13] Xiaoyu, J., N. Zhiqiang, C. Wenyuan, and Z. Weiping, "Polydimethylsiloxane (PDMS)-based spiral channel PCR chip", *Electronics Letters*, 2005. **41**(16): p. 890-891.

[14] Wang, W., Z.-X. Li, R. Luo, S.-H. Lu, A.-D. Xu, and Y.-J. Yang, "Droplet-based micro oscillating-flow PCR chip", *Journal of Micromechanics and Microengineering*, 2005. **15**: p. 1369-1377.

[15] Guttenberg, Z., H. Muller, H. Habermuller, A. Geisbauer, J. Pipper, J. Felbel, M. Kielpinski, J. Scriba, and A. Wixforth, "Planar chip device for PCR and hybridization with surface acoustic wave pump", *Lab on a Chip*, 2005. **5**: p. 308-317.

[16] Woolley, A.T., D. Hadley, P. Landre, A.J. deMello, R.A. Mathies, and M.A. Northrup, "Functional integration of PCR amplification and capillary electrophoresis in a microfabricated DNA analysis device", *Analytical Chemistry*, 1996. **68**(23): p. 4081-4086.

[17] Taylor, T.B., E.S. Winn-Deen, E. Picozza, T.M. Woudenberg, and M. Albin, "Optimization of the performance of the polymerase chain reaction in silicon-based microstructures", *Nucleic Acids Research*, 1997. **25**(15): p. 3164-3168.

[18] Poser, S., T. Schulz, U. Dillner, V. Baier, J.M. Kohler, D. Schimkat, G. Mayer, and A. Siebert, "Chip elements for fast thermocycling", *Sensors and Actuators A*, 1997. **62**: p. 672-675.

[19] Chaudhari, A.M., T.M. Woudenburg, M. Albin, and K.E. Goodson, "Transient liquid crystal thermometry of microfabricated PCR vessel arrays", *Journal of Microelectromechanical Systems*, 1998. **7**(4): p. 345-355.

[20] Khandurina, J., T.E. McKnight, S.C. Jacobson, L.C. Waters, R.S. Foote, and J.M. Ramsey, "Integrated system for rapid PCR-based DNA analysis in microfluidic devices", *Analytical Chemistry*, 2000. **72**(13): p. 2995-3000.

[21] Lin, Y.C., M.Y. Huang, K.C. Young, T.T. Chang, and C.Y. Wu, "A rapid micro-polymerase chain reaction system for hepatitis C virus amplification", *Sensors and Actuators B-Chemical*, 2000. **71**(1-2): p. 2-8.

[22] Hong, J.W., T. Fujii, M. Seki, T. Yamamoto, and I. Endo, "Integration of gene amplification and capillary gel electrophoresis on a polydimethylsiloxane-glass hybrid microchip", *Electrophoresis*, 2001. **22**(2): p. 328-333.

[23] Lee, C.-Y., G.-B. Lee, H.-H. Liu, and F.-C. Huang, "MEMS-based temperature control systems for DNA amplification", *International Journal of Nonlinear Sciences and Numerical Simulation*, 2002. **3**: p. 215-218.

[24] Yoon, D.S., Y.-S. Lee, Y. Lee, H.J. Cho, S.W. Sung, W. Oh, J. Cha, and G. Lim, "Precise temperature control and rapid thermal cycling in a micromachined DNA polymerase chain reaction chip", *Journal of Micromechanics and Microengineering*, 2002. **12**: p. 813-823.

[25] Zou, Q., U. Sridhar, Y. Chen, and J. Singh, "Miniaturized independently controllable multichamber thermal cycler", *IEEE Sensors Journal*, 2003. **3**(6): p. 774-780.

[26] Zhao, Z., Z. Cui, D. Cui, and S. Xia, "Monolithically integrated PCR biochip for DNA amplification", *Sensors and Actuators A*, 2003. **108**: p. 162-167.

[27] Ferrance, J.P., Q. Wu, B. Giordano, C. Hernandez, Y. Kwok, K. Snow, S. Thibodeau, and J.P. Landers, "Developments towards a complete micro-total analysis system for Duchenne muscular dystrophy diagnosis", *Analytica Chimica Acta*, 2003. **500**: p. 223-236.

[28] El-Ali, J., I.R. Perch-Nielsen, C.R. Poulsen, D.D. Bang, P. Telleman, and A. Wolff, "Simulation and experimental validation of a SU-8 based PCR thermocycler chip with integrated heaters and temperature sensors", *Sensors and Actuators A*, 2004. **110**: p. 3-10.

[29] Lee, D.-S., S.H. Park, H. Yang, K.-H. Chung, T.H. Yoon, S.-J. Kim, K. Kim, and Y.T. Kim, "Bulk-micromachined submicroliter-volume PCR chip with very rapid thermal response and low power consumption", *Lab on a Chip*, 2004. **4**: p. 401-407.

[30] Erill, I., S. Campoy, J. Rus, L. Fonseca, A. Ivorra, Z. Navarro, J. Plaza, J. Aguilo, and J. Barbe, "Development of a CMOS-compatible PCR chip: comparison of design and system strategies", *Journal of Micromechanics and Microengineering*, 2004. **14**: p. 1558-1568.

[31] Lagally, E.T., J.R. Scherer, R.G. Blazej, N.M. Toriello, B.A. Diep, M. Ramchandani, G.F. Sensabaugh, L.W. Riley, and R.A. Mathies, "Integrated portable genetic analysis microsystem for pathogen/infectious disease detection", *Analytical Chemistry*, 2004. **76**(11): p. 3162-3170.

[32] Yang, M., P. R., and M.A. Burns, "Cost-effective thermal isolation techniques for use on microfabricated DNA amplification and analysis devices", *Journal of Micromechanics and Microengineering*, 2005. **15**: p. 221-230.

[33] Liao, C., G. Lee, H. Liu, T. Hsieh, and C. Luo, "Miniature RT–PCR system for diagnosis of RNA-based viruses", *Nucleic Acids Research*, 2005. **33**(18): p. e156:3-7.

[34] Oh, K.W., C. Park, K. Namkoong, J. Kim, K.-S. Ock, S. Kim, Y.-A. Kim, Y.-K. Cho, and C. Ko, "World-to-chip microfluidic interface with built-in valves for multichamber PCR assays", *Lab on a Chip*, 2005. **5**: p. 845-850.

[35] Noh, J., S.W. Sung, M.K. Jeon, S.H. Kim, L.P. Lee, and S.I. Woo, "In situ thermal diagnostics of the micro-PCR system using liquid crystals", *Sensors and Actuators A*, 2005. **122**: p. 196-202.

[36] Easley, C.J., J.M. Karlinsey, and Landers J. P., "On-chip pressure injection for integration of infrared-mediated DNA amplification with electrophoretic separation", *Lab on a Chip*, 2006. **6**(5): p. 601-610.

[37] Easley, C.J., J.M. Karlinsey, J.M. Bienvenue, L.A. Legendre, M.G. Roper, S.H. Feldman, M.A. Hughes, E.L. Hewlett, T.J. Merkel, J.P. Ferrance, and J.P. Landers, "A fully integrated microfluidic genetic analysis system with sample-in-answer-out capability", *Proceedings of the National Academy of Sciences*, 2006. **103**(51): p. 19272-19277.

[38] Toriello, N.M., C.N. Liu, and R.A. Mathies, "Multichannel reverse transcription-polymerase chain reaction microdevice for rapid gene expression and biomarker analysis", *Analytical Chemistry*, 2006. **78**: p. 7997-8003.

[39] Kaigala, G.V., R.J. Huskins, J. Preiksaitis, X.L. Pang, L.M. Pilarski, and C.J. Backhouse, "Automated screening using microfluidic chip-based PCR and product detection to assess risk of BK virus-associated nephropathy in renal transplant recipients", *Electrophoresis*, 2006. **27**(19): p. 3753-3763.

[40] Van Dijken, J., G. Kaigala, J. Lauzon, A. Atrazhev, B.J. Taylor, T. Reiman, A.R. Belch, C.J. Backhouse, and L.M. Pilarski, "Microfluidic chips for detecting the t(4;14) translocation and monitoring disease during treatment using RT-PCR analysis of IgH-MMSET hybrid transcripts", *Journal of Molecular Diagnostics*, 2007. **9**(3): p. 358-367.

Chapter 2

Thermal management in microfluidic lab-on-a-chip devices using a single resistive element approach

2.1 INTRODUCTION

Molecular biology provides great insights into the nature of numerous diseases, but in its current form, it is often impractical for use outside of the laboratory setting due to high costs and complexity. The ongoing adaptation and integration of molecular biology techniques onto microchip platforms will render them substantially faster, increasingly automated, portable, and inexpensive, allowing molecular diagnostics to be used as routine tools in a clinical setting [1-3]. Numerous molecular biology protocols require precise and uniform heating while others require a more complex, rapidly varying temperature schedule (thermal cycling). We demonstrate the use of a novel thermal management method to measure and control the temperature within microfluidic devices for performing a genetic amplification reaction, the reverse-transcriptase polymerase chain reaction (RT-PCR). The work in this chapter is based on a manuscript in preparation.

PCR is an important technique widely used in molecular biology to substantially increase the amount of DNA present in a given sample so that it may be detected and analyzed using inexpensive detection technologies [4]. To perform PCR, the target DNA is combined with a mix of reagents and repeatedly cycled through distinct temperature stages. Accurate

temperature control, temperature uniformity, and rapid transitions between the temperature stages are all crucial for high yield PCR. From a thermal management standpoint, this thermal cycling is perhaps the most complex scenario, compared to most techniques that require a single temperature stage. To detect and analyze RNA, a reverse transcription (RT) incubation step is performed to transcribe the RNA into cDNA, which can then be amplified using PCR. A single-step RT-PCR can be performed, wherein the prepared sample includes both enzyme systems (for RT and for PCR) and undergoes temperature cycling for PCR immediately following the incubation required for RT.

Resistive thin film elements have emerged as one of the most common approaches for thermal management in microscale systems [5]. In comparison to Peltier cells, another widely used heating technique, resistive thin film heaters can operate and respond substantially faster while maintaining a much lower power consumption [6]. The infrared laser [7-9], microwave [10], and induction heating [11] approaches are also rapid means for temperature control, but resistive heating elements are more amenable to integration in portable systems due to their reduced size and minimal drive electronics and power requirements. Additionally, resistive elements are easily fabricated using standard, well-established microfabrication techniques, are versatile in design, and are readily integrated with microelectronics.

Thin metal films, in addition to acting as heating elements, can be used as temperature sensors to provide necessary feedback for controlling temperature [5]. Platinum has proven to be an excellent choice for such thin film temperature sensors since its resistivity exhibits a sensitive linear dependence on temperature (i.e. a large temperature coefficient of resistivity, TCR). It also remains more stable at higher temperatures than metals such as gold and silver, degrading only at temperatures above ~900°C [12]. It has therefore become by far the most common choice of material for thin film temperature sensors [2, 6]. For simplicity, platinum is also typically used for heater elements [13-21] (to avoid patterning different metals). However, since the superior temperature sensing properties of platinum are not required in a heating element, other less expensive and more easily patterned materials such as polysilicon [5, 22] and tungsten [23] have also been used.

15

In order to have the total resistance of a resistive element accurately reflect its temperature, the temperature distribution in the metal film must be uniform. Features such as sharp turns or notches on the element can restrict current flow and consequently produce greater localized resistive heating, resulting in hot spots. The geometry and environment surrounding the resistive element greatly affects its temperature distribution by influencing how heat is dissipated. Without adequate spacing between the resistive element and features such as the edges of the microchip, temperature uniformity cannot be maintained. Other design requirements, such as the need to have electrical leads that do not impose a significant resistive or thermal load, also limit how uniform the temperature on the resistive element can be. As a result, to our knowledge, two separate resistive thin film elements have always been implemented in microfluidic demonstrations of electrical temperature control: an active element to provide heating, and a passive element to sense temperature and provide feedback [6, 13-23]. Nonetheless, if the resistive thin film element could be designed to heat while maintaining a uniform temperature distribution, it would then be able to function simultaneously as both a heater and a sensor. Such a design would eliminate the need for the second resistive element and its accompanying electronics and connections, facilitating the interfacing of the microchip. This single resistive element approach would have significant advantages when implemented in highly miniaturized systems designed to integrate a large number of individual heating modules. Furthermore, it may allow for more rapid thermal responses and more accurate temperature sensing by allowing the heater/sensor to be placed closer to the chamber.

In the present work, finite element modeling (FEM) was used to design a microchip for performing genetic amplification (PCR or RT-PCR) using the single resistive element approach to thermal management. Glass/polymer-based devices (Figure 2-1a-b) were considered due to their suitability for integrating several important analytical molecular biology techniques such as capillary electrophoresis [2]. A relatively large reaction chamber size was chosen (~µl scale) to accommodate biochemical tests performed on clinical samples with low analyte concentration [24]. Since sharp turns tend to produce local hot spots, a circular single-ring geometry was chosen as a starting point for subsequent studies (Figure 2-1c). Electrode pads were designed such that the heater ring dominated the resistance of the

16

element and was thus the only part that undergoes significant resistive heating. Microchip and heating element geometries (dimensions shown in Figure 2-1c) were optimized to maintain temperature uniformity both on the resistive element (required for temperature sensing) and in reaction chamber (required for PCR).

Though the resistive element can act as a sensor, it measures its own temperature and not the temperature of the reaction chamber with which we are concerned. This fundamental issue is typical in PCR microchips since metals tend to inhibit PCR [3], preventing resistive temperature sensors from directly contacting the contents of the reaction chamber. As discussed by Iles et al. [25], no matter what the approach used to heat the

Figure 2-1. Representative a) two-layer and b) three-layer microchips considered in this study, as well as c) a representative single-ring resistive thin film element, illustrating the dimensions considered for optimization in this study.

microsystem, the measurement of temperature in microfluidic systems is challenging and the temperature of the sensor can differ significantly from that of the active fluidic volume. In silicon-based devices, this temperature offset is often smaller (~1°C) due to the high thermal conductivity of silicon, but in the much less thermally conductive glass-based devices, the temperature offset can be tens of degrees [17]. To cope with the large offset between chamber and measured temperatures in glass-based PCR devices, other research groups have needed to use a "dummy" chip with a temperature sensor inside the reaction chamber. Such dummy chips have either been used for calibration [13, 19] or run in parallel with the actual PCR to provide control feedback [8, 9].

17

Here, the relationship between the temperatures at the resistive element and at the reaction chamber in the steady-state was established and corroborated by using both experimental measurements and simulation. This relationship allowed the temperature of the reaction chamber to be controlled on the basis of measuring the temperature at the resistive element. During temperature transitions, since there was a substantial delay in the response of the chamber temperature to changes at the resistive element, we employed heating and cooling stages wherein either maximal or minimal power is applied to the element to achieve faster temperature ramping rates in the chamber. To show the effectiveness of this approach, we demonstrate genetic amplification (RT-PCR), which requires precision in temperature during thermal cycling. To our knowledge, this is the first implementation of the single resistive element approach to thermal management within a microfluidic chip.

2.2 FINITE ELEMENT MODELING

Before discussing our simulations, it is useful to consider some simpler situations that provide insight. 1) A *uniform & insulated thin chip:* Let us first consider an extremely thin microchip containing a circular metal ring that is used as an electrical heater. The ring is far from the edges of the chip and the region inside the ring is thermally insulated on both the top and bottom surfaces. The metal ring is sufficiently thermally conductive that a radial cross section through the ring at any point along its circumference shows a uniform temperature (i.e. not cooler closer to the surfaces of the ring). In this situation, the steady state temperature at any point in the region enclosed by the ring, and in particular, at the center of the region, is the temperature of the ring itself. That temperature can be deduced from the resistance of the ring, knowing its TCR. 2) A *non-uniform insulated thin chip:* A more interesting situation is that of the above, but with a non-uniform ring whose temperature varies along its circumference, perhaps due to the ring varying in cross-sectional area. In this case, although the temperature will vary spatially within the enclosed region, the steady state temperature at the center of the region is again the average temperature of the ring and that average temperature can be obtained from the resistance of the ring. *3) A non-uniform and uninsulated, thicker chip:* Finally, as an approximation of our experimental system, we consider

the above situation but with incomplete insulation, where the temperature at the center of the enclosed region is still related to the average temperature of the ring, but is offset by heat transfer to and from the enclosed region. This is representative of our microchip design where the enclosed region is in thermal communication with the air and, via conduction through the thickness of the chip, to the remainder of the microchip outside the ring. There may be variations in temperature along the circumference of the heater ring, but as with the examples above, we expect the temperature in the central region to depend largely upon the average ring temperature with correction factors that relate to the lack of insulation in the central region and with a temperature gradient caused by temperature non-uniformities in the ring.

The examples above serve to determine the temperature at the precise center of the enclosed region, i.e. in the limit of an infinitely small volume within a very thin chip. However, for larger volumes (e.g. for dealing with low analyte concentrations) with a thicker (for practical fabrication and handling) microchip system (on the order of mm) and with convection (for cooling and thermal cycling purposes), the temperature distribution becomes a complex function of several variables including geometries, material properties, and the environment surrounding the microchip. Hence, optimization through solving analytical expressions is impractical and thermal non-uniformities could greatly impact the reliability of the analyses. FEM can readily handle the problem in an efficient manner, allowing design variations to be easily made and rapidly studied for trends. Our primary interest is in genetic amplification (via the polymerase chain reaction, PCR) and this requires that we maintain a uniform temperature (within 1°C) in the reaction chamber. The low concentration of DNA in our typical sample requires that we use a moderately large volume chamber, one with a 1-1.5 mm radius. This provides what is largely a worst-case scenario for the application of our method – a smaller volume PCR would better approximate the simplified situations described above and would hence be less susceptible to temperature non-uniformities. The present work demonstrates a method that allows the determination of the temperature in the central region by ascertaining the correction factors described above (and minimizing them) thereby allowing the use of this compact single resistive element temperature control approach for a wide range of designs.

2.2.1 Model used for simulation

FEMLAB 3.1i (COMSOL Inc., Los Angeles, USA) was used to perform FEM to investigate the effects of various microchip and thin film resistive element design parameters on the temperature distributions within the microchip. Two simplified, representative chip models were considered, corresponding to two different microfluidic valving strategies. The two-layer system (Figure 2-1a), based on the work of Pilarski *et al.* [26], consists of a reaction chamber, channels, and loading reservoirs molded into a poly(dimethylsiloxane) (PDMS) layer that is irreversibly bonded onto a glass substrate. Valving is accomplished using micro-robotic arms to press down on the flexible PDMS and pinching channels closed. The three-layer system (Figure 2-1b), based on the work of Grover et al. [27], consists of a PDMS membrane sandwiched between two etched glass plates to form simple, pneumatically-driven valves. Design optimization was completed for both models, but for simplicity, only the results for the two-layer microchip architecture will be discussed as an example here (for this section) to demonstrate the observed trends. Similar trends and results were observed for the three-layer microchips as well.

Since biochemical reactions are typically performed in aqueous environments, for the purpose of simulation, the reaction chamber in the model was treated as being filled with water. For simplicity, channels and loading reservoirs were not included since from prior simulations, we had established that this omission significantly decreased the computation time with no observable compromise on the outcome. A platinum resistive thin film element deposited on the bottom surface of the microchip was considered (Figure 2-1c). Though in practice, a titanium adhesion layer is also deposited, its thickness (~20 nm) is much less than that of the platinum thin film (~200 nm) and the titanium is likely largely oxidized (and nonconductive). Hence, the properties of the platinum dominate and the titanium is therefore not considered in the microchip model. The resistance of the thin film element was chosen to be ~70 Ω (defined by the width, w, of the heater ring), which allows it to heat the reaction chamber to typical temperature ranges for performing biochemical reactions (up to 100°C) with reasonable electrical requirements (under 20 V and 200 mA).

The size of the resistive element (in the order of mm) was chosen to ensure that the resistivity of the element would be uniform: the element sizes were sufficiently large to avoid being prone to errors caused by photolithographic resolution limitations (~1 μm), yet still small enough to avoid significant thickness variations introduced by the platinum deposition process. The thicknesses of deposited platinum thin films could vary (smoothly) by up to ~10% across a standard substrate (~100 mm x 100 mm). We estimated that by keeping the resistive element within a 10 mm x 10 mm area, the thickness variations across the thin films due to deposition would be smaller than ~1%. According to our simulations of the element (at ~125°C), such variations would give rise to less than a 1°C variation in the temperature distribution of the thin film. Resistive element and microchip geometries (dimensions in Figure 2-1c) were simulated to find general trends and to determine a suitable design for optimizing temperature uniformity (discussed below).

2.2.2 Model implementation

FEMLAB 3.1i was used to simulate the heat transfer and temperature distribution within the microchip (more details in Appendix E). The material properties used are listed in Table 2-1. Boundary conditions for all internal interfaces (between the different material elements within the chip itself) were set as continuous temperature (heat transferred by conduction). External boundary conditions were set to emulate the experimental conditions (i.e. the environment/setup in which the microchip is operated) corresponding to a chip held by the edges in a holder at room temperature and insulated below. More specifically, these consisted of thermal insulation on the bottom surface of the microchip, constant ambient temperature (22°C) on the sides of the microchip, and convective and radiative heat flux (heat transfer coefficient = 5.6 W/m²·K for natural convection in air [28] and emissivity = 1) on the top surface of the microchip (these boundary conditions for a 'held chip' are denoted b.c. 1). In certain cases, all external boundary conditions in the model were changed to heat flux to model the microchip suspended in air (these 'suspended chip' boundary conditions are denoted by b.c. 2). This change in boundary conditions was used to investigate the susceptibility of the temperature distribution of the microchip design to changes in its operating environment.

Table 2-1. Material properties used in FEM.
The temperature dependence of these properties was assumed to be negligible

Material	Thermal Conductivity (W/m·K)	Specific Heat Capacity (J/kg·K)	Density (kg/m³)
Borofloat glass [29]	1.11	830	2200
PDMS [30]	0.18	1100	1030
Water [29]	0.58	4187	1000
Platinum [29]	72	133	21500

Since the resistive element is extremely thin compared to the other microchip components, it is very challenging for it to be meshed and solved in 3D due to computational limitations posed by the FEA software and implementation [31]. A standard approach to dealing with this situation is to consider the thickness of the resistive element negligible and model it as a 2D boundary. The assumption made is that the resistive element is sufficiently thin and conductive (thermally as well as electrically) such that no temperature or voltage gradient exists across its thickness. The resistive element generates heat via Joule heating and its resistivity (ρ) depends on its temperature through the following relationship:

$$\rho = \rho_0(1 + \alpha(T - T_0)) \tag{2-1}$$

ρ_0 is the resistivity of the platinum element at the reference temperature T_0, while α is its TCR. It is typical that the resistivity and the TCR of a metal thin film substantially differ from those of its bulk form [32]. Hence, to ensure accuracy of the simulation, these values were experimentally established for annealed (200°C for 2 hours at atmosphere) platinum thin film elements fabricated as test samples (line-shaped elements that have not been optimized for temperature sensing, are fabricated in the same manner). The resistances of these test samples at room temperature were measured and used to determine their average resistivity at room temperature. The platinum thin films were electrically insulated and immersed in a water bath (HAAKE Phoenix II P1 circulator, Thermo Electron Corp., Waltham, MA, USA) to measure their resistances for various temperatures. The TCR was then extracted from the resulting resistance vs. temperature (R vs. T) relationship. Resistive heating is modeled by applying a voltage or current as a boundary condition on the electrode pads of the resistive element.

2.2.3 Model validation

Annealed (200°C for 2 hours) resistive elements were patterned onto microchips with the two-layer architecture (Figure 2-1a). A source measurement unit (Keithley model 236, Cleveland, OH, USA) was then used to apply various currents to these elements (causing resistive heating) and to measure the voltage across them after the steady-state was reached. As a test of the validity of our FE modeling, the resistive
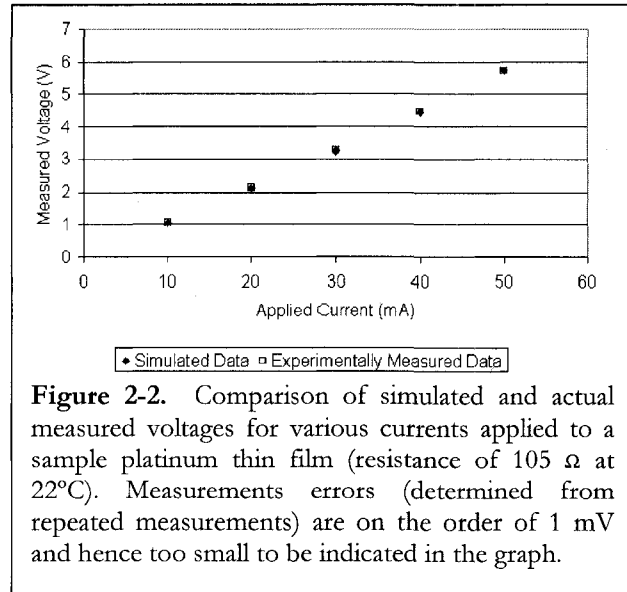
Figure 2-2. Comparison of simulated and actual measured voltages for various currents applied to a sample platinum thin film (resistance of 105 Ω at 22°C). Measurements errors (determined from repeated measurements) are on the order of 1 mV and hence too small to be indicated in the graph.

elements in these experiments were simulated to first predict the temperatures within the chip and then to predict the experimentally measured voltages. Since the microchips were suspended in air when voltages were measured, the b.c. 2 set of external boundary conditions were applied in the simulation. The data obtained from the simulations (Figure 2-2) matched the experimental data well with an average absolute error of 0.016 V (corresponds to ~1°C). This small error is likely accounted for by the fact that the parameters used in the FE model are approximate.

2.2.4 FE results for temperature uniformity within the resistive element

Temperature uniformity on the resistive element is required in order to accurately deduce the temperature of the heater from its resistance. Therefore, we varied design parameters (Figure 2-1c) in our FE model to optimize the temperature uniformity of the resistive element. For comparison purposes, the applied voltages were adjusted such that the temperature of the resistive element was always ~100°C at steady-state for the different design parameters considered. The temperature non-uniformities tended to scale with temperature (i.e. at lower temperatures the variations were proportionally smaller). To

evaluate the temperature distribution along the length of the resistive element, a circular boundary splitting the ring in half was considered in the model. The temperature along the arc-length of this boundary was plotted, effectively yielding the temperature profile along the middle of the ring. Such temperature profiles could be compared after changing the design parameters (Figure 2-3).

Figure 2-3. Optimizing temperature uniformity along the resistive element in a PDMS/glass microchip model with boundary conditions described in section 2.2.2.
(a) Effect of electrode pad connection width, x (R = 2 mm, w = 0.2 mm, r = 1 mm, d = 10 mm, b.c. 1)
(b) Effect of proximity of chip edges, d (R = 2 mm, w = 0.2 mm, x = 0.4 mm, r = 1 mm)

We found that the width of the connections between the heater ring and the electrode pads (the distance marked 'x' in Figure 2-1c) affects the temperature uniformity on the rest of the resistive thin film element since it determines how electric current and heat flow through this area. Figure 2-3a illustrates the temperature profiles for a single-ring resistive thin film as its electrode pad connection width is incrementally widened. If the connections are made narrow (x = 0.2 mm and x = 0.3 mm), the ends of the heater connected to the electrode pads become areas of relatively higher electrical resistance and become hot spots consisting of confined regions of substantially higher temperature (by up to 3°C) than the rest of the heater ring. On the other hand, if the connections are made wide (x = 0.5 mm and x = 0.6 mm), the middle of the heater ring becomes a hot spot instead. In this case, a substantial amount of heat is escaping into the electrode pads, causing the ends of the heater ring to be at a lower temperature relative to the remainder of the resistive element. Between these two cases, an optimum connection width exists (x = 0.4 mm), where the temperature distribution is the most uniform. For example, in Figure 2-3a, the temperature variation along the length

24

of the ring is minimized to within 0.3°C when x = 0.4 mm. We found that given the same microchip architecture, the optimum connection width scaled linearly with the heater ring width (w), which can be adjusted to define the resistance of the resistive element. For the Pt resistive element and glass/PDMS structure considered here, the optimum connection width was found to be approximately twice the heater ring width (i.e. x ≈ 2w).

The geometry of the microchip also has a substantial effect on the temperature distribution in the resistive element. Figure 2-3b reveals that when the edges of the microchip are located close to the resistive element (d = 4 mm), the temperature distribution of the ring is less uniform. More specifically, with the boundary conditions described earlier in section 2.2.2, the relatively cool ambient temperature boundary conditions of the microchip edges caused the sides of the heater ring closest to these edges to be ~1°C-1.5°C lower than the rest of the ring (d = 4 mm, b.c. 1). However, if all the external boundary conditions were changed to convective and radiative heat flux (i.e. the microchip is surrounded by air on all sides), the sides of the heater ring became hotter than the rest of the ring, reversing the temperature distribution (d = 4 mm, b.c. 2). We believe that the microchip material between the resistive element and the microchip edge acts as thermal isolation between the element and the external environment. Therefore, if the microchip edges are located close (e.g. d = 4 mm), to the resistive element, insufficient thermal isolation is provided and the temperature distribution of the element becomes susceptible to the external conditions (e.g. changing between b.c. 1 and b.c. 2). On the other hand, if the edges of the microchip are located far from the heater ring (d = 10 mm), adequate thermal isolation is provided between the resistive element and the external environment, and hence, the temperature distribution in the resistive element is more uniform and does not change when the conditions on the external microchip surfaces are altered between b.c. 1 and b.c. 2 (Figure 2-3b). For the case of d = 10 mm, an increase of 10°C in room temperature causes only a 0.1°C increase in temperature variation along the ring. Although this external room temperaure increase will result in the rise of the overall temperature of the heater, during regular operation with a closed loop feedback controller, this increase in temperature will be compensated. It was found that, for the same microchip architecture, the minimal distance between the resistive element and the microchip edges (d) required to provide adequate thermal isolation scaled

linearly with the radius of the heater ring (R). This minimal distance is approximately five times the heater ring radius (i.e. $d \approx 5R$) for the PDMS/glass structure considered here. If a different microchip architecture (e.g. layer thicknesses) or different materials (thermal conductivities) are employed, the degree of thermal isolation provided would be altered, and simulations would be necessary to establish this minimal spacing (between Pt ring and edge of the chip). Like the microchip edges, other features on the microchip (e.g. valves, pumps, etc.) may also affect the temperature distribution of the resistive element and should hence be adequately spaced from the heater ring as well to ensure temperature uniformity. However, the microchip should not be made any larger than necessary, since a large size will reduce the speed of thermal transients in the system (due to a larger thermal mass) as well as the potential device density, without substantially improving temperature uniformity.

2.2.5 FE results for temperature uniformity within the reaction chamber

Temperature uniformity in the region targeted for thermal regulation (reaction chamber) is typically a requirement in microfluidic chips, particularly when dealing with biochemical reactions. The temperature distribution in the chamber (1 mm radius) was evaluated by plotting the temperature profiles along the radial (along the bottom of the chamber) and vertical (along the center of the chamber) directions of the chamber (Figure 2-4). We found that the temperature distribution within the chamber can be optimized using two key parameters: (a) the height of the chamber, and (b) the size of the heater ring.

Firstly, the temperature profile along the vertical direction of the chamber was dictated primarily by the thermal conductivity of the chamber. The temperature variation along this vertical direction could therefore be significantly reduced only by decreasing the height of the chamber (Figure 2-4a). For the chamber filled with aqueous contents considered here and under b.c. 1, a chamber height smaller than 0.1 mm ensures temperature variations along the vertical direction of the chamber are smaller than 0.5°C. However, decreasing the height of the chamber also increases its surface area to volume ratio, which may present problems with increased sample adsorption [3]. Therefore, to obtain desirable temperature uniformity along the vertical direction of the chamber, additional considerations (e.g. surface coatings)

must be in place to ensure that shortening the height of the chamber, and hence increasing its surface area to volume ratio, will not affect the functionality of the microchip.
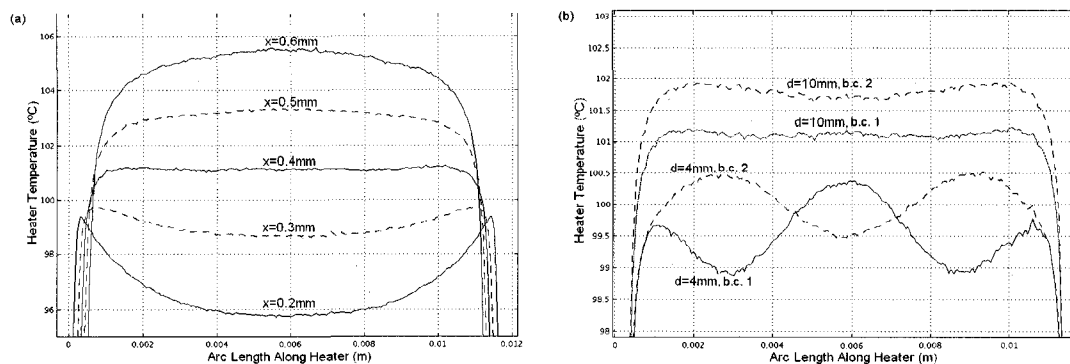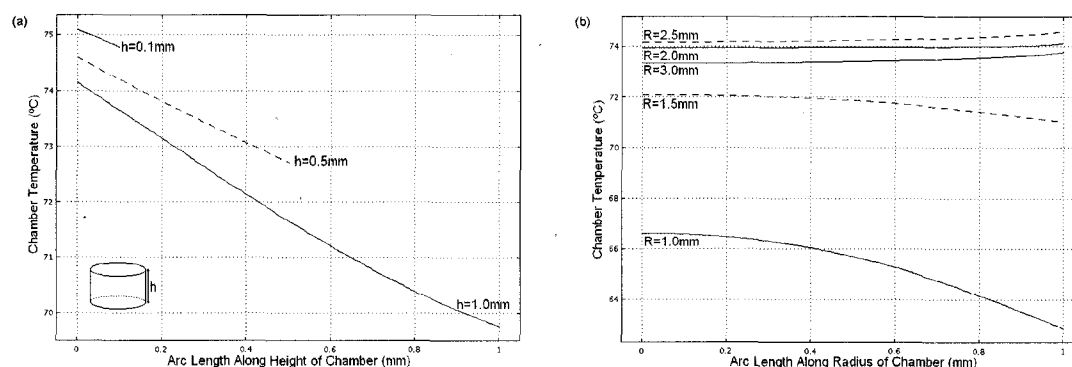

Figure 2-4. Optimizing temperature uniformity in the reaction chamber of a PDMS/glass microchip model with boundary conditions b.c. 1 described in section 2.2.2.

(a) Effect of chamber height (h) on the temperature profile in the vertical direction of the chamber (R = 2 mm, w = 0.2 mm, x = 0.4 mm, r = 1 mm, d = 10 mm)

(b) Effect of heater radius (R) on the temperature profile in the radial direction of the chamber (w = 0.2 mm, x = 0.4 mm, r = h = 1 mm, d = 10 mm)

The temperature profile along the radial direction of the chamber can be controlled by optimizing the radius of the resistive element. Figure 2-4b shows that increasing the radius of the heater ring improves the temperature uniformity in the radial direction of the chamber, bringing it well under 1°C. Placing the heater ring too close to the chamber (R = 1.0 mm and R = 1.5 mm) will cause the high temperature areas in the vicinity of the heater ring to heat the chamber non-uniformly, resulting in large temperature variations (up to 5°C) along the radial direction of the chamber (Figure 2-4b). As the radius of the heater ring is increased, the high temperature areas in the vicinity of the heater ring are moved further away from the chamber, resulting in a local minimum of the temperature distribution in the area inside the heater ring (i.e. the location of the chamber) where the temperature becomes uniform. Once the region of relatively uniform temperature near the local minimum is large enough to encompass the chamber (R = 2.0 mm), further increase in the radius of the heater ring provides no observable improvement in the temperature uniformity of the chamber (Figure 2-4b). It was further observed that, for a constant heater temperature, as the radius of the heater ring is increased, the chamber temperature initially increases since the heater is increasing in size and is thus providing heat to a larger area in the vicinity of the chamber. However, as the radius of the heater ring is increased past a certain point (R = 2.5 mm), the

overall chamber temperature becomes progressively cooler (Figure 2-4b) since the heater ring is moving away from the vicinity of the chamber. Such a trend may be detrimental in platforms limited in power since to obtain the same chamber temperature, a larger resistive element would have to reach a higher temperature than a smaller element. Hence, a large resistive element increases power consumption without providing improvements of temperature uniformity. Furthermore, a larger resistive element would reduce device density. As a result, there is an optimal heater ring radius that maintains temperature uniformity in the reaction chamber while minimizing power consumption. For a given microchip architecture, this optimal heater ring radius (R) scales linearly with the radius of the reaction chamber (r). For the glass/PDMS structure considered here, the optimal heater ring radius is $R \approx 2.5r$. It should be noted that different material thermal conductivities, microchip layer thicknesses, and resitive element positions (relative to microchip layers) will affect the optimal spacing between the heater ring and the reaction chamber. Therefore, although the trend will be similar to as established here, the optimal heater ring radius will vary with different microchip architectures.

2.3 MATERIALS AND METHODS FOR ON-CHIP RT-PCR

2.3.1 Microfluidic chip architecture

We make use of the trends established in section 2.2 (for maintaining temperature uniformity) to design a microchip for performing genetic amplification using the single resistive element approach. Because PDMS is permeable to air, the two-layer microchip architecture (Figure 2-1a) is susceptible to vapor loss. Hence, the three-layer glass/PDMS/glass microchip architecture (Figure 2-1b) was employed instead. The reaction chamber and fluidic channels are 90 μm deep to ensure that temperature variations along the height of the chamber were negligible. The volume of the PCR chamber (1.5 mm radius) was chosen to accommodate ~600 nL. We can readily shrink the volume further if necessary, but the current volume is dictated by our biological applications (e.g. the clinically significant levels of DNA-virus in samples of bodily fluid are low enough that we require such volumes to ensure that the sample volume contains a DNA template) [24, 33]. The

platinum resistive element is physically located on the top surface of the lower glass substrate (control layer), directly under the PDMS membrane (Figure 2-1b). In this position, the resistive element is close to the reaction chamber, but does not come into direct physical contact with the biological sample, preventing the platinum from potentially inhibiting the PCR [3]. Using similar simulations to those presented in section 2.2 for the two-layer architecture, the microchip and resistive element geometries were optimized for temperature uniformity (within 1°C) in the three-layer architecture. The final optimized dimensions were (as defined in Figure 2-1c): x = 0.4 mm (for w = 0.2 mm), R = 2.5 mm, and d = 5 mm.

2.3.2 Microfluidic chip fabrication

The PCR microchip consists of a pre-cast polydimethylsiloxane (PDMS) membrane (254 μm) (HT-6135, Bisco Silicones, Elk Grove, IL, USA) placed between two patterned glass plates. The top glass plate is termed the fluidic layer, while the bottom layer is termed the control layer. Both the glass plates were etched using standard wet etching processes. The platinum resistive thin-film elements (200 nm) are sputtered on top of the control layer along with a thin titanium adhesion layer (20 nm). A lift-off technique was used to pattern the platinum/titanium thin films. Holes in the fluidic layer were formed using water-jet drilling (Bengal, Flow International Corporation, Kent, Washington, USA). Irreversible bonding between the PDMS membrane and the glass substrates is achieved by UV/ozone activation of the PDMS surface. Further details can be found in [34].

2.3.3 Resistive element preparation and calibration

Following sputter deposition, the Pt films are annealed to ensure subsequent stable operation. Annealing is performed by passing a current of ~120 mA through the resistive element to hold it for ~2 hours at temperatures of ~200°C (at atmospheric pressure), allowing its resistivity to become constant with time. Typically, this annealing step results in a ~3-5 Ω drop in the total resistance of the resistive elements used in this study (typically ~70 Ω at room temperature to allow operation requiring less than 20 V and 200 mA). Once annealed, the resistive element is calibrated to establish the relationship between its

resistance and temperature. The resistive element is immersed in a water bath (HAAKE Phoenix II P1 circulator, Thermo Electron Corp., Waltham, MA, USA) and its resistances at various temperatures are measured and plotted (R vs. T). The water bath is accurate to 0.1°C, and for each temperature data point, fifteen minutes are allowed for steady-state to be reached. The least squares method is then performed to obtain the best-fit line for the R vs. T relationship. We have further established that this R vs. T relationship does not undergo any observable changes with usage, and hence only needs to be characterized once. The resistivity of the film is ~172 Ω·nm, differing as expected from the bulk value of 106 Ω·nm. The temperature coefficient of resistivity (TCR) is ~0.0022°C^{-1}, comparable to other reported values of 0.00248°C^{-1} [21] and 0.00235°C^{-1} [35].

2.3.4 Operation of the PCR microchip

To operate the microchip, a custom-built stage was used to couple pressure/vacuum lines and electrode pins to the microchip. Microcontroller-based custom-built electronics were used to operate the resistive element as well as the valving and pumping. The microcontroller applies a current to the resistive element and measures its resistance using a Wheatstone bridge configuration to ensure high precision by improving signal resolution. The sensitivity of the output signal is ~3 mV/°C, and hence, by measuring it with 16-bit accuracy, changes in temperature smaller than 1°C could be measured, which is sufficient for our application. Increasing the resistance of the resistive element would increase its sensitivity to temperature, but would require a higher voltage supply for operation. A resistance of ~70 Ω was therefore chosen here since one of the goals is to ensure the resistive element is suitable for portable and inexpensive diagnostic platforms by remaining within reasonable power limits (under 20 V and 200 mA). The temperature of the resistive element is calculated from its resistance using its pre-determined R vs. T calibration (pre-stored in the microcontroller or entered by the user). This temperature is used to deduce the temperature in the reaction chamber using a relationship determined using the method described later in section 2.4.1. Hence, with the temperature at the resistive element as feedback, the applied current is controlled to result in the desired temperature for PCR in the reaction chamber.

2.3.5 RT-PCR mixture

The RT-PCR reaction mix and thermal cycling program employed (for amplifying the β2 microglobulin gene) had been optimized for use on a conventional thermal cycler. The RT-PCR reaction mix consisted of the following in 25 µL: 5 µL H_2O, 12.5 µL 2X reaction mix (Invitrogen, Carlsbad, CA, USA), 5 µL 5 mM $MgSO_4$, 0.5 µL 10 µM forward primer (CCA GCA GAG AAT GGA AAG TC), 0.5 µL 10 µM fluorescently VIC-labelled reverse primer (ACT TAA CTA TCT TGG GCT GTG AC), 0.6 µL 10 mg/mL bovine serum albumin (BSA, Sigma-Aldrich, St. Louis, MO, USA), 0.5 µL enzyme mix, and 0.4 µL 1 µg/mL template RNA (purified clinical sample). The BSA was included to help counter surface adsorption effects (binds more preferentially to channel walls than the PCR components). The thermal cycling program consisted of: a reverse transcription stage of 45°C for 30 min., a pre-denaturation stage of 94°C for 2 min., 35 cycles of 94°C for 15 s, 60°C for 30 s, and 68°C for 30 s, and a post-extension stage of 68°C for 8 min. These dwell times may be shortened further to accomplish a more rapid RT-PCR, but since temperature accuracy and uniformity was the primary focus of this study rather than operation speed, the original conventional thermal cycler dwell times were retained.

2.3.6 Detection of the PCR product using microchip capillary electrophoresis

After the genetic amplification is completed, detection and analysis was performed by capillary electrophoresis (CE) using a commercial Microfluidic Tool Kit (µTK, Micralyne, Edmonton, AB, Canada). The thermally cycled mix from the PCR chamber is loaded onto a glass CE microchip (Micralyne, Edmonton, AB, Canada) and separation of the DNA was achieved using an injection voltage of 0.4 kV and a separation voltage of 6 kV. The polymer used within the CE microchip is 5% Genescan polymer (Applied Biosystems, Foster City, CA, USA) with 10% glycerol in water. Product sizing was done by including GS500 size standard (Applied Biosystems). Further details can be found in [36].

2.4 CHAMBER TEMPERATURE CHARACTERIZATION AND CONTROL

As discussed earlier, and as in similar implementations by others, due to the low thermal conductivity of the materials used in the microchips, a substantial offset exists between the temperature at the reaction chamber (T_c) and the temperature at the resistive element (T_h). In order to use the resistive element as a sensor for feedback to control the temperature within the reaction chamber, the relationship between T_c and T_h must be established. To determine this relationship, the thermal system of the microchip can be likened to an electrically equivalent network (the governing equations have similar forms), where temperatures are analogous to voltages, heat flux is analogous to electrical current, thermal conductance/resistance are analogous to electrical conductance/resistance, and heat capacity is analogous to electrical capacitance (further details in Appendix A). This is a common analogy for thermal systems [37, 38], where thermal conduction is modeled as a network of parallel RC circuits, while convection is modeled as a resistance, with the temperatures at the locations of interest acting like voltage nodes. For the microchip considered here, heat generated by the resistive element travels via thermal conduction to the chamber and to the surface of the microchip. It then dissipates into the ambient environment via natural convection. Considering this generalized heat flow path, we obtain the simplified equivalent electrical model depicted in Figure 2-5a. The layers of the chip provide relatively low thermal resistances (conduction over relatively short distances) whereas the transfer of heat from the chip surface (via convection to the room air) acts as a relatively high thermal resistance (see Appendix A). In the steady-state case, the time-dependent capacitive effects are eliminated, and hence, the thermal problem can be treated as an electrical resistive divider network. The temperature at the reaction chamber should therefore depend linearly on the temperature at the resistive element in the steady-state.

Though T_c is difficult to measure without perturbing the thermal conditions, the temperature at the top surface of the microchip above the chamber (T_s) is readily measured using either a patterned Pt film that is operated as a temperature sensor or a thin wire (40 gauge) thermocouple (5TC-TT-K-40-36, Omega Engineering, Laval, Quebec, Canada). With the resistive divider model, both T_c and T_s are expected to vary linearly with T_h. However, T_s is

32

much closer to T_c than T_h, due in part to the fact that the thermal conductivity of the PDMS separating T_c and T_h is much lower than that of the glass separating T_c and T_s (Table 2-1). Geometry also plays a role. Simulations have shown that the steady-state temperature difference between T_c and T_s is roughly a third of the difference between T_c and T_h (T_s is no further than ~10°C away from T_c for the operating temperatures considered), and that the dynamic behaviour of T_s closely resembles that of T_c. Therefore, to calibrate the microchip, we set T_h, measure T_s and use a 'short-range' extrapolation from T_s to estimate T_c (using FEM). We then have a relationship between T_s, T_c and T_h (Figure 2-5b) and can subsequently use T_h to predict T_c through a 'long-range' extrapolation. This is very much the situation with many thermal-sensing applications where the true temperature must be extrapolated from the measured value. As discussed by Noh et al. [17], this is particularly an issue with glass-based devices where temperature differences of tens of degrees must be dealt with. These measurements also served to corroborate the simulation results, with agreement to within 1°C. After these measurements of T_s have been made once, subsequent use of the chip relies only upon measurements of T_h. The accuracy of the simulations suggests that the T_s measurements were not needed – although useful as a confirmation.

2.4.1 Static condition

To establish the required relationship between T_c and T_h, we sometimes used a separate calibration microchip having the same architecture as in Figure 2-1, but with an additional platinum resistive element deposited on the top surface of the upper glass plate (fluidic layer) to function as a temperature sensor that measures T_s (Figure 2-5a). We also used a thin wire thermocouple attached to the top of the microchip (measurements using both methods agreed to within 1°C). The resulting T_s was then measured for various T_h (done at a room temperature of 22°C and with temperatures held for 5 minutes to ensure steady-state is reached). These experimentally determined temperatures were subsequently employed as boundary conditions in a FEM of the microchip (set up with the same material properties and external boundary conditions as described in section 2.2.2), which was then solved to estimate T_c after steady-state was reached ('short range' extrapolation). Using this combination of experimental measurement (T_h and T_s) and simulation (prediction of T_c from

T_h and T_s), we verified that T_c (as well as T_s) varied linearly with T_h in the steady-state case (Figure 2-5b). This linear mapping function between T_c and T_h can be used to control T_c on the basis of measuring T_h ('long range' extrapolation). For each PCR temperature stage, the temperature controller uses the established T_c vs. T_h mapping function to determine the T_h required to obtain the desired T_c and maintains the resistive element at this T_h. Because the reaction chamber is sufficiently thermally isolated from room temperature (low thermal conductivity of glass and only natural convection at work), we have observed (both experimentally and analytically) that this mapping function allows T_c to be predicted to within 1°C if room temperature (T_{ext}) does not change by more than 3.5°C (see Appendix B).
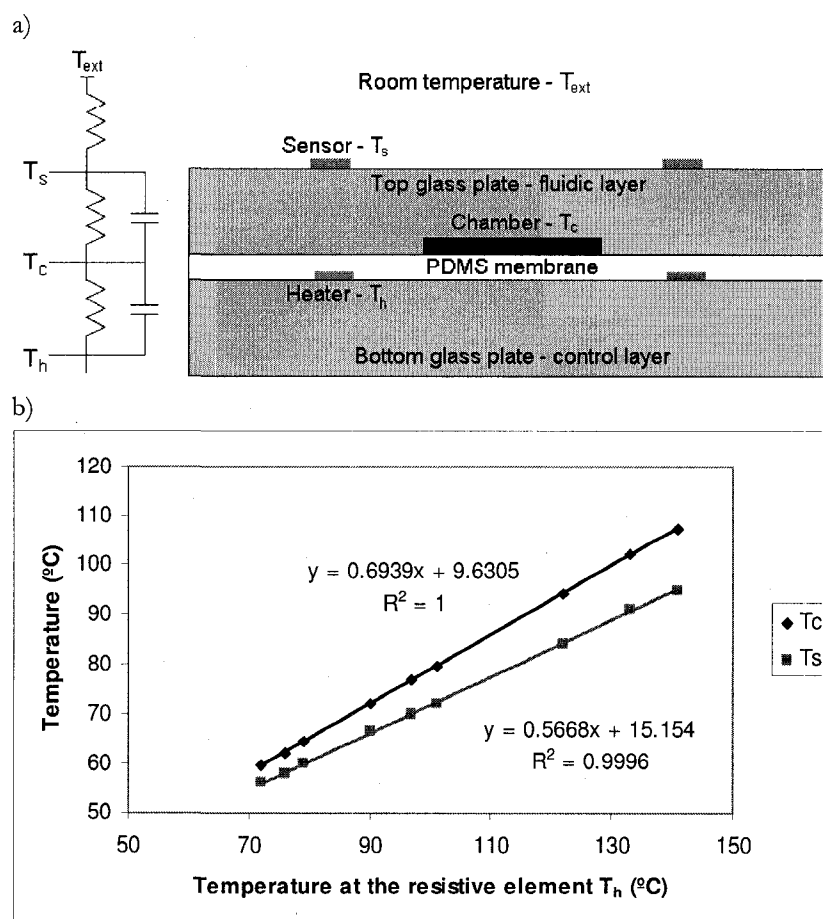
Figure 2-5.
    a) Cross-sectional view of the microchip depicting the temperatures of interest and its simplified analogous electrical model (with temperature nodes at the locations of interest).
    b) The linear dependence of the calculated T_c and the experimentally measured T_s on the measured T_h at steady-state.

With the methods presented here, we can obtain the relationship between T_c and T_s only through simulation (i.e. we cannot measure T_c directly). This is a 'short-range' extrapolation and hence not likely to contribute a large error, but nonetheless depends on the accuracy of the FE model. On the other hand, we can obtain the relationship between T_h and T_s either through simulation or through experiment, and can hence compare the two to verify the accuracy of the FE model. As a 'long-range' extrapolation, it is more prone to error, but we found that experiment and simulation agreed to within 1°C in the following method. The FE model of the calibration microchip was used to predict the expected T_s values when the desired T_c values for PCR are obtained (in the steady-state case). Actual calibration microchips were then operated (using the determined T_c vs. T_h mapping function) and the actual T_s was measured at each PCR stage. The experimental and predicted values matched to within 1°C. Hence, the FE model is accurate and the function of T_c vs. T_h holds true under static offset conditions. However, since the linear relationship is valid only in the steady-state case, it cannot be applied accurately in the dynamic case where capacitive effects are present (e.g. T_h heats at a much faster rate than T_c because the heat capacity of the resistive element is much smaller than that of the reaction chamber).

2.4.2 Dynamic condition

The temperature of the chamber is regulated by using a custom-built software controller that controls the temperature of the resistive element. The controller design satisfies two conditions: one is the rapid temperature transition between set-points, and the second is the regulation around set-point temperatures with minimum errors (static state). Proportional-derivative (PD) control is used to obtain rapid transients between the different temperature stages while proportional-integrative (PI) control is used to maintain a constant temperature during the stages themselves [39]. The dynamic temperature within the chamber during set-point transitions is regulated using a bumpless transfer strategy for switching from the PD controller to the PI controller. This results in rapid set-point transitions, while minimizing overshoots and undershoots. Further details on the control strategy will be reported on elsewhere [40].

For PCR, rapid thermal transitions between the different stages helps in shortening the duration of the process (faster tests) and in improving the yield. However, temperature overshoots can reduce the activity of the replication enzyme or even boil the reaction mix, while undershoots can compromise the specificity of the amplification process. In the PCR microchip considered here, it was found that due to the low thermal inertia of the resistive element, T_h can change rapidly and reach its set-point within 1 s of heating. However, on account of the low thermal conductivity of the glass and the PDMS separating the resistive element and the reaction chamber, as well as their much greater thermal inertia, T_c changes at a much slower rate than T_h and can take ~3 minutes to reach within 0.5°C of its final steady-state temperature with a fixed T_h. Therefore, to improve heating rates within the chamber, short heating stages were introduced where T_h is raised to higher temperatures than required (8-50°C higher) for a few seconds (3-8 s). FEM simulations provided us with an appropriate temperature and duration for these heating stages to maximize heating rates in the chamber while still avoiding undesirable overshoots or undershoots (Figure 2-6). Our temperature controller ensures temperature ramping rates are relatively slow when approaching a set-point (3°C before the set-point is reached, a bumpless handover from the PD to the PI controller is programmed and the PI controller parameters are pre-set to realize a ~1°C/s temperature variation up until the set-point is reached). Under these conditions, we have determined by simulation that overshoots or undershoots in T_c are at most ~1°C larger than those measured in T_s. Using this guideline, the heating stage parameters were fine-tuned experimentally to ensure minimal (<1°C) overshoots or undershoots in T_s.

Cooling of the reaction chamber relies on passive natural convection to the surrounding environment and on thermal conduction to cooler regions of the microchip (and the stage). To minimize the resistive heating effects during the cooling state, the current applied to the resistive element is significantly lowered. Only a small current (~15 mA) is applied for temperature monitoring purposes (does not cause significant resistive heating). Simulations have shown that as the microchip cools, the localized high temperature region around the heater dissipates its excess heat more rapidly than does the larger, more uniform temperature region associated with T_c. This occurs because natural convection is associated with a

36

substantially larger thermal resistance than conduction in the microchip (as determined in Appendix A). As a result, temperatures within the microchip equilibrate with each other before subsequently cooling together via natural convection. Figure 2-6 shows that upon cooling, T_h decreases rapidly and soon matches up with T_c. After 10 s of passive cooling, T_h is within 2°C of T_c, and after 15 s, it is within 1°C of T_c. Hence, near the end of the cooling stage (30-40 s long), T_h can accurately represent T_c directly with no offset. Therefore, T_h is monitored during the cooling stage, and when it reaches the desired T_c for the next temperature stage, the cooling stage is ended and the controller resumes applying current to heat the resistive element.
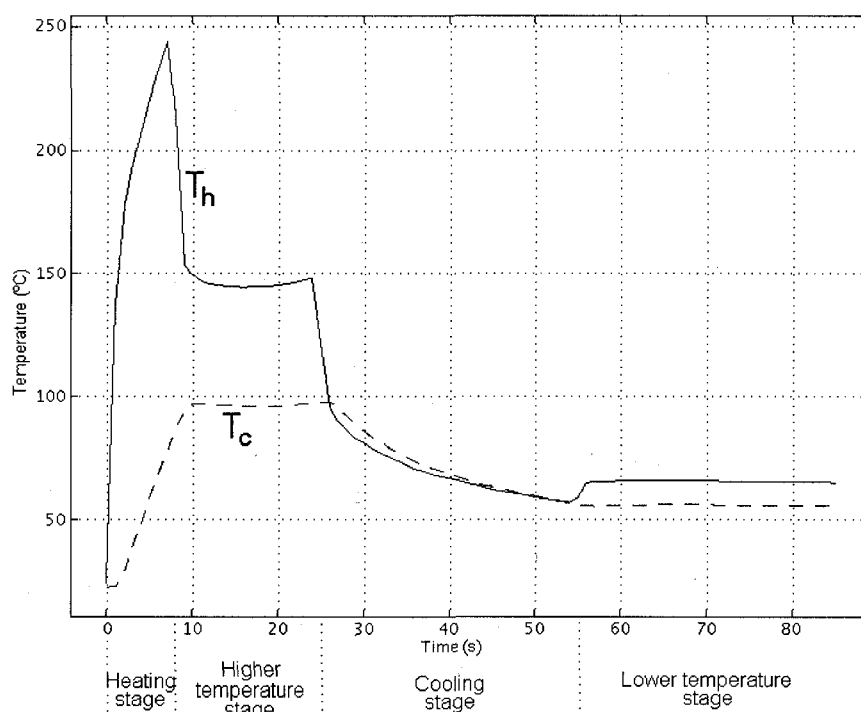
Figure 2-6. FE simulation of the temperatures at the resistive element (T_h) and at the reaction chamber (T_c) for the considered PCR microchip as it undergoes two temperature stages (~94°C and ~60°C).

Currently, we are employing heating rates of up to ~10°C/s and cooling rates of up to ~2°C/s in the reaction chamber. The heating rate is limited by the fact that the resistive element cannot be heated to temperatures higher than ~200°C to avoid exceeding the operating temperature range of the PDMS membrane. The cooling rate is limited by the rate at which heat can be passively removed.

2.5 DEMONSTRATION OF MICROCHIP-BASED GENETIC AMPLIFICATION

Validation of the FEM results for the design optimization, the temperature control approach, and the operation of the developed PCR microchip was provided by the successful demonstration of RT-PCR. The template chosen was $\beta 2$ microglobulin ($\beta 2M$), a gene present in most human cells and thus often used as an experimental positive control. The reaction mixture and temperature control program used on the chip (section 2.3.5) had been adjusted for optimal performance. The RT-PCR products were analyzed by CE as described in section 2.3.6. On-chip RT-PCR runs were reliably successful, yielding product peaks that match with the controls performed on a conventional thermal cycler (Figure 2-7). Given the sensitivity of PCR to small changes in temperature, the presence of the correct product peak and the absence of non-specific peaks provides further indication that the temperature control scheme used is accurate and avoids substantial temperature overshoots or undershoots. The developed microchip has also routinely amplified cancer biomarkers and viral genetic material with similar performance (results in Chapter 5, section 5.5.1).
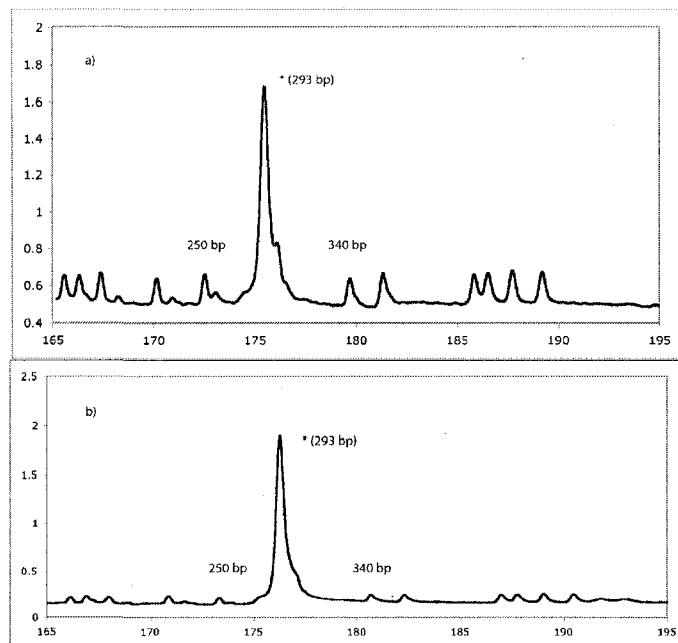
Figure 2-7. Electropherograms of fluorescence (arbitrary units; y-axis) versus time (seconds; x-axis) for successful $\beta 2M$ on-chip RT-PCR. The product (size: 293 bp) is marked by *. Both electropherograms show peaks from a DNA size standard that contributes a number of low-level reference peaks (e.g. 250 and 340 bp). (a) On-chip (b) Conventional thermal cycler control.

2.6 CONCLUDING REMARKS

In this work, FEM was used to design a microchip for performing genetic amplification (RT-PCR) that utilizes a single resistive element as both a heater and a temperature sensor. To our knowledge, this is the first demonstration of a microfluidic lab-on-a-chip device using a single resistive element approach to thermal management. Temperatures in the microchip were characterized and used in conjunction with FEM approaches to determine a mapping function between the temperature of the resistive element and the temperature of the reaction chamber. Though the mapping function is specific to the microchip architecture and environment for which it is characterized, it can be recomputed if necessary using the same method described here. This relationship was used to control the chamber temperature using the temperature measured by the resistive element as feedback. The developed microchips were capable of performing RT-PCR. Temperatures in the steady-state were accurate to ~1°C, but as with any such application, the exact magnitude of any overshoots or undershoots could not be determined (T_c vs. T_h relationship holds only at steady-state). Nonetheless, they were small enough to not affect the amplification of the templates tested here (<2-3°C). Work is being done to further characterize the dynamic temperature behaviour as well as to integrate the developed resistive heating element with other functionalities for sample preparation, detection, and analysis (CE), moving towards a practical disease diagnostic and monitoring tool for the clinical setting.

2.7 REFERENCES

[1] Backhouse, C.J., T. Footz, S. Adamia , and L.M. Pilarski. "Microfluidic chips for molecular analysis of human cancer", in *International Conference on MEMS, Nano and Smart Systems (ICMENS),*. 2003.

[2] Lagally, E.T. and R.A. Mathies, "Integrated genetic analysis microsystems", *Journal of Applied Physics D: Applied Physics*, 2004. **37**: p. R245-R261.

[3] Kricka, L.J. and P. Wilding, "Microchip PCR", *Analytical and Bioanalytical Chemistry*, 2003. **377**: p. 820-825.

[4] Saiki, R.K., D.H. Gelfand, S. Stoffel, S.J. Scharf, R. Higuchi, G.T. Horn, K.B. Mullis, and H.A. Erlich, "Primer-directed enzymatic amplification of DNA with a thermostable DNA-polymerase", *Science*, 1988. **239**(4839): p. 487-491.

[5] DeVoe, D.L., "Thermal Issues in MEMS and Microscale Systems", *IEEE Transactions on Components and Packaging Technology*, 2003. **25**(4): p. 576-583.

[6] Erill, I., S. Campoy, J. Rus, L. Fonseca, A. Ivorra, Z. Navarro, J. Plaza, J. Aguilo, and J. Barbe, "Development of a CMOS-compatible PCR chip: comparison of design and system strategies", *Journal of Micromechanics and Microengineering*, 2004. **14**: p. 1558-1568.

[7] Ferrance, J.P., Q. Wu, B. Giordano, C. Hernandez, Y. Kwok, K. Snow, S. Thibodeau, and J.P. Landers, "Developments towards a complete micro-total analysis system for Duchenne muscular dystrophy diagnosis", *Analytica Chimica Acta*, 2003. **500**: p. 223-236.

[8] Easley, C.J., J.M. Karlinsey, and Landers J. P., "On-chip pressure injection for integration of infrared-mediated DNA amplification with electrophoretic separation", *Lab on a Chip*, 2006. **6**(5): p. 601-610.

[9] Easley, C.J., J.M. Karlinsey, J.M. Bienvenue, L.A. Legendre, M.G. Roper, S.H. Feldman, M.A. Hughes, E.L. Hewlett, T.J. Merkel, J.P. Ferrance, and J.P. Landers, "A fully integrated microfluidic genetic analysis system with sample-in-answer-out capability", *Proceedings of the National Academy of Sciences*, 2006. **103**(51): p. 19272-19277.

[10] Fermer, C., P. Nilsson, and M. Larhed, "Microwave-assisted high-speed PCR", *European Journal of Pharmaceutical Sciences*, 2003. **18**(2): p. 129-132.

[11] Pal, D. and V. Venkataraman, "A portable battery-operated chip thermocycler based on induction heating", *Sensors and Actuators A*, 2002. **102**: p. 151-156.

[12] Firebaugh, S.L., K.F. Jensen, and M.A. Schmidt, "Investigation of high-temperature degradation of platinum thin films with an in situ resistance measurement apparatus", *Journal of Microelectromechanical Systems*, 1998. **7**(1): p. 128-135.

[13] Toriello, N.M., C.N. Liu, and R.A. Mathies, "Multichannel reverse transcription-polymerase chain reaction microdevice for rapid gene expression and biomarker analysis", *Analytical Chemistry*, 2006. **78**: p. 7997-8003.

[14] Yang, M., P. R., and M.A. Burns, "Cost-effective thermal isolation techniques for use on microfabricated DNA amplification and analysis devices", *Journal of Micromechanics and Microengineering*, 2005. **15**: p. 221-230.

[15] Pal, R., M. Yang, R. Lin, B.N. Johnson, N. Srivastava, S.Z. Razzacki, K.J. Chomistek, D.C. Heldsinger, R.M. Haque, V.M. Ugaz, P.K. Thwar, Z. Chen, K. Alfrano, M.B. Yim, M. Krishnana, A.O. Fuller, R.G. Larson, D.T. Burke, and M.A. Burns, "An integrated microfluidic device for influenza and other genetic analyses", *Lab on a Chip*, 2005. **5**: p. 1024-1032.

[16] Oh, K.W., C. Park, K. Namkoong, J. Kim, K.-S. Ock, S. Kim, Y.-A. Kim, Y.-K. Cho, and C. Ko, "World-to-chip microfluidic interface with built-in valves for multichamber PCR assays", *Lab on a Chip*, 2005. **5**: p. 845-850.

[17] Noh, J., S.W. Sung, M.K. Jeon, S.H. Kim, L.P. Lee, and S.I. Woo, "In situ thermal diagnostics of the micro-PCR system using liquid crystals", *Sensors and Actuators A*, 2005. **122**: p. 196-202.

[18] Liao, C., G. Lee, H. Liu, T. Hsieh, and C. Luo, "Miniature RT–PCR system for diagnosis of RNA-based viruses", *Nucleic Acids Research*, 2005. **33**(18): p. e156:3-7.

[19] Lagally, E.T., J.R. Scherer, R.G. Blazej, N.M. Toriello, B.A. Diep, M. Ramchandani, G.F. Sensabaugh, L.W. Riley, and R.A. Mathies, "Integrated portable genetic analysis microsystem for pathogen/infectious disease detection", *Analytical Chemistry*, 2004. **76**(11): p. 3162-3170.

[20] El-Ali, J., I.R. Perch-Nielsen, C.R. Poulsen, D.D. Bang, P. Telleman, and A. Wolff, "Simulation and experimental validation of a SU-8 based PCR thermocycler chip with integrated heaters and temperature sensors", *Sensors and Actuators A*, 2004. **110**: p. 3-10.

[21] Yoon, D.S., Y.-S. Lee, Y. Lee, H.J. Cho, S.W. Sung, W. Oh, J. Cha, and G. Lim, "Precise temperature control and rapid thermal cycling in a micromachined DNA polymerase chain reaction chip", *Journal of Micromechanics and Microengineering*, 2002. **12**: p. 813-823.

[22] Lee, C.-Y., G.-B. Lee, H.-H. Liu, and F.-C. Huang, "MEMS-based temperature control systems for DNA amplification", *International Journal of Nonlinear Sciences and Numerical Simulation*, 2002. **3**: p. 215-218.

[23]   Liu, J., M. Enzelberger, and S. Quake, "A nanoliter rotary device for polymerase chain reaction", *Electrophoresis*, 2002. **23**(10): p. 1531-1536.

[24]   Kaigala, G.V., R.J. Huskins, J. Preiksaitis, X.L. Pang, L.M. Pilarski, and C.J. Backhouse, "Automated screening using microfluidic chip-based PCR and product detection to assess risk of BK virus-associated nephropathy in renal transplant recipients", *Electrophoresis*, 2006. **27**(19): p. 3753-3763.

[25]   Iles, A., R. Fortt, and A.J. de Mello, "Thermal optimisation of the Reimer-Tiemann reaction using thermochromic liquid crystals on a microfluidic reactor", *Lab on a Chip*, 2005. **5**: p. 540-544.

[26]   Pilarski, P.M., S. Adamia, and C.J. Backhouse, "An adaptable microvalving system for on-chip polymerase chain reactions", *Journal of Immunological Methods*, 2005. **305**: p. 48-58.

[27]   Grover, W.H., A.M. Skelley, C.N. Liu, E.T. Lagally, and R.A. Mathies, "Monolithic membrane valves and diaphragm pumps for practical large-scale integration into glass microfluidic devices", *Sensors and Actuators B-Chemical*, 2003. **89**(3): p. 315-323.

[28]   Fontes, J., "Temperature Sensors", in *Sensor Technology Handbook*, J.S. Wilson, Editor. 2005, Elsevier Inc.: Oxford. p. 531-562.

[29]   Lide, D.R., ed. *CRC Handbook of Chemistry and Physics 86th Edition*. 2005, CRC Press: Boca Raton.

[30]   Erickson, D., D. Sinton, and D. Li, "Joule heating and heat transfer in polydimethylsiloxane microfluidic systems", *Lab on a Chip*, 2003. **3**(3): p. 141-149.

[31]   "Generating Meshes", in *COMSOL Multiphysics User's Guide*. 2005, COMSOL AB: Stockholm. p. 262-297.

[32]   Aviles, F., O. Ceh, and A.I. Oliva, "Physical properties of Au and Al thin films measured by resistive heating", *Surface Review and Letters*, 2005. **12**(1): p. 101-106.

[33]   Van Dijken, J., G. Kaigala, J. Lauzon, A. Atrazhev, B.J. Taylor, T. Reiman, A.R. Belch, C.J. Backhouse, and L.M. Pilarski, "Microfluidic chips for detecting the t(4;14) translocation and monitoring disease during treatment using RT-PCR analysis of IgH-MMSET hybrid transcripts", *Journal of Molecular Diagnostics*, 2007. **9**(3): p. 358-367.

[34]   Kaigala, G., S. Ho, R. Penterman, and C.J. Backhouse, "Rapid prototyping of microfluidic devices with a wax printer", *Lab on a Chip, DOI: 10.1039/b617764f*, 2007.

[35] Lee, D.-S., S.H. Park, H. Yang, K.-H. Chung, T.H. Yoon, S.-J. Kim, K. Kim, and Y.T. Kim, "Bulk-micromachined submicroliter-volume PCR chip with very rapid thermal response and low power consumption", *Lab on a Chip*, 2004. **4**: p. 401-407.

[36] Vahedi, G., C. Kaler, and C.J. Backhouse, "An integrated method for mutation detection using on-chip sample preparation, single-stranded conformation polymorphism, and heteroduplex analysis", *Electrophoresis*, 2004. **25**(14): p. 2346-2356.

[37] Lienhard IV, J.H. and J.H. Lienhard V, *A Heat Transfer Textbook*. 3rd ed. Cambridge: Phlogiston Press, 2005.

[38] Senturia, S.D., *Microsystem Design*. New York: Springer Science+Business Media, Inc., 2001.

[39] Ogata, K., *Modern control engineering*. 3rd ed. New Delhi: Prentice Hall of India Private Limited, 1998.

[40] Kaigala, G.V., J. Jiang, C.J. Backhouse, and H. Marquez, "System design and modeling of a time-varying, nonlinear temperature controller for microfluidics", *IEEE Transactions on control system technology*, Submitted Jan 2006.

Chapter 3

Dynamic temperature measurement in microfluidic devices using thermochromic liquid crystals

3.1 INTRODUCTION

Microfluidic lab-on-a-chip (LOC) devices hold tremendous potential in overcoming the barriers currently limiting their use to the laboratory setting. Precise and localized temperature control in miniaturized systems are important for adapting many molecular biology techniques into such devices. A common example is the polymerase chain reaction (PCR), a technique that employs thermal cycling to amplify genetic material. Temperature overshoots or undershoots (even short duration) are known to have detrimental effects such as reducing the activity level of the replicating enzyme (Taq) or causing errors to be made in the copying process [1, 2]. These effects can lead to false positives or false negatives in medical diagnostics.

As described by Iles *et al.* [3], the temperature characterization of microfluidic devices is challenging since it is difficult to measure their temperature without significant perturbations. Nevertheless, it has been found that thermochromic liquid crystals (TLCs) provide a compact and effective method for measuring temperature at the microscale [3-6]. TLCs react to changes in temperature by changing colour. We make use of cholesteric TLCs, microencapsulated slurries of optically active mixtures of organic chemicals with

44

chiral molecular structures. The colour change effects are caused by the interference and diffraction of reflected and scattered light and are most easily observed in a thin-film state. In bulk, the materials also reflect light, but the predominant observed effect is one of iridescence (hue depends on viewing angle) [7].

Past use of TLCs has measured the temperature either by mapping the hue/colour (e.g. as measured by RGB signal values) to temperature or by mapping the wavelength of the peak of the reflected light to temperature. However, that has not been without challenges. Chaudhari *et al.* [4] went so far as to say that automated image analysis was impractical due to weak signals. They found that attempts to increase the concentration of the TLCs (in order to obtain a stronger signal) failed because it led to the white colour dominating the other colours. Although Noh *et al.* [5] were successful in mapping colour to temperature for steady state temperatures in a microchip PCR application, this success was limited, in part, by problems due to bubble formation at the higher temperature range (i.e. above 90°C). They suggested that these problems might be controlled through the use of integrated valves. Liu *et al.* [6] also used a hue-based method for measurement of the steady-state temperature of a 12 nL reaction PCR volume. Iles *et al.* [3] used the TLC method to measure the steady-state temperature of an organic synthesis reaction within a microfluidic reactor, and suggested the use of TLCs for dynamic applications also. Though much has been done with TLCs, particularly to verify PCR chamber temperatures in the steady-state [4-6], some barriers hinder their use in a dynamic mode. In the present work, we demonstrate a novel TLC-based method that overcomes these barriers and we apply it to tracking temperature transients during PCR.

There is an emphasis in the LOC community towards developing rapid diagnostics. In this context, realizing rapid PCRs within microfluidic devices while still avoiding temperature overshoots and undershoots during transitions is increasingly important. The TLC colour change bandwidth can be customized, but there exists a trade-off between resolution (sensitivity) in measuring temperature and the range of temperatures that can be measured [5]. Since temperature fluctuations as small as 1-2°C are enough to affect PCR, we choose to employ TLCs that change colour over a tight ~3°C range to

45

ensure sufficient resolution in measuring temperature. By analyzing the reflected spectra over time of TLCs placed inside the reaction chamber of the microchip as they undergo thermal cycling, the temperature vs. time trajectory is computed. This is, to our knowledge, the first time that TLCs have been used dynamically within microfluidic devices. This chapter is based on a technical note recently accepted in *Lab on a Chip*.

3.2 MATERIALS AND METHODS

The tri-layered glass/PDMS/glass PCR microchips (Figure 3-1) used here were based on patterned metal films for heating and temperature sensing. These are well-characterized and have been demonstrated to perform PCR reliably (Chapter 2). Integrated microvalves are included for confining the contents of the reaction chamber, eliminating the bubble formation problems observed by Noh *et al.* [5].
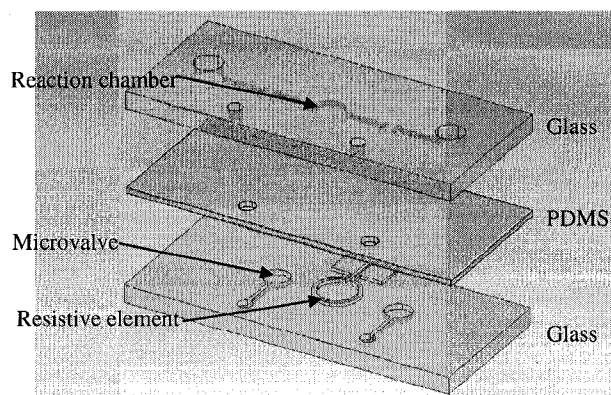
Figure 3-1. Microchip architecture (48 mm x 14 mm) used for the genetic amplification. The glass layers (both fluidic and control) are 1.1 mm thick while the PDMS is 254 μm thick. The reaction chamber is 90 μm deep and has a radius of 1.5 mm. Channels dimensions are 190 μm x 90 μm. The heater design and its placement with reference to other components were optimized to ensure temperature uniformity along the heater and in the reaction chamber.

We implemented a PD/PI controller that accurately controlled the chamber temperature (within ~1°C) during the steady-state. However, for the dynamic case (during transitions), it is challenging to determine the temperature accurately, a common scenario in microfluidics [3]. Here, TLCs are used to further characterize the dynamic behaviour

46

of the temperature within the reaction chamber at transitions between temperature stages to check for temperature overshoots and undershoots. Three sets of TLCs (R58C3W, R70C3W, R93C3W, Hallcrest Glenview, IL, USA) were used, each custom-synthesized to change reflected colour with a bandwidth of ~3°C around one of the typical desired chamber temperatures for each PCR stage. The reaction chamber is filled with a 1:2 dilution of the stock TLC suspension in water (we experimentally found that this TLC concentration yielded the strongest color signal without perturbing the TLC response), and the spectrum of the reflected light of the TLCs was observed using a spectrometer (Ocean Optics USB2000, Dunedin, FL, USA) in a setup similar to that used by Iles *et al.* [3]. As suggested by the manufacturer, the TLCs were viewed at a perpendicular angle (using an optical fiber attached to the spectrometer) and with a black (non-reflective) background to ensure colour changes were prominent. Illumination was provided by a white LED and the ambient fluorescent lights. The transition to each temperature stage was tested individually (the procedure described later is repeated thrice) using the appropriate set of TLCs. The reflected spectra of the TLCs were recorded every 100 ms (the actual temperature will vary on a time scale of seconds) as the microchip underwent PCR temperature cycling (i.e. cycling through all three temperature stages repeatedly) and subsequently related to temperature (described later in this section). Because a narrow colour change bandwidth of the TLCs (~3°C) was chosen, considerable intensity variations in the spectrum occur in a short temperature span, and this is sufficient to deduce the temperature of the TLCs to within ~1°C.

As seen by eye in reflected light under white light illumination, the TLC suspension has a milky white colour at room temperature. As it is heated, it changes colour successively (Table 3-1) before again turning white. The TLCs turn red as the temperature reaches the lowest temperature of its colour change range (e.g. 58.0°C for 58C3W), green at the second temperature threshold (e.g. at 58.6°C for R58C3W), and blue at the third threshold (e.g. at 60.8°C for R58C3W). When the temperature rises above the colour change range of the TLCs (~3°C bandwidth for the TLCs used here), their colour returns to the original milky white.

Table 3-1. The colour change ranges of the custom-synthesized TLCs.

TLC	Red	Green	Blue
R58C3W	58.0°C	58.6°C	60.8°C
R70C3W	69.7°C	70.6°C	72.8°C
R93C3W	92.4°C	93.6°C	95.8°C

When the TLCs are white, the spectrometer detects a background reflected spectrum consisting of strong peaks at the red (610 nm), green (535 nm), and blue (445 nm) wavelengths (Figure 3-2). We found that the background spectrum varied up to 10-20% between different runs due to slight variations in the positioning of the LED and optical fiber. Within a run, since the setup was not moved, the background spectrum generally remained constant (discussed below). To account for the different backgrounds between runs, spectra collected over time during a run were divided by the background spectrum obtained at the beginning of each run (i.e. for the spectrum at each time instant, the intensity at each wavelength is divided by the corresponding background wavelength intensity). This results in a 3D plot of relative spectra (relative intensities vs. wavelength) vs. time. In some cases, the intensity of the battery-powered LED decreased slightly during the run, causing the background intensities to show a steady decrease that was easily subtracted. The background level is represented by 1 and increases in intensity have a relative intensity greater than 1.
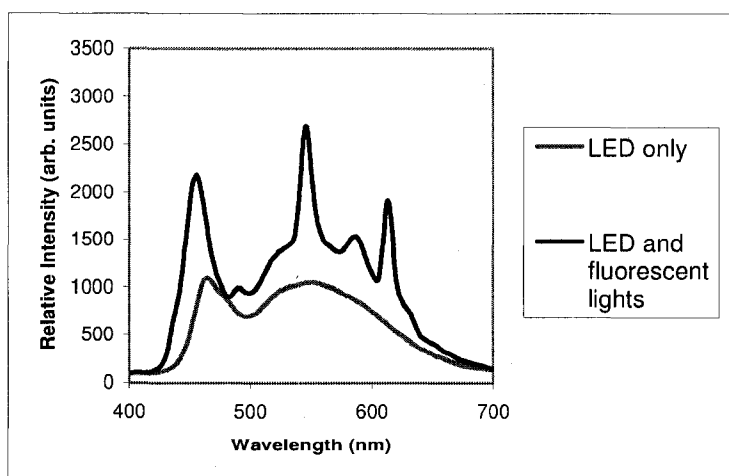
Figure 3-2. Background reflected spectrum when TLCs are white (no colour change) when within the PCR chamber and illuminated with a white LED and the ambient fluorescent lights at room temperature. The peaks are mainly due to the ambient fluorescent lights. As the TLCs change color from red to blue, a "wave" moves through this reflected spectrum from the red wavelengths to the blue wavelengths.

To extract temperature vs. time data from these relative spectra vs. time plots, we make use of the blue peak in the spectrum since it undergoes the largest intensity changes with temperature/colour, providing us with the largest sensitivity in temperature. Red and green peaks underwent smaller intensity changes and were hence not sufficiently sensitive [7]. The intensities over a bandwidth of ~15 nm around the blue peak (this corresponds roughly to its full width at half maximum) were averaged to reduce noise and subsequently plotted over time, yielding a plot of relative blue intensity over time. This plot was then normalized by dividing all relative intensities by the maximum relative blue intensity (B_{max}) reached throughout the run, yielding a plot of normalized blue intensity over time. Due to variations in illumination between different runs, this B_{max} value ranged from ~1.4-1.6. However, within a given run itself, the variation was less than 0.01. In the resulting normalized intensity vs. time plot (Figure 3-3), the maximum value is now 1 (represents B_{max}), and different runs done with the same temperature set-points showed a variation of less than 0.01 in normalized intensity. Hence, with this normalization performed on the data (dividing by B_{max}), we can compare the data from different experimental runs.

Normalized blue intensity vs. time plots were obtained for runs done with different temperature set-points to obtain a correlation between the normalized blue intensity and temperature (Figure 3-3a-c). Since the steady state temperatures are well-calibrated, we calibrate our dynamic method to the steady state method at points when the normalized blue intensity becomes constant with time. Hence, the value at which the normalized blue intensity settles is determined by the temperature set-point used (Table 3-2). We found that, as expected, B_{max} occurs approximately in the middle of the colour change range of the TLCs (e.g. ~72°C, Figure 3-3b). Hence, a given normalized blue intensity can be mapped to one of two different temperatures, one on the lower side of the colour change range and one on the higher side. To distinguish between the two, the normalized intensities of the red peak were plotted over time as well, following the same procedure that was applied to the blue peak (still normalizing to B_{max}). When the temperature is on the lower side of the TLC colour change range (e.g. 70°C, Figure 3-3a), there is an intensity increase in the red peak, and when the temperature is on the higher

side of the TLC colour change range (e.g. 74°C, Figure 3-3c), the red peak is at the baseline (no increase in intensity).
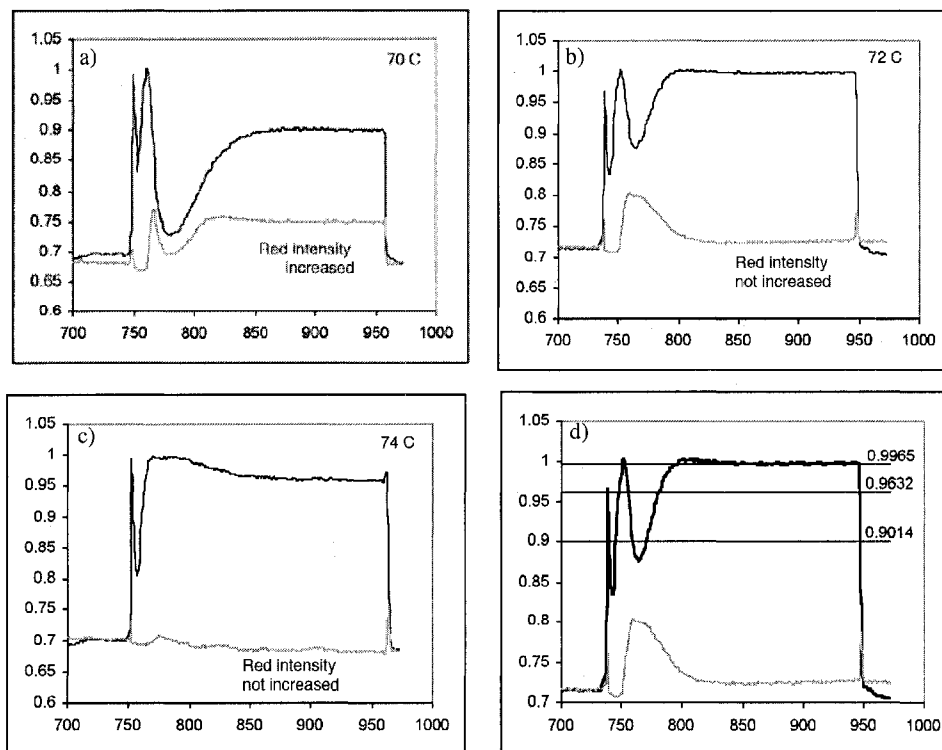
Figure 3-3. Normalized intensity vs. time plots for controller set-points at a) 70°C, b) 72°C, and c) 74°C. The black lines represent the blue peak and the grey lines represent the red peak. Though data was collected over two PCR cycles (3 temperature stages each), only the 72°C stage is shown here. In d) the normalized intensity vs. time used to determine the temperature crossing points for the transition from the 60°C to the 72°C stage is shown. The three horizontal lines represent the thresholds for 70°C, 72°C and 74 °C.

We found that the variation in TLC signal is quite small (compared with the measurement uncertainties) until the temperature nears the edge of the operating range of the TLCs whereupon the signal drops off rapidly. This means that the measurements near the desired temperature (at the centre of the operating range) provide relatively little information on the temperature vs. time behaviour and that most of this information is provided by the behaviour near the edges of the operating region. For example, when the temperature set-point is changed from 72°C to 71°C or 73°C, the resulting change in the normalized blue intensity was found to be ~0.01. Since the uncertainty in measuring the normalized blue intensity is also 0.01 (as determined earlier), these points provide little

information. Moving further away to 70°C or 74°C, a 1°C change in temperature corresponds to a larger change of ~0.02 or more in the normalized blue intensity. Hence, the 0.01 uncertainty in the normalized blue intensity corresponds to a smaller uncertainty of ~0.5°C in temperature (i.e. the temperature determined using the TLCs is within ~0.5°C of the set-point temperature). Temperature set-points located even further away from the temperature at which B_{max} occurs fell outside of the colour change range (bandwidth) of the TLCs and hence yielded no spectral change for analysis. As a result, three temperature set-points (the middle and edges of the TLC bandwidth) separated by steps of 2°C (sufficiently large to ensure the variation in normalized blue intensity was greater than its uncertainty) could be obtained and were correlated with normalized blue intensities (Table 3-2). The times at which the normalized blue intensity value crosses the correlated values were noted (Figure 3-3d), and translated into temperature crossing points. We obtain a temperature crossing point every time the normalized blue intensity vs. time plot crosses one of the values correlated with temperature. For example, in Figure 3-3d, every time the plot crosses 0.9014 and the red peak is present, we know the temperature has crossed 72°C. The temperature and its time derivative must be continuous, and the PI/PD controller algorithm ensures that the temperature is slowly varying (changes of 1°C/s or less) as it approaches the set-point value. Near any one extremum we could readily fit a quadratic (i.e. a parabolic curve), but with successive extrema we need a higher order polynomial in order to take into account the nearby extrema. It is well-known that the higher the order of polynomial the more likely one is to obtain spurious fluctuations. The lowest order polynomial that could fit the observed behaviour is a cubic. Hence, we fitted a cubic spline to these crossing points to obtain an estimate of the temperature versus time trajectory during the transitions between temperature stages.

Table 3-2. Correlation of the normalized blue peak intensity to temperature

Set-point temperature	Normalized blue peak intensity
70°C	0.9014
72°C	0.9965
74°C	0.9632

3.3 RESULTS AND DISCUSSION

For all the temperature transitions, we found that the temperature controller could be fine-tuned to find a good balance between speed and overshoots/undershoots in the chamber temperature. Figure 3-4a is representative of the results of such tuning: during the denaturation stage of the PCR the chamber temperature just touches 96°C (only one crossing point) and the undershoot is below 92°C (two crossing points). This overshoot was deemed acceptable (too low to boil or cause extensive degradation of the enzyme) and the undershoot is thought to be of little consequence. However, without fine-tuning the temperature controller, overshoots or undershoots could be much larger and could impair operation. Figure 3-4b is representative of an untuned transient and shows the temperature versus time of the chamber during the annealing stage of the PCR, indicating that the chamber temperature overshot by 5°C to about 55°C (two crossing points at 58°C) before settling back to 60°C. In general, this is not acceptable as such an overshoot is likely to cause non-specific amplification (this is application specific). The present TLC method can hence be used as feedback for fine-tuning the controller. The transients found here were not substantial enough (for this application) to be detrimental to the amplification of the $\beta2$ microglobulin ($\beta2M$) gene (as in Chapter 2) but they are significant enough to affect highly temperature sensitive reactions [1, 2].
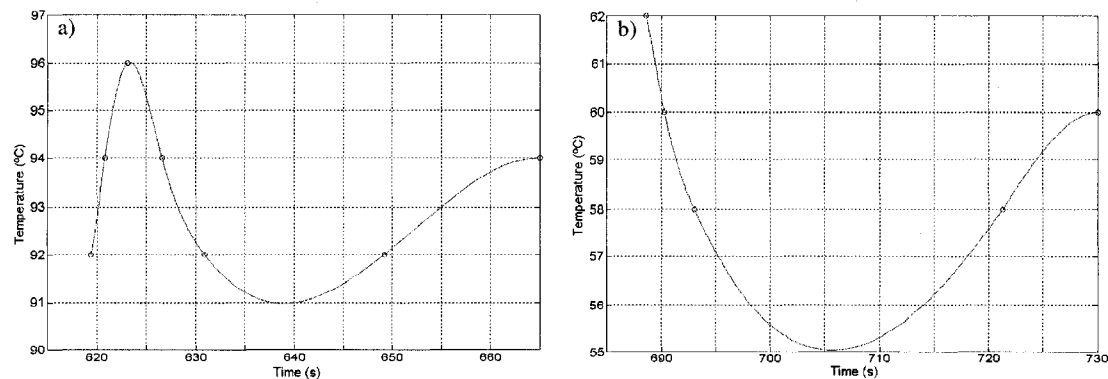
Figure 3-4. Chamber temperature estimates and the dynamic trends as captured by the optical spectra of the TLCs during the transition a) from the 72°C stage to the 94°C stage and b) from the 94°C stage to the 60°C stage. For PCR, accurate temperature control is the most critical for these two transitions. The temperature controller had been fine-tuned in a), but not in b).

3.4 CONCLUDING REMARKS

The present design is a suitable test-case for our dynamic TLC-based method: the volumes are relatively large (to ensure that sufficient template DNA is available when using clinical samples) and the bulk material is low-conductivity glass, resulting in long equilibration times and large temperature differences. These temperature differences may be small for high conductivity materials such as silicon, but tens of degrees are common in glass-based applications [5]. Even larger temperature differences would be expected for polymer-based devices (lower thermal conductivity than glass). It is common that a sensed value of temperature at one point is used to determine the heat that should be applied at a second, often different point. As a result, we feel that the results found here are likely to be representative of the transients on many miniaturised PCR systems, particularly glass-based ones like the microchip studied here. In the present work, the slow settling to the steady state (over ~60s) results from the fact that a large unused region of the chip communicates thermally with the reaction chamber and comes to equilibrium gradually. Though the magnitude of the resulting overshots/undershoots was not large enough to affect our application (β2M), they may be detrimental to more temperature sensitive reactions.

It has been noted [5] that for temperature accuracy, one requires tight-bandwidth TLCs, however such TLCs do not provide any information on the temperature beyond their bandwidth. There is clearly a significant benefit to estimating a temperature vs. time trajectory in a method that allows the use of tight bandwidth TLCs while monitoring for large transients (beyond the bandwidth) that may impair reliability. To improve the accuracy of the method, more data points might be obtained with lower uncertainties and analysed with a non-linear least squares method. Given the sensitivity of the PCR process to such transients, dynamic characterisation methods are needed in order to realize clinical-grade LOC PCRs. The methodology presented here may be automated to facilitate the fine-tuning of temperature controllers to reduce overshoots/undershoots.

3.5 REFERENCES

[1]   Wittwer, C.T. and D.J. Garling, "Rapid cycle DNA amplification: time and temperature optimization", *Biotechniques*, 1991. **10**(1): p. 76-83.

[2]   Sadler, D.J., R. Changrani, P. Roberts, C.-F. Chou, and F. Zenhausern, "Thermal management in bioMEMS: temperature control for ceramic-based PCR and DNA detection devices", *IEEE Transactions on Components and Packaging Technology*, 2003. **26**(2): p. 309-316.

[3]   Iles, A., R. Fortt, and A.J. de Mello, "Thermal optimisation of the Reimer-Tiemann reaction using thermochromic liquid crystals on a microfluidic reactor", *Lab on a Chip*, 2005. **5**: p. 540-544.

[4]   Chaudhari, A.M., T.M. Woudenburg, M. Albin, and K.E. Goodson, "Transient liquid crystal thermometry of microfabricated PCR vessel arrays", *Journal of Microelectromechanical Systems*, 1998. **7**(4): p. 345-355.

[5]   Noh, J., S.W. Sung, M.K. Jeon, S.H. Kim, L.P. Lee, and S.I. Woo, "In situ thermal diagnostics of the micro-PCR system using liquid crystals", *Sensors and Actuators A*, 2005. **122**: p. 196-202.

[6]   Liu, J., M. Enzelberger, and S. Quake, "A nanoliter rotary device for polymerase chain reaction", *Electrophoresis*, 2002. **23**(10): p. 1531-1536.

[7]   *Handbook of thermochromatic liquid crystal technology*. Hallcrest Inc., Glenview, IL, USA, 1991.

Chapter 4

Practical strategies for enhancing the speed of microchip genetic amplification implementations

4.1 INTRODUCTION

Molecular biology offers many useful techniques for disease diagnostics, but in their conventional form, their cost and complexity limit their practical use outside of a laboratory setting. As a result, there has been substantial effort to miniaturize these techniques onto microfluidic platforms to improve speed, automation, portability, and cost-effectiveness (as reviewed by [1, 2]), moving towards a diagnostic and/or disease monitoring tool suitable for routine use in a clinical setting or in other point-of-care applications. The polymerase chain reaction (PCR) is one such molecular biology technique that is used to amplify the minute amounts of DNA present in clinical samples to levels that can be detected and analyzed by low-cost technologies. Hence, it is key to lab-on-a-chip (LOC) devices. PCR involves thermally manipulating DNA and enzymatic activity by repeatedly cycling a reaction mixture through distinct temperature stages. For high-yield PCR, temperature uniformity, accurate temperature control, and rapid transitions between temperature stages are all critical [3, 4].

The first demonstrations of microchip PCR tended to be made from silicon [5-12] to take advantage of its favourable thermal properties and the versatility and maturity of silicon-based microfabrication [1]. The high thermal conductivity of silicon (157 W/m·K [1]) allows

for uniform temperature distributions and rapid temperature ramping rates, resulting in impressive heating rates of up to 175°C/s and cooling rates of up to 125°C/s [13]. However, silicon is not as suitable for several other molecular biology/analytic techniques. As an example, capillary electrophoresis (CE), a technique commonly used following PCR to detect and analyze amplified DNA fragments, requires high electric fields that silicon will not sustain, as well as fluorescence detection typically at optical wavelengths to which silicon is opaque [1, 14]. In contrast to silicon, glass is compatible with a wider range of biochemical techniques, including CE, and hence, as the focus for on-chip PCR shifted towards integration with other analytical functionalities, more recent demonstrations of microchip PCR make use of glass-based devices, particularly those that integrate fluorescence detection technologies such as CE along with PCR [15-24]. However, since the thermal conductivity of glass (1.1 W/m·K [1]) is much lower (~150x) than that of silicon, temperature ramping rates in glass-based microfluidics tend to be orders of magnitude lower than those of silicon-based devices. Polymers, such as polydimethylsiloxane (PDMS), are another common choice of material for LOC devices on account of their biocompatibility and amenability to rapid prototyping [1]. Since their thermal conductivities are an order of magnitude lower than that of glass (0.18 W/m·K for PDMS [1]), polymer-based devices would have even slower thermal transients. Hence, in order to take advantage of the biochemical versatility of glass/polymer-based devices, the challenge of dealing with low thermal conductivities needs to be addressed. The work in this chapter is based on a manuscript in preparation.

Both the Landers and Mathies group have been successful in achieving relatively fast temperature ramping rates in glass/polymer-based devices. The Landers group has demonstrated that by using infrared heating (50 W infrared lamp) and active forced convection cooling (fan or compressed air), heating and cooling rates of 10-20°C/s are achievable in glass and polymer-based devices with μL-sized reaction chambers [25, 26]. These strategies are impressive and demonstrate that fast thermal transients can be achieved with relatively large reaction volumes in glass-based microchips. Very recently, the Landers group have also demonstrated that by coupling their heating and cooling strategies with thermal isolation techniques and a smaller 270 nL reaction chamber, they can achieve even higher temperature ramping rates (~25°C/s) in glass-based microchips [14]. However, since

we are directing our efforts towards developing low power, portable and inexpensive systems for use as point-of-care devices, our applications demand strategies requiring less substantial peripheral instrumentation and power. The Mathies group has developed a more compact and less power intensive heating scheme for glass-based microchip PCR that relies on integrated resistive thin film elements, and have demonstrated heating and cooling rates of ~10-20°C/s for a 200 nL reaction volume with active cooling (blown air) [15]. With passive cooling, they have achieved cooling rates of ~5°C/s [23]. Though we use a similar resistive element-based strategy, since we are directing our microchips to handle clinical samples that require a larger reaction volume to accommodate low analyte concentrations (e.g. microchip viral analysis using urine [27]), the larger thermal mass dictated by our applications limits our temperature ramping rates. We therefore require alternate strategies for improving thermal cycling speed that require less peripheral instrumentation and power consumption (e.g. resistive elements and passive cooling) and are applicable to larger reaction volumes.

We recently demonstrated a glass-based microfluidic chip for performing PCR that utilizes a single resistive thin film element as both a heater and a temperature sensor (chapter 2), rather than using two separate elements as used in several other demonstrations [6-12, 16-21]. We have addressed aspects accurate temperature control and uniformity (chapter 2), low power consumption (chapter 2) and portability [24], and with similar microchips/platforms, we demonstrated applicability in cancer [28] and viral detection [27]. However, the thermal management system is relatively slow, and hence, in the present work, the goal is to increase the rapidity of PCR in this glass-based microchip that utilizes a relatively large reaction chamber (~600 nL) to accommodate clinical samples, as well as only passive means of cooling to ensure low power consumption and to simplify the peripheral instrumentation by avoiding active cooling elements. The heating rates within the reaction chamber were fairly rapid (~10°C/s) in our earlier demonstration (chapter 2), but cooling rates were relatively slow (~2°C/s) since heat dissipation from the microchip relied solely on natural convection. Hence, the passive cooling rate may therefore limit the widespread usage of this microchip, as well as other similar glass or polymer-based PCR microchips.

The passive cooling rate of the microchip can be improved with the implementation of a heat sink. To date, the usage of a heat sink in the context of LOC devices has only been well explored by Yang *et al.* [12], but for silicon-based PCR. In this demonstration, thermal conduits are used to selectively heat-sink only the desired low temperature areas while leaving desired high temperature areas (i.e. the vicinity of the resistive element and the heated reaction chamber) not heat-sunk. The heat sink provides an alternative path for heat dissipation that is substantially less resistant to heat flow than natural convection. Additionally, the heat sink redirects heat flow away from regions that do not require heating reducing the size of the heated volume in the microchip and hence its effective heat capacity. These two effects shorten the equilibration time of temperature transients in the microchip.

Additionally, to further improve the thermal cycling speed of the microchip, we also adapted the PCR thermal cycling protocol. In conventional PCR protocols using bench-top thermal cyclers, 30 s long dwell times are typically used for each of the three temperature stages, typically because they allow sufficient time for temperatures in the relatively large (~25 µL) PCR samples to equilibrate [4]. With such PCR dwell times, even in an idealized situation where the temperature transition stages could be made instantaneous, a typical 35 cycle PCR would still require ~1 hour to complete. Hence, to achieve PCRs shorter than an hour, we will certainly need to make protocol adaptations in addition to the instrumentation-based strategies for speeding up the heating and cooling stages (e.g. heat sink implementation). Two independent approaches are implemented here: 1) combining two PCR temperature stages into one, and 2) substantially reducing the time spent at each stage and customizing to specific applications.

With both instrumentational and protocol adaptation strategies employed, microchip PCR was performed ~3 times more rapidly than in the unoptimized system demonstrated in chapter 2 while yielding comparable results. Despite using a relatively large reaction volume for handling clinical samples with low analyte concentrations, 35 PCR temperature cycles could be completed in ~30 minutes within glass-based microfluidics. Though the speed optimization strategies presented are applied to a specific microchip design here, the same principles can be applied to any lab-on-a-chip device.

4.2 MATERIALS AND METHODS

4.2.1 Microfluidic chip and heat sink architecture

The microchip architecture used here is the same as in chapter 2, comprising of a glass/PDMS/glass structure (Figure 4-1) for forming pneumatically-actuated valves based on the work of Grover *et al.* [29]. A platinum/titanium (Pt/Ti), ring-shaped resistive element patterned on the lower glass layer provides heat for thermally cycling a ~600 nL reaction chamber located in the top glass layer. The geometry and positioning of the various microchip components were as designed in chapter 2 to ensure that temperature variations are negligible along the length of the resistive element (allowing it to function simultaneously as a heater and a temperature sensor) and within the reaction chamber (required for high yield PCR). Details on the design, fabrication, and operation of this PCR microchip may be found in chapter 2 (optimized for temperature uniformity and for handling clinical samples, but not for speed).

The heat sink used here is comprised of a 5 inch x 2.5 inch, 0.5 inch thick polished copper block. The size of the copper block was chosen such that its heat capacity was sufficiently large to ensure its temperature did not substantially increase when absorbing the heat generated during operation of the microchip (i.e. a large heat reservoir). The size of the copper block could be shrunk if cooling fins were employed. The vicinity of the reaction chamber and the resistive element were insulated by placing them over a shallow trench (1 mm deep) machined into the surface of the copper block. These regions were not heat-sunk to avoid greatly hampering heating rates and increasing power consumption (as described later in section 4.3.2). A thin coating (estimated to be <1 μm thick and thus has a negligible thermal resistance relative to the microchip) of silicone heat transfer compound (MG Chemicals, Toronto, ON, Canada) was applied to the rest of the microchip to ensure good thermal contact with the heat sink.

4.2.2 Microchip model implementation

Finite element modeling (COMSOL Multiphysics 3.2, COMSOL Inc., Los Angeles, USA) was used to simulate the microchip for design purposes, as well as to assist in characterizing the microchip (as described in chapter 2 and in section 4.2.3). Taking advantage of the circular symmetry of the reaction chamber and resistive element, a 2D axisymmetric model of the microchip (Figure 4-1) was used to allow the heat sink position to be easily modified and simulations to be completed rapidly. The material properties used are listed in Table 4-1. The distance to the closest edge in the actual microchip is used as the maximum radius considered in the model. Since PCR is performed in an aqueous environment, the chamber is assumed to be filled with water in the FE model. Boundary conditions are chosen to closely match the experimental set-up/environment in which the microchip is operated. The heat-sunk regions on the bottom surface of the microchip are modeled as a constant temperature boundary at the temperature of the heat sink. For design purposes, the copper block was considered to be a perfect heat sink with a temperature equal to room temperature (22°C), but for assisting in temperature calibration or verification, the actual heat sink temperature was experimentally measured and used to refine the model (detailed in section 4.5.1). The area of the bottom microchip surface below the reaction chamber, which is not heat-sunk (i.e. located above the trench on the copper block heat sink), is modeled as a thermally insulated boundary. All other external boundary conditions on the microchip are set to natural convection (heat transfer coefficient = 5.6 W/m^2·°C [30]). Since this is a simple 2D axisymmetric model, the ring-shaped resistive element is reduced to a line (width of the ring) with a defined temperature.
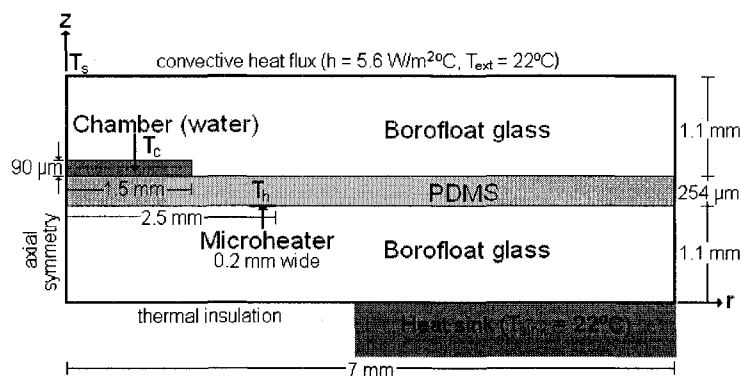
Figure 4-1. 2D axisymmetric model of the PCR microchip used in this study

60

Table 4-1. Material properties used in FEM

Material	Thermal Conductivity (W/m·K)	Specific Heat Capacity (J/kg·K)	Density (kg/m³)
Borofloat glass [31]	1.11	830	2200
PDMS [32]	0.18	1100	1030
Water [31]	0.58	4187	1000
Platinum [31]	72	133	21500

A more detailed 3D model of the microchip was also used to consider the fact that the heater ring is not a complete circle (the axial symmetry is broken where the heater ring connects to the electrode pads, as discussed later in section 4.3.5) as well as to model resistive Joule heating and study voltage and power requirements. The complete microchip was simulated in the same manner as described in chapter 2, and the same external boundary conditions as described earlier for the 2D model were applied. The temperature of the resistive element is now set by applying an electrical voltage/current to the electrode pads.

4.2.3 Temperature calibration

The resistive element of the PCR microchip measures its own temperature (T_h), but for PCR, the temperature of the reaction chamber (T_c) is what must be controlled precisely. The relationship between T_h and T_c is therefore required. Although the same microchip as in chapter 2 was used here, since the microchip environment is altered with the implementation of a heat sink, the relationship between T_h and T_c must be redetermined. As described in chapter 2, both experimental measurements and FEM calculations were used to establish this relationship. Briefly, T_h and T_s values were measured experimentally and used as boundary conditions in the FE model of the microchip to calculate an estimate for the corresponding T_c values (as determined in chapter 2, since the thermal resistance due to natural convection is much larger than that due to thermal conduction within the microchip, the offset between T_s and T_c is 10°C or less, allowing T_c to be accurately predicted using measurements of T_s). The resulting T_c vs. T_h relationship was used to control T_c on the basis of measuring T_h, and the accuracy of the temperature control was verified by ensuring measured T_s values matched those predicted by the FE model, and by using thermochromic liquid crystals (as described in chapter 3).

4.2.4 RT-PCR mixture

The RT-PCR reaction mixture (for amplifying the β2 microglobulin gene) consists of the following in 25 μL: 5 μL H$_2$O, 12.5 μL 2X reaction mix (Invitrogen, Carlsbad, CA, USA), 5 μL 5 mM MgSO$_4$, 0.5 μL 10 μM forward primer (CCA GCA GAG AAT GGA AAG TC), 0.5 μL 10 μM fluorescently VIC-labelled reverse primer (ACT TAA CTA TCT TGG GCT GTG AC), 0.6 μL 10 mg/mL BSA (Sigma-Aldrich, St. Louis, MO, USA), 0.5 μL enzyme mix, and 0.4 μL 1 μg/mL template RNA (purified clinical sample). To substantially reduce the thermal cycling time, as explained later in section 4.4.4, the thermal cycling program consisted of: a reverse transcription stage of 45°C for 10 min., a pre-denaturation stage of 94°C for 1 min., 35 cycles of 94°C for 5 s and 60°C for 10 s, and a post-extension stage of 68°C for 1 min.

4.2.5 Microchip capillary electrophoresis

Following microchip RT-PCR, capillary electrophoresis was performed on a Microfluidic Tool Kit (μTK, Micralyne, Edmonton, AB, Canada) to detect and analyze the amplicons. The PCR products from the microchip are loaded onto a glass CE microchip (Micralyne, Edmonton, AB, Canada), CE was performed using an injection voltage of 0.4 kV and separation voltage of 6 kV. The sieving matrix used within the CE microchip was 5% Genescan polymer (Applied Biosystems, Foster City, CA, USA) with 10% glycerol and sizing of the PCR product was done by running it along with GS500 size standard (Applied Biosystems). Further details can be found in [33].

4.3 HEAT SINK DESIGN

4.3.1 Electrically equivalent circuit

It is common to use electrical analogies to help understand thermal systems since the underlying behaviours are similar [34, 35]. Heat conduction can be modeled as a network of parallel RC circuits (further elaboration in Appendix A), with temperatures being analogous

to voltages (potentials) and heat flows being analogous to electrical current (energy flow). Heat capacities and thermal conductivities/resistivities are analogous to electrical capacitances and conductivities/resistivities. The total heat capacity of a heated volume V can be calculated using equation (4-1) [35] knowing the density ρ and specific heat capacity c of the material in question, assuming the temperature of the heated volume is uniform. A higher specific heat capacity or a larger heated volume yields a larger thermal capacitance.

$$C = \rho c V \qquad (4\text{-}1)$$

Similarly to electrical resistances, thermal resistances for conduction depend on the thermal conductivities/resistivities of the materials in the system and on a geometrical factor. The thermal resistance for conduction increases as the thermal conductivity (k) of the material decreases, the cross-sectional area (A) decreases, or the length (L) over which conduction occurs increases. For simple geometries, thermal resistances can be calculated analytically (e.g. $R_k = L/kA$ for perpendicular heat flow between to planes). Due to the cylindrical geometries of the microchip considered here, it is useful to consider the thermal resistance associated with radial heat conduction between two concentric cylinders (outer radius r_2, inner radius r_1, height l, separated by a material with thermal conductivity k) [35]:

$$R_{k,cyl} = \frac{\ln(r_2 / r_1)}{2\pi k l} \qquad (4\text{-}2)$$

Thermal resistances associated with convection can be calculated knowing the heat transfer coefficient h (depends on properties of the surrounding fluid such as its velocity) and the area A over which convection occurs. As shown in equation (4-3) [35], the thermal resistance due to convection decreases if a larger surface area is provided for it to occur or if the heat transfer coefficient is increased (e.g. faster air flow). For natural convection in air, the heat transfer coefficient is commonly taken as 5.6 W/m$^2\cdot°$C [30].

$$R_h = \frac{1}{hA} \qquad (4\text{-}3)$$

The simplest model for a thermal system is a lumped model, where a single resistance and a single capacitance are assigned to a body (i.e. only one parallel RC circuit rather than a network). This model assumes the temperature distribution of the body in question is uniform, and therefore most accurate if this condition is true. A lumped model of the microchip under consideration (Figure 4-2) can be used to analytically estimate the time constant for thermal transitions in the reaction chamber. For an electrical parallel RC circuit, the characteristic response time can be estimated from the solution of a first order differential equation (time constant $\tau = RC$). Since heat transfer in the microchip is governed by equations with a similar form, this solution is equally valid here.

To enable a simple analytical calculation, the heated volume used to calculate the thermal capacitance (C) of the lumped model (using equation (4-1)) is approximated to be the volume of the microchip enclosed by the heat sink (i.e. cylinder with radius r as in Figure 4-2). Regions outside of this volume are considered to be maintained at room temperature by the heat sink and hence not part of the heated volume (simulations show that this is a reasonable assumption).

Two parallel thermal resistances are considered since there are two parallel paths for heat to dissipate from the reaction chamber to room temperature: via conduction to the heat sink (R_k) and via natural convection to the ambient environment (R_h). Because of the relatively small lengths involved in microfluidic chips (mm scale), thermal resistances associated with conduction are much smaller than those associated with natural convection [14] (this is verified shortly). As a result, heat primarily flows along the lowest resistance path radially towards the heat sink, rather than vertically and dissipating through the top surface of the microchip (simulations show the same behaviour). Therefore, conduction is taken as occurring only radially from the edge of the reaction chamber to the edge of the heat-sunk region, allowing equation (4-2) to be applied to calculate R_k (Figure 4-2). As for R_h, the area of the considered heated volume (circle with radius r in Figure 4-2) is used in equation (4-3). The heat-sunk regions are considered to be at room temperature and therefore no convection occurs here, as there is no temperature difference to drive the heat transfer.

$$C = \rho c \pi r^2 l \qquad R_k = \frac{\ln(r/r_c)}{2\pi k l} \qquad R_h = \frac{1}{h\pi r^2}$$

$$R = \left(R_k^{-1} + R_h^{-1}\right)^{-1}$$
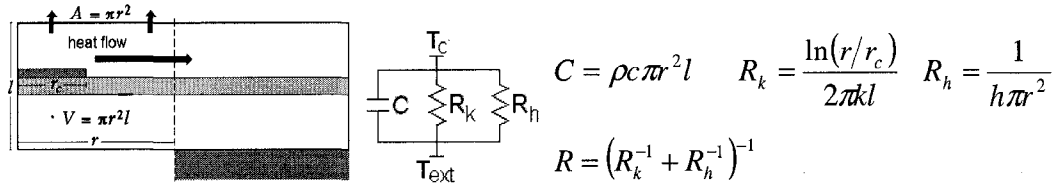
Figure 4-2. Lumped model of the microchip with associated analytical equations

By substituting the thermal conductivity for glass (Table 4-1), the heat transfer coefficient for natural convection and considering distances on the mm scale, we find that R_h is three orders of magnitude smaller than R_k (the earlier assumption was correct). Hence, heat flow in the microchip is dominated by conduction to the heat sink and the convective term can be neglected. With this simplification, the thermal resistance of the system (R) is just R_k. Multiplying this with C to obtain the time constant (τ) and again substituting the thermal properties of glass (Table 4-1) yields the following:

$$\tau = R_k C = \left[\frac{\ln(r/r_c)}{2\pi k l}\right]\rho c \pi r^2 l = \frac{\rho c r^2}{2k}\ln(r/r_c) \approx \frac{\rho c r^2}{2k} \tag{4-4}$$

$$\tau \approx r^2 \left(10^6\right) \tag{4-5}$$

The time constant of the microchip therefore scales quadratically with the radius of the non-heat-sunk area, and hence depends strongly on the size of the heated volume of the microchip (its effective thermal mass), which is reduced by the heat sink. Placing the heat sink at $r = 3$ mm (a bit larger than the radius of the resistive element) yields a time constant on the order of 10 s. In comparison, a similar lumped analysis for the case of no heat sink (see Appendix A, the thermal resistance is dominated by convection and the entire microchip is used as the heated volume to calculate the capacitance) yields a time constant on the order of ~9 minutes. Therefore, the implementation of a heat sink greatly reduces the time constant of the microchip from minutes to seconds, and thus allows for faster thermal transients and shorter equilibration times. This scale of reduction in the time constant was observed as well both in simulations, which are more accurate as they can take into account more complex geometries and temperature distributions (i.e. treat a network of parallel RC circuits instead of only one), and in experimental results.

65

4.3.2 Heat sink placement

Though placing the heat sink closer to the reaction chamber results in faster cooling rates in the reaction chamber, placing it too close to the resistive element would result in a substantial portion of the heat generated by the resistive element being lost to the heat sink, decreasing heating rates and increasing power consumption. Yang *et al.* found that for silicon-based devices, including a trench to provide thermal isolation between the heat-sunk regions and the desired high temperature regions counteracted these undesirable effects by reducing the amount of heat lost to the heat sink [12]. Nevertheless, glass is not as amenable to the introduction of trenches as silicon, and more importantly, the fabrication of trenches may be complex and costly (ease of manufacture is a key goal). However, since glass possesses a much lower thermal conductivity than silicon, it provides significantly higher thermal resistance, which becomes an advantage in this case since the same effect of thermal isolation obtained from introducing a trench in silicon can be achieved in glass by providing adequate spacing between the heat-sunk regions and the desired high temperature regions.

Finite element modeling (FEM) was used here to simulate a heat sink implemented onto the PCR microchip developed in chapter 2 and determine a suitable placement for the heat sink which substantially improves the passive cooling rate of the reaction chamber without drastically decreasing the heating rate or increasing power requirements. The temperature of the resistive element was set to 200°C (approximately the maximum available temperature for heating, limited by the melting point of the PDMS layer) for 10 s to simulate heating, following which the microchip is allowed to cool passively. The resulting temperature in the reaction chamber was then plotted over time (Figure 4-3) and heating and cooling rates inside the reaction chamber were compared for different distances (d) between the resistive element and the heat sink. We found that placing the heat sink 1 mm away from the resistive element (i.e. r = 3.5 mm) was suitable for the glass/PDMS/glass microchip architecture considered here (it will vary with the thermal conductivities and thicknesses of the microchip materials). In the actual implementation of the heat sink, to account for the fact that the region where the heater ring is connected to its electrode pads is not heated, the non-heat-sunk region is extended by a 2 mm wide slot (1 mm on each side) in this region.
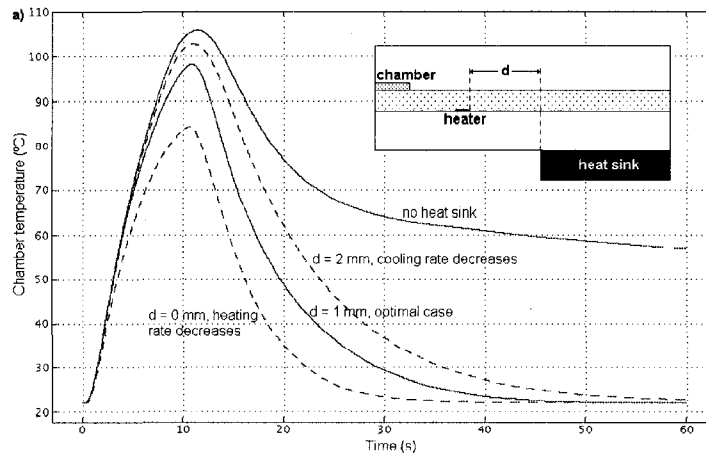
Figure 4-3. Design of the heat sink position using FEM. The distance d between the outer radius of the heater and the edge of the heat sink was varied and T_c was plotted over time for two cases. T_h was set to 200°C for 10 s and then set to cool passively. It was found that d = 1 mm roughly doubled the cooling rate without significantly increasing the heating rate compared to the case with no heat sink. Increasing d lowered the cooling rate while decreasing d lowered the heating rate.

4.3.3 Effects of the heat sink on thermal control

Since steady-state can be achieved much more rapidly, the use of a heat sink facilitates temperature control (and rapid thermal cycling), helping to reduce overshoots and undershoots which can potentially cause erroneous PCR results [3, 4]. To illustrate this effect, the operation of the microchip with and without a heat sink was simulated and the T_c vs. time plots were compared (Figure 4-4). As described in chapter 2, during heating, the temperature controller used initially applies a large T_h (the heating stage) to achieve a high heating rate in T_c (T_c takes several time constants to equilibrate otherwise). Once T_c approaches the desired value, T_h is then reduced to the temperature required to maintain the desired T_c. This control scheme is approximated in the simulations as two temperature steps in T_h: a high temperature one that represents the heating stage and then a lower one that maintains the desired T_c (94°C in Figure 4-4). The temperature and duration of the heating stage in the simulations are adjusted to minimize the temperature overshoots/undershoots in T_c as much as possible. Figure 4-4 shows that significant overshoots/undershoots can be eliminated with a heat sink in place, while a gradual fluctuation in T_c is present and cannot be eliminated when no heat sink is in place. When no heat sink is implemented, heat travels

throughout the entire microchip, whose equilibration time is much longer than the duration of the heating stage. Therefore, at the end of the heating stage, though the vicinity of the chamber has reached a temperature close to its steady-state temperature, further regions of the microchip are still far from steady-state as sufficient heat has not yet traveled to them. As a result, when T_h is decreased (after the heating stage) to avoiding an overshoot (since T_c has already approached the desired value), an undershoot is observed in T_c because a portion of the injected heat is used to bring the remainder of the microchip to steady-state rather than to maintain T_c. Attempting to bring the far regions of the microchip closer to steady-state by elongating the heating stage would result in a substantial overshoot in T_c. Therefore, the slow equilibration time in the case of no heat sink causes a substantial delay in the response of the microchip temperatures to changes in T_h, resulting in unavoidable fluctuations in T_c unless a longer heating stage (comparable to the equilibration time of the entire microchip) is employed. On the other hand, when a heat sink is in place, only the vicinity of the chamber is being heated, and this smaller thermal mass has an equilibration time comparable to the duration of the heating stage. When T_c approaches its desired value at the end of the heating stage, the temperature distribution throughout the entire microchip is already close to its steady-state case since the far regions are not heated. Since the far regions of the microchip do not participate, they do not cause a fluctuation in T_c at the end of the heating stage.
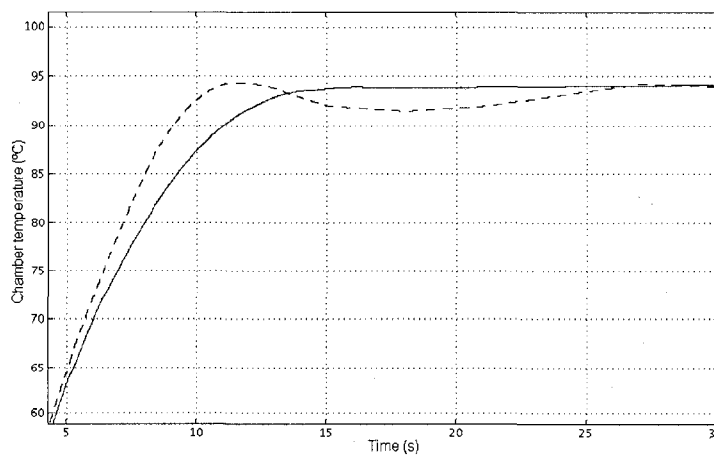
Figure 4-4. Simulation of T_c vs. t for microchip with (solid line) and without (dashed line) a heat sink, where the heating stage is simulated by changing the temperature of the resistive element in two steps (tuned to minimize fluctuations in both cases). Small fluctuations seen in T_c when no heat sink is implemented are eliminated with the heat sink in place.

4.3.4 Effects of the heat sink on power consumption

To investigate power consumption issues, the microchip with a heat sink at d = 1 mm was modeled in 3D and resistive Joule heating was simulated. We found that applying ~2 W of power (a current of 150 mA) to the resistive element was sufficient to attain a T_c of 95°C, which is the maximum temperature required for most PCRs. Without a heat sink, the same T_c can be attained with ~1 W of power (a current of 100 mA). Nevertheless, although the power consumption of the microchip had been increased by the implementation of a heat sink, the increase was low enough such that PCR could still be performed using reasonable power requirements (under 20 V and 200 mA, the same design requirement as in chapter 2) suitable for portable and inexpensive platforms (as in [24]). Miniaturizing the reaction chamber further would lead to even lower power consumption (discussed in Chapter 5).

4.3.5 Effects of the heat sink on temperature uniformity

The 3D model was also used to characterize temperature distributions throughout the PCR microchip and verify if temperature uniformity was maintained along the resistive element (required for accurate temperature measurement) and within the reaction chamber (required for high yield PCR). It was found that the temperature distribution dipped significantly (>1°C) in the area where the heater ring meets the electrode pads (Figure 4-5a). This area is not heated since the heater ring is not a complete circle due to the need for electrical connections. The proximity of the heat sink in this area therefore lowers its temperature relative to the other areas near the heater ring, thus disrupting the temperature uniformity with in the chamber. We overcame this problem by introducing a slot to the trench in the copper block as depicted in Figure 4-5b, effectively moving the heat sink away from where the electrode pad connections are made (Figure 4-5b). Through simulations, for the microchip architecture considered here, it was found that a slot width of 2 mm restored temperature variations along the heater ring and in the reaction chamber to be within 1°C. A narrower slot was not enough to reduce the temperature dip near the electrode pads, while a wider slot removed far too much of the heat sink effect and allowed the area to become relatively hotter than other regions.

a)

b)
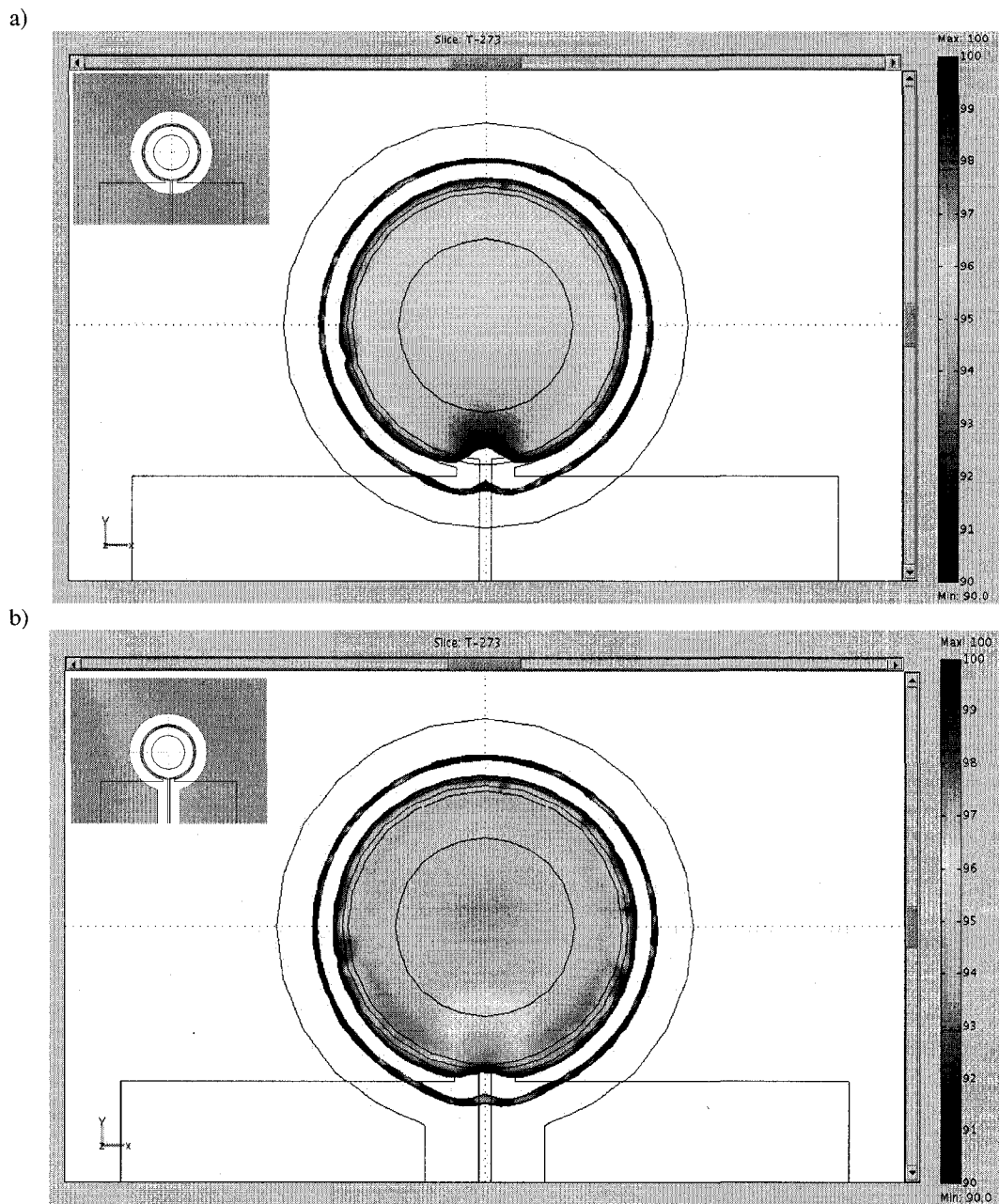
Figure 4-5. Simulation of temperature distribution in the reaction chamber with the heat sink implemented.

a) The heat-sunk region is on the outside of a 3.5 mm radius centered on the reaction chamber (colored region in the inset). The area of the chamber near the electrode pad connections of the heater is ~3°C lower than the rest of the chamber. Note that the decreased temperature due to the heater geometry (not a complete circle) and not due to the electrode pads since their size is relatively much too small for them to act as significant heat sinks.

b) A 2 mm wide slot is added to the non-heat-sunk region (heat-sunk region is the colored region in the inset). The temperature in the reaction chamber is now uniform to within 1°C.

70

4.4 PCR PROTOCOL OPTIMIZATION

4.4.1 Two-stage PCR

The three-stage PCR approach consists of the denaturation stage, where template DNA duplexes are separated into single strands, the annealing stage, where primers attach themselves to the template, and the extension stage, where the replicating enzyme (Taq) builds a new complementary strand using supplied nucleotides. Instead of this typical three-stage approach, we implement here a shorter two-stage approach to PCR [36] where the annealing and extension stages are combined into one stage at the same temperature (Figure 4-6). PCR can still be performed with comparable performance using the two-stage approach since the replicating enzyme still functions near the annealing temperature [36], albeit at a lower incorporation rate [37] (~30 nucleotides/s at ~60°C, roughly half the rate at ~70°C for Taq). Therefore, as long as sufficient time is given for the Taq to complete the replication of the DNA template, the two-stage PCR will be successful. To further reduce the thermal cycling time, it is also possible to design primers with an annealing temperature closer to the optimal operating temperature for Taq to achieve a faster incorporation rate. Hence, to realize two-stage PCR, careful optimization of the biochemical system (e.g. primer design) is required and the protocol becomes more specific to the application.
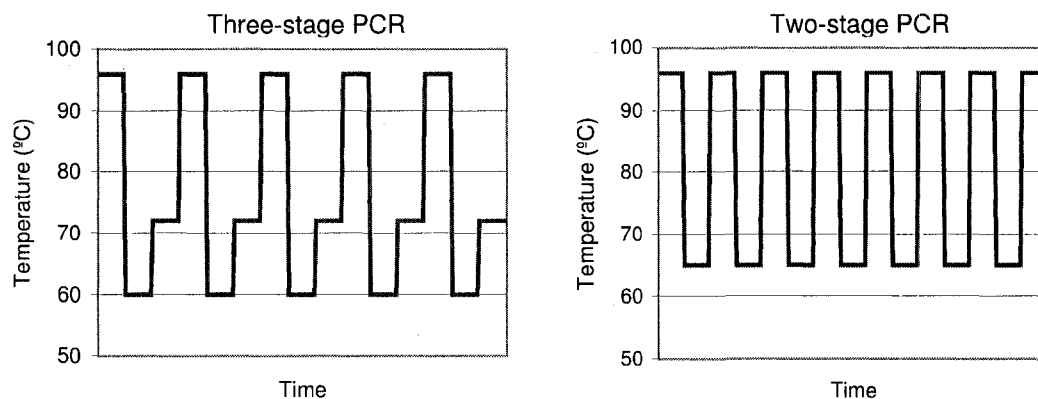
Figure 4-6. Three-stage (left) and two-stage (right) PCR approaches. In the two-stage approach, the annealing and extension stages are combined into one.

4.4.2 Optimized PCR dwell times

The duration of the PCR temperature stages may also be substantially shortened to further reduce the thermal cycling time while not compromising on the outcome of the PCR. Wittwer and Garling [4] have shown that PCRs can be performed using 1 s long denaturation and annealing stages. For the denaturation stage, they found that the separation of DNA duplexes can occur within a few seconds and is faster for shorter templates. For the annealing stage, kinetic studies on DNA renaturation predict that the use of excess primer concentrations ensures the annealing of typical PCR primers (15-25 bps) also occurs within a few seconds. Hence, Wittwer and Garling conclude that the extension stage requires the most time [4] since it is limited by the incorporation rate of the Taq ($\sim$30 nucleotides/s at 60°C [37]). Nevertheless, with a sufficiently short template (roughly <300bp), the extension stage too can be shortened to seconds because the Taq is able to complete copying the short template within this time. Shortening the extension time may not be suitable for longer templates, but in the context of medical diagnostic applications, the amplification of such long templates may not be necessary.

4.5 RESULTS

4.5.1 Experimental results of heat-sink implementation

PCR microchips were operated with a heat sink implemented (geometry design as described in sections 4.3.2 and 4.3.5 to maintain heating rates and temperature uniformity) to evaluate the effect of the heat sink on the thermal cycling of the microchip. After $\sim$5 minutes of operation, the heat sink temperature settled at 30°C, which was maintained for the remainder of the thermal cycling. The heat sink temperature could be made closer to room temperature if it was made larger or cooling fins were used (for increasing convection), but the present heat sink was effective and appropriate for portable systems (as in [24]). From simulations, the increase in the heat sink temperature can result in an increase of $\sim$2-3°C in the chamber temperature if it is not accounted for when determining the T_c vs. T_h

relationship. Hence, to ensure accuracy of the temperature control, calibration and operation of the PCR microchip was done only after allowing the heat sink temperature to stabilize by running a few temperature cycles on an unfilled microchip (repeatably settles at 30°C as described in section 4.2.4 for PCR runs done at ambient temperature). This "warm-up" run ensures the heat sink is close (~1-2°C away) to its equilibrium temperature when the actual PCR run is performed. Such a "warm-up" run would be unnecessary with a better heat sink that can maintain room temperature.

T_c was verified using experimental measurements of the temperature at the top of the microchip (T_s) as described in chapter 2 (ensured measured T_s values matched with those predicted by the FE model when T_c is at the desired values as described in section 4.2.3) and using thermochromic liquid crystals. We found that the steady-state temperatures in the reaction chamber could be maintained to within 1°C of the desired value. Furthermore, due to the rapid equilibration times provided by the heat sink (shorter RC time constant), though the same type of temperature controller as in chapter 2 was used (to maximize temperature ramping rates during the heating and cooling stages), the overshoots and undershoots in the reaction chamber temperature were much smaller than when a heat sink is not used (under 1°C rather than ~3°C, these were determined through measurements of T_s during thermal cycling since as determined in chapter 2, overshoots/undershoots in T_c are at most 1°C larger than those in T_s). With the heat sink implemented (optimal spacing as described in section 4.3.2 and 2 mm slot as in 4.3.5) and a typical room temperature of 22°C, heating and cooling rates in the microchip were ~5°C/s. A typical PCR cooling stage (from 94°C to 60°C) was shortened by ~80% (~35 s) compared to the case with no heat sink demonstrated in chapter 2. Typical heating stages (60°C to 72°C and 72°C to 94°C) were lengthened by ~30% (~1 s). As predicted by the simulations, an applied current of ~150 mA (~2 W) was required to maintain the temperature at the highest PCR stage (94°C). This is higher than the case with no heat sink (required only ~100 mA or ~1 W), but still amenable to portable and inexpensive platforms (as in chapter 2 and in [24], which can supply a maximum of 20 V and 200 mA). The power consumption is expected to be reduced with further miniaturization of the microchip, with simulations predicting a linear scaling.

4.5.2 Microchip implementation of fast PCR

With the heat sink implementation and the shortened, 2-stage PCR approach, the thermal cycling time required to perform PCR was roughly a third of the time required for the demonstration in chapter 2 (no heat sink and no PCR protocol optimization), taking ~30 min. to perform 35 PCR temperature cycles (for amplifying the β2-microglobulin gene). RT-PCR was performed on the β2-microglobulin gene in ~40 min. (10 min. RT stage) using the speed-optimized PCR approach and yielded comparable results to those obtained using the non-optimized approach in chapter 2 (Figure 4-7).
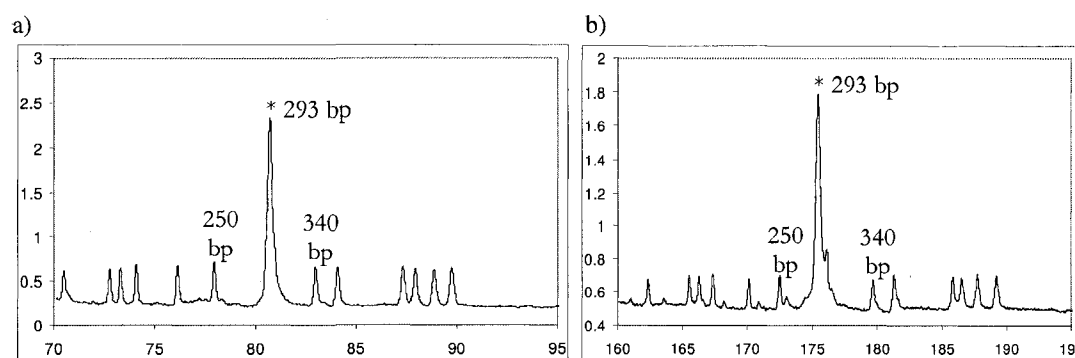
Figure 4-7. Electropherograms (fluorescence vs. time) comparing PCR products from on-chip thermal cycling a) with and b) without heat sink. The size of the PCR products are the same and the intensities are comparable. The product peak (293 bp) falls on the 300 bp peak of the size standard. Due to small variations in CE resolution between different microchips, this 300 bp is slightly resolved in b) but obscured in a).

4.6 CONCLUDING REMARKS

Shortening the time to complete a genetic amplification reaction is important for the widespread applicability of microfluidic implementations in point-of-care diagnostics. Despite the relatively low thermal conductivity of glass as compared to say silicon, glass-based implementations will certainly be widely used on account of their suitability to other molecular biology techniques (e.g. CE). As a result, we present strategies to overcome the low thermal conductivity of glass-based microchips and thus achieve rapid PCRs in such devices.

By implementing a heat sink and carefully designing its position, the passive cooling rate of the microchip was greatly improved with minimal sacrifices in terms of heating rate and power consumption. The low thermal conductivity of glass became an advantage in this case, readily providing the thermal isolation necessary between the heat sink and the vicinity of the resistive element and reaction chamber. Additionally, the implementation of the heat sink served to improve the accuracy of the temperature control by assisting in the reduction of overshoots/undershoots, and also to allow thermal modules to be placed more closely to each other while remaining independent. The thermal cycling time was further reduced by developing a two-stage PCR protocol with shortened dwell times, which is particularly suitable for short DNA templates (<300 bp). With both the heat sink and the speed-optimized PCR protocol, RT-PCR of the β2-microglobulin gene was performed roughly three times faster than the earlier demonstration with no heat sink or shortened protocol, but still yielding comparable results.

Both instrumental and protocol optimization strategies may be applied to microchip materials and/or geometries different from those presented here. In particular, if the reaction volume is further miniaturized (likely with an integrated sample concentration step for dealing with clinical samples) to improve thermal transition speed and power consumption, the same strategies used here could be employed to further reduce the thermal cycling time, making even shorter PCRs possible (eventually limited primarily by the incorporation rate of the polymerase).

Further miniaturization would also allow more thermal modules to be placed within a given microchip area, resulting in microchips that can perform more complex protocols, or more processes in parallel. In this case, low thermal conductivities are highly advantageous as they readily allow thermal modules to be placed in high densities while remaining thermally independent. Though high thermal conductivities can inherently provide faster temperature ramping rates, they do not provide the thermal isolation required for high device densities. The thermal module developed here, which uses low thermal conductivities and is readily scalable for improved thermal transition speeds, is therefore a highly useful building block for more complex lab-on-a-chip systems with many integrated functionalities.

4.7 REFERENCES

[1]   Lagally, E.T. and R.A. Mathies, "Integrated genetic analysis microsystems", *Journal of Applied Physics D: Applied Physics*, 2004. **37**: p. R245-R261.

[2]   Kricka, L.J. and P. Wilding, "Microchip PCR", *Analytical and Bioanalytical Chemistry*, 2003. **377**: p. 820-825.

[3]   Sadler, D.J., R. Changrani, P. Roberts, C.-F. Chou, and F. Zenhausern, "Thermal management in bioMEMS: temperature control for ceramic-based PCR and DNA detection devices", *IEEE Transactions on Components and Packaging Technology*, 2003. **26**(2): p. 309-316.

[4]   Wittwer, C.T. and D.J. Garling, "Rapid cycle DNA amplification: time and temperature optimization", *Biotechniques*, 1991. **10**(1): p. 76-83.

[5]   Poser, S., T. Schulz, U. Dillner, V. Baier, J.M. Kohler, D. Schimkat, G. Mayer, and A. Siebert, "Chip elements for fast thermocycling", *Sensors and Actuators A*, 1997. **62**: p. 672-675.

[6]   Lee, C.-Y., G.-B. Lee, H.-H. Liu, and F.-C. Huang, "MEMS-based temperature control systems for DNA amplification", *International Journal of Nonlinear Sciences and Numerical Simulation*, 2002. **3**: p. 215-218.

[7]   Yoon, D.S., Y.-S. Lee, Y. Lee, H.J. Cho, S.W. Sung, W. Oh, J. Cha, and G. Lim, "Precise temperature control and rapid thermal cycling in a micromachined DNA polymerase chain reaction chip", *Journal of Micromechanics and Microengineering*, 2002. **12**: p. 813-823.

[8]   Zhao, Z., Z. Cui, D. Cui, and S. Xia, "Monolithically integrated PCR biochip for DNA amplification", *Sensors and Actuators A*, 2003. **108**: p. 162-167.

[9]   Zou, Q., U. Sridhar, Y. Chen, and J. Singh, "Miniaturized independently controllable multichamber thermal cycler", *IEEE Sensors Journal*, 2003. **3**(6): p. 774-780.

[10]   Lee, D.-S., S.H. Park, H. Yang, K.-H. Chung, T.H. Yoon, S.-J. Kim, K. Kim, and Y.T. Kim, "Bulk-micromachined submicroliter-volume PCR chip with very rapid thermal response and low power consumption", *Lab on a Chip*, 2004. **4**: p. 401-407.

[11]   Noh, J., S.W. Sung, M.K. Jeon, S.H. Kim, L.P. Lee, and S.I. Woo, "In situ thermal diagnostics of the micro-PCR system using liquid crystals", *Sensors and Actuators A*, 2005. **122**: p. 196-202.

[12]   Yang, M., P. R., and M.A. Burns, "Cost-effective thermal isolation techniques for use on microfabricated DNA amplification and analysis devices", *Journal of Micromechanics and Microengineering*, 2005. **15**: p. 221-230.

[13]   Neuzil, P., C. Zhang, P. Juergen, S. Oh, and L. Zhuo, "Ultra fast miniaturized real-time PCR: 40 cycles in less than six minutes", *Nucleic Acids Research*, 2006. **34**(11): p. e77.

[14]   Easley, C.J., J.A.C. Humphrey, and J.P. Landers, "Thermal isolation of microchip reaction chambers for rapid non-contact DNA amplification", *Journal of Micromechanics and Microengineering*, 2007. **17**: p. 1758-1766.

[15]   Lagally, E.T., C.A. Emrich, and R.A. Mathies, "Fully integrated PCR-capillary electrophoresis microsystem for DNA analysis", *Lab on a Chip*, 2001. **1**(2): p. 102-107.

[16]   Lagally, E.T., J.R. Scherer, R.G. Blazej, N.M. Toriello, B.A. Diep, M. Ramchandani, G.F. Sensabaugh, L.W. Riley, and R.A. Mathies, "Integrated portable genetic analysis microsystem for pathogen/infectious disease detection", *Analytical Chemistry*, 2004. **76**(11): p. 3162-3170.

[17]   Pal, R., M. Yang, R. Lin, B.N. Johnson, N. Srivastava, S.Z. Razzacki, K.J. Chomistek, D.C. Heldsinger, R.M. Haque, V.M. Ugaz, P.K. Thwar, Z. Chen, K. Alfrano, M.B. Yim, M. Krishnana, A.O. Fuller, R.G. Larson, D.T. Burke, and M.A. Burns, "An integrated microfluidic device for influenza and other genetic analyses", *Lab on a Chip*, 2005. **5**: p. 1024-1032.

[18]   Oh, K.W., C. Park, K. Namkoong, J. Kim, K.-S. Ock, S. Kim, Y.-A. Kim, Y.-K. Cho, and C. Ko, "World-to-chip microfluidic interface with built-in valves for multichamber PCR assays", *Lab on a Chip*, 2005. **5**: p. 845-850.

[19]   Liao, C., G. Lee, H. Liu, T. Hsieh, and C. Luo, "Miniature RT–PCR system for diagnosis of RNA-based viruses", *Nucleic Acids Research*, 2005. **33**(18): p. e156:3-7.

[20]   Huang, F.C., C.S. Liao, and G.B. Lee, "An integrated microfluidic chip for DNA/RNA amplification, electrophoresis separation and on-line optical detection", *Electrophoresis*, 2006. **27**: p. 3297-3305.

[21] Toriello, N.M., C.N. Liu, and R.A. Mathies, "Multichannel reverse transcription-polymerase chain reaction microdevice for rapid gene expression and biomarker analysis", *Analytical Chemistry*, 2006. **78**: p. 7997-8003.

[22] Easley, C.J., J.M. Karlinsey, J.M. Bienvenue, L.A. Legendre, M.G. Roper, S.H. Feldman, M.A. Hughes, E.L. Hewlett, T.J. Merkel, J.P. Ferrance, and J.P. Landers, "A fully integrated microfluidic genetic analysis system with sample-in-answer-out capability", *Proceedings of the National Academy of Sciences*, 2006. **103**(51): p. 19272-19277.

[23] Liu, P., T.S. Seo, N. Beyor, K.-J. Shin, J.R. Scherer, and R.A. Mathies, "Integrated portable polymerase chain reaction-capillary electrophoresis microsystem for rapid forensic short tandem repeat typing", *Analytical Chemistry*, 2007. **79**: p. 1881-1889.

[24] Kaigala, G.V., V.N. Hoang, A. Stickel, J. Lauzon, D.P. Manage, L.M. Pilarski, and C.J. Backhouse, "Fully portable and inexpensive microchip-based genetic analysis platform for integrated RT-PCR and capillary electrophoresis", *The Analyst*, Accepted December 2007.

[25] Oda, R.P., M.A. Strausbauch, A.F.R. Huhmer, N. Borson, S.R. Jurrens, J. Craighead, P.J. Wettstein, B. Eckloff, B. Kline, and L.J. P., "Infrared-mediated thermocycling for ultrafast polymerase chain reaction amplification of DNA", *Analytical Chemistry*, 1998. **70**: p. 4361-4368.

[26] Giordano, B.C., J. Ferrance, S. Swedberg, A.F.R. Huhmer, and J.P. Landers, "Polymerase chain reaction in polymeric microchips: DNA amplification in less than 240 seconds", *Analytical Biochemistry*, 2001. **291**: p. 124-132.

[27] Kaigala, G.V., R.J. Huskins, J. Preiksaitis, X.L. Pang, L.M. Pilarski, and C.J. Backhouse, "Automated screening using microfluidic chip-based PCR and product detection to assess risk of BK virus-associated nephropathy in renal transplant recipients", *Electrophoresis*, 2006. **27**(19): p. 3753-3763.

[28] Van Dijken, J., G. Kaigala, J. Lauzon, A. Atrazhev, B.J. Taylor, T. Reiman, A.R. Belch, C.J. Backhouse, and L.M. Pilarski, "Microfluidic chips for detecting the t(4;14) translocation and monitoring disease during treatment using RT-PCR analysis of IgH-MMSET hybrid transcripts", *Journal of Molecular Diagnostics*, 2007. **9**(3): p. 358-367.

[29] Grover, W.H., A.M. Skelley, C.N. Liu, E.T. Lagally, and R.A. Mathies, "Monolithic membrane valves and diaphragm pumps for practical large-scale integration into glass microfluidic devices", *Sensors and Actuators B-Chemical*, 2003. **89**(3): p. 315-323.

[30] Fontes, J., "Temperature Sensors", in *Sensor Technology Handbook*, J.S. Wilson, Editor. 2005, Elsevier Inc.: Oxford. p. 531-562.

[31] Lide, D.R., ed. *CRC Handbook of Chemistry and Physics 86th edition*. 2008, CRC Press: Boca Raton.

[32] Erickson, D., D. Sinton, and D. Li, "Joule heating and heat transfer in polydimethylsiloxane microfluidic systems", *Lab on a Chip*, 2003. **3**(3): p. 141-149.

[33] Vahedi, G., C. Kaler, and C.J. Backhouse, "An integrated method for mutation detection using on-chip sample preparation, single-stranded conformation polymorphism, and heteroduplex analysis", *Electrophoresis*, 2004. **25**(14): p. 2346-2356.

[34] Senturia, S.D., *Microsystem Design*. New York: Springer Science+Business Media, Inc., 2001.

[35] Lienhard IV, J.H. and J.H. Lienhard V, *A Heat Transfer Textbook*. 3rd ed. Cambridge: Phlogiston Press, 2005.

[36] Sullivan, D., B. Fahey, and D. Titus, "Fast PCR: General considerations for minimizing run times and maximizing throughput", *Bioradiations*, 2006(118): p. 16-21.

[37] Innis, M.A., K.B. Myambo, D.H. Gelfand, and M.A.D. Brow, "DNA sequencing with Thermus aquaticus DNA polymerase and direct sequencing of polymerase chain reaction-amplified DNA", *Proceedings of the National Academy of Sciences*, 1988. **85**(24): p. 9436-9440.

Chapter 5

Other related research and future directions

5.1 INTRODUCTION

The development of a reliable on-chip thermal management technique opens up several possibilities for lab-on-a-chip systems involving PCR and for protocols beyond molecular biology. This chapter will provide an overview of the research currently underway to explore different aspects and applications of the PCR microchip and of the single resistive element strategy for thermal management described in the earlier chapters.

5.2 TIME DOMAIN TEMPERATURE SENSING STRATEGY

As described in chapter 2, we had found that as the PCR microchip cools passively, the temperature of the resistive element (T_h) falls quickly at first until it matches the temperature of its vicinity, including the reaction chamber (T_c). T_h and T_c then match each other closely as they cool together (Figure 5-1a). It was envisaged that this phenomenon may be used as an alternate temperature sensing strategy which is possibly more direct and thus more robust than the strategy of relating T_c to T_h, which allows the temperature to be well known only once steady-state is reached. The power delivered to the resistive element would alternate between a high power heating pulse that delivers heat to the reaction chamber and a low

power sensing pulse that allows T_h to equilibrate with T_c in order to measure it (only enough current to allow resistance to be measured without causing significant resistive heating). Dubbed time domain multiplexing (TDM), this strategy was not possible when the microchip was operated without a heat sink since T_c cooled significantly (by more than 1°C) by the time T_h matched it. However, with the heat sink implemented, simulations showed that T_h could reach T_c much more quickly (in less than 0.5 s) and before T_c has a chance to change, making the TDM temperature sensing strategy possible (Figure 5-1b). Nonetheless, the presence of the heat sink causes the T_h to settle at a temperature lower than T_c, resulting in the fact that T_h will be exactly equal to T_c only at a certain point in time t_{eq}. This time (t_{eq}) likely varies depending on the starting T_h before the sensing pulse as well as on the experimental environment of the microchip, making it difficult to pinpoint what t_{eq} should be in order to implement the TDM strategy to accurately measure T_c. The TDM strategy is therefore not an improvement over the currently used strategy (applying the determined T_c vs. T_h relationship) unless T_h can be made to equilibrate with T_c without cooling below it.
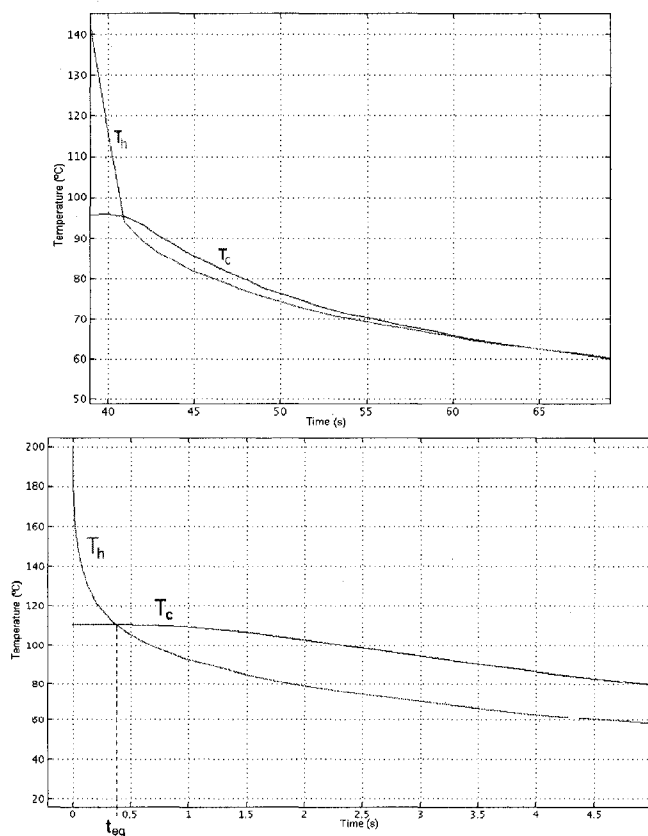
Figure 5-1. Simulation of passive cooling in a microchip a) without and b) with a heat sink implemented

81

5.3 SURFACE EFFECTS

Although temperature has been well characterized for the PCR microchips developed in this thesis, little work has been done to explore the surface effects in the microchip and how they impact PCR. Currently, to counteract surface adsorption of the PCR mix components (particularly the DNA and the Taq polymerase), the fluidic layer is silanized with Sigmacote (Sigma-Aldrich, St. Louis, MO, USA) prior to the assembly of the microchip, and bovine serum albumin (BSA) is included in the PCR mix to passivate the surface. However, experiments have yet to be done to quantify the effectiveness of these treatments. The effectiveness of other treatments, such as the Hjerten protocol [1] and dynamic coating [2], also needs to be considered and tested.

PCR experiments completed so far suggest significant surface adsorption effects are still present with the currently used protocol. For example, though the inclusion of BSA tends to reduce the PCR product yield of a control run performed on a conventional thermal cycler (in a polypropylene tube), it greatly improves the yield of a PCR performed on-chip, which may fail altogether if BSA is excluded. Furthermore, it has been found that in some cases where an on-chip PCR did not result in a PCR product (or yielded a very weak product), flushing the chip with water, allowing it to dry, and redoing the PCR on the chip would result in a strong PCR product, suggesting the microchip walls had been "coated" by the previous run. Alternatively, if a chip is reused after yielding a strong PCR product, the second PCR will yield non-specific products, suggesting that reagents or products left behind from the previous run are interfering. Different surface treatments may reduce surface adsorption further and thus improve PCR yield.

The effect of fabrication techniques on the microchip surfaces must also be considered. For example, it is known that residual chrome from etching masks can inhibit PCR [3], and thus, extra precautions must be taken when stripping the chrome off the fluidic layer to ensure no residue remains. The Dynasolve used to disassemble PCR chips for reuse also inhibits PCR with trace amounts and may also detrimentally affect the glass surface. As described in

earlier chapters, prior to rebonding PCR chips disassembled by Dynasolve, the fluidic layer must undergo a cold Piranha treatment as well as a high temperature anneal to rejuvenate the glass surface. PCR was successful on reused chips as long as both these treatments were perfomed, but failed if either was neglected.

5.4 INTEGRATION WITH OTHER MOLECULAR BIOLOGY TECHNIQUES

5.4.1 Capillary electrophoresis

Though PCR is a critically important molecular biology technique, PCR alone is most often not sufficient to carry out a genetic analysis. Other techniques are required as well (e.g. for detection), and PCR is typically one step out of a series of steps used to process and analyze genetic material. One such technique is capillary electrophoresis (CE), which is typically performed immediately following PCR to detect and analyze the amplified DNA fragments. High electric fields are applied to introduce the migration of negatively charged DNA fragments through a microfluidic channel filled with a sieving matrix. The sieving matrix provides resistance to the movement of the DNA fragments, allowing smaller fragments to migrate more quickly than large ones. By running the PCR product along with a size standard (a mixture of DNA fragments of known size that acts as a ruler), the size and identity of the PCR product can be confirmed. Certain mutations can also conformationally change DNA and hence its electrophoretic mobility. These mutations can be detected using techniques such as heteroduplex analysis (HA) and single-stranded conformational polymorphism (SSCP) [4], which both make use of CE to differentiate conformational changes in DNA for useful medical diagnostic applications.
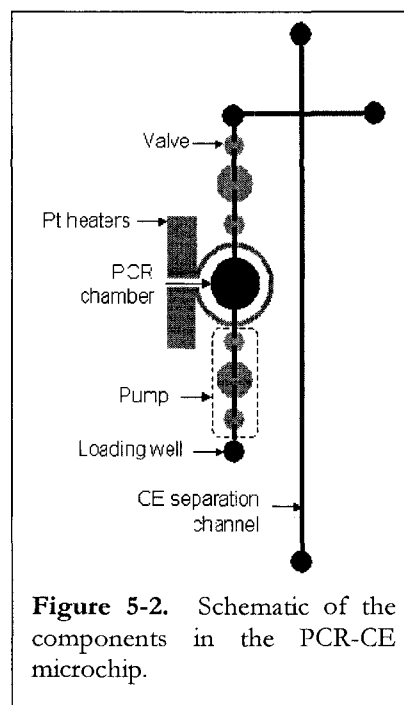
Figure 5-2. Schematic of the components in the PCR-CE microchip.

Much work has been completed in integrating CE with the PCR (including RT-PCR) system presented in this thesis. The glass/PDMS/glass microchip was enlarged to accommodate wells and microfluidic channels for performing CE (Figure 5-2). The design guidelines and temperature characterizing methods described in chapter 2 were readily applied with ease to the PCR-CE microchip, and RT-PCR has been repeatedly demonstrated using the microchip, with subsequent CE analysis performed both on standard glass CE chips and on the PCR-CE microchip itself.

A portable, shoebox-sized, and inexpensive (parts ~$1000) platform, dubbed the TTK (Tricorder Tool Kit), has also been developed (by Alex Stickel at AML) for operating the PCR-CE microchips (Figure 5-3). The TTK consists of high voltage circuitry for performing CE, a laser for exciting fluorescently-labelled analytes, a CCD camera for detecting the analytes, the source measurement unit circuitry for operating the resistive element, and mini-pumps for actuating the valves and pumps. RT-PCR and CE have been performed on the PCR-CE microchip using the TTK (Figure 5-3) [5], and work is currently underway (by Jana Lauzon at ACDC) to develop a protocol where RT-PCR-CE is performed in a completely seamless manner (without the need for user intervention between any steps of the process). Protocols for CE-based tests, such as HA, SSCP, and RFLP (restriction fragment length polymorphism), are under development as well. Along with the PCR-CE microchip, this TTK platform is a substantial step towards realizing a portable and inexpensive diagnostic tool sufficiently practical for widespread use in a clinical setting.
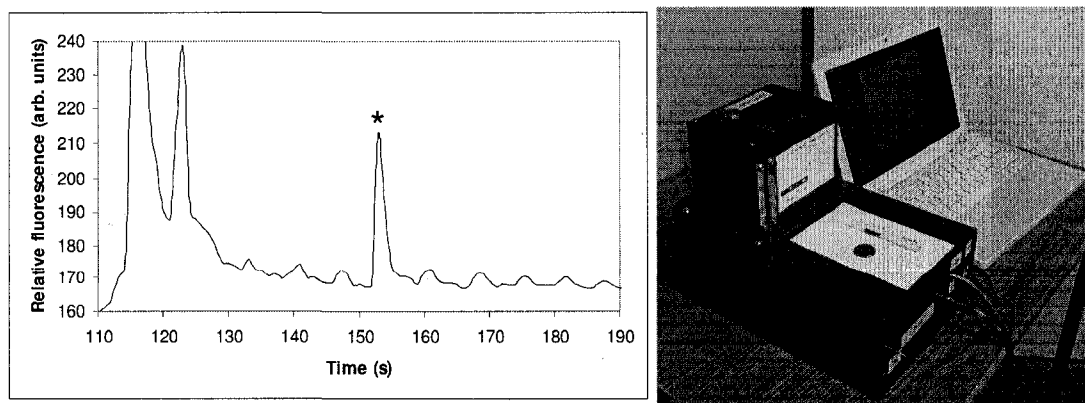
Figure 5-3. An electropherogram (top) obtained from an RT-PCR-CE (β2M gene) performed on the same PCR-CE chip using the TTK (bottom).

5.4.2 Sample preparation using magnetic beads

Molecular biology techniques both preceding and following PCR are required to carry out a genetic test. Genetic material (DNA or RNA) from clinical samples (e.g. blood, buccal swabs, genital swabs, etc.) most often must be extracted and purified before undergoing PCR since other components in these raw samples (e.g. seral proteins) may inhibit or interfere with the biochemical reaction. One possible method for performing this sample preparation step on a microfluidic chip is through the use of magnetic beads. As an example, Chargeswitch® beads (Invitrogen, Carlsbad, CA, USA) possess a surface that switches electrical charge depending on pH. At a low pH (< 5.5), they become positively charged and can thus bind to negatively charged genetic material. At a high pH (> 8.5), they become negatively charged and can hence release the genetic material. Magnetic fields can be used to move the beads through buffers with low or high pH to bind or release genetic material where required. The magnetic beads can therefore be used to extract DNA from clinical samples, and also to concentrate DNA prior to PCR, which may be required for obtaining sufficient starting template material when working with very small reaction volumes (e.g. if the PCR chamber is miniaturized further). A protocol for DNA extraction and purification using magnetic beads on a microfluidic chip has been developed (by Govind Kaigala and Jeeshan Chowdhury at AML and ACDC) and is currently being adapted for integration with the PCR-CE microchip. Such an integration will result in a system capable of performing genetic tests directly on, for example, a drop of blood.

5.5 OTHER APPLICATIONS

5.5.1 Clinically relevant PCR-based tests

Chapters 2 and 4 describe the use of the developed single resistive element heating system for performing RT-PCR of the β2 microglobulin gene. This gene is present in human cells and is typically used as an experimental control (e.g. verifying the integrity of the reagents and template used). The microchip has successfully been used to repeatedly amplify more

clinically relevant templates as well (Figure 5-4). On-chip RT-PCR has been performed on patient mRNA samples to amplify the CDR2/CDR3 gene, a biomarker for multiple myeloma. Both BK virus DNA and Norovirus RNA have also been amplified (PCR and RT-PCR respectively). Work is currently underway (by Dammika Manage at AML and ACDC) to perform on-chip PCR-HA-RFLP analyses of hemochromatosis (HFE) and breast cancer (BRCA) genes. These applications demonstrate the ability and versatility of the developed microchip (and TTK platform) for cancer diagnostics and/or viral detection.
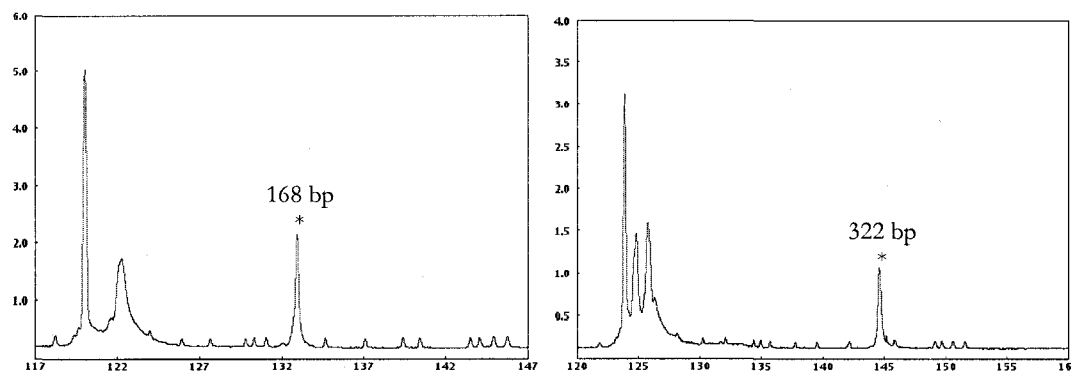
Figure 5-4. Electropherograms (relative fluorescence in arbitrary units vs. time in seconds) of CDR2/CDR3 (left) and Norovirus (right) templates amplified on-chip from RNA samples (RT-PCR). CE was performed on a μTK.

5.5.2 Real-time PCR

PCR can also be performed with real-time detection to quantify the amount of template DNA present in a given sample. As thermal cycling proceeds, the emitted fluorescence from labeled, amplified DNA is monitored at the end of each cycle. By comparing the resulting fluorescence vs. cycle curve to similar curves obtained from standard reactions with known starting DNA concentrations, the concentration in the given sample can be determined. To date, a TTK platform has been modified (by Alex Stickel at AML) such that the CCD camera detects fluorescence in the PCR reaction chamber rather than the CE channel of the PCR-CE microchip. Real-time PCR has been successfully performed using a PCR-CE microchip on this modified TTK platform, yielding a fluorescence vs. time curve (Figure 5-5). However, conventionally, standard reactions used for quantifying DNA must be performed simultaneously with the unknown sample to ensure experimental conditions are similar enough to allow fair comparison. Currently, this is not possible on the developed

PCR-CE chip as it does not include more than one reaction chamber. Nevertheless, the current reaction chamber and resistive element design can readily be arrayed with the proper thermal management strategies and design considerations in place (e.g. heat sink and adequate spacing between thermally active components).
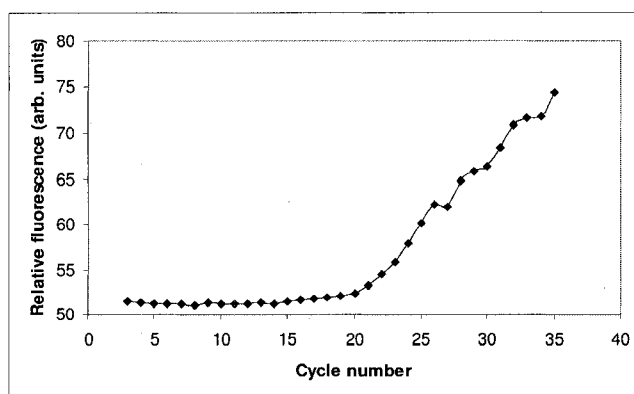
Figure 5-5. Fluorescence vs. time curve for an on-chip real-time PCR run of the β2M gene.

5.5.3 Other molecular biology techniques

PCR is by no means the only molecular biology technique that requires heating. Many other techniques make use of heating as well, but the precise thermal cycling required to perform PCR makes it the most complex. Other techniques typically only require maintaining one or two temperature stages, usually to promote enzyme activity. For example, the reverse transcription (RT) step described in chapters 2 and 4 simply involves keeping the reaction chamber at 45°C (this step builds cDNA from RNA to allow PCR to be subsequently performed). Another example is nucleic acid sequence-based amplification (NASBA), another molecular biology technique for amplifying RNA that employs three enzymes acting at a single temperature of 41°C. Though not yet done here, NASBA can readily be performed by the developed microchip as well.

Fluorescence in situ hybridization (FISH) is another molecular biology technique requiring heating (adapted to a microfluidic chip in [6]), and has been successfully performed on-chip using the single resistive element strategy. FISH is a commonly used technique for labeling and analyzing the chromosomes in whole cells. It can detect gross chromosomal

abnormalities and is used to diagnose diseases such as trisomy 21 (Down's syndrome). Using the same microchip and heat sink as described in chapter 4, cells were immobilized with a 10 minute 85°C treatment and then fluorescently tagged probes were hybridized with a 15 hour 37°C treatment (Figure 5-6). Since the thermal module had been well characterized, it was readily adapted for FISH within a day (primarily just a change in software), was successful on the first attempt, and worked reliably afterwards. Work is currently underway (by Vince Sieben at AML and ACDC) to automate FISH on a microchip utilizing the single resistive element heating approach, a step towards making FISH a practical and affordable technique for more routine and widespread use in a clinical setting.

Figure 5-6. FISH performed on Daudi cells using on-chip heating. The red probes are attached to the p53 gene, a tumour suppressor gene that serves to eliminate cancer-prone cells before they proliferate (more than 50% of human tumours contain a mutation or deletion of the p53 gene). The green probes mark the center of the chromosome on which the p53 should be found, and the blue demarcates the nucleus of the cell.

5.5.4 Thermoelectrically actuated microvalves

The single resistive element heating system developed in this thesis is widely applicable and not limited to molecular biology technique implementations. For example, the glass/PDMS/glass microvalve structure used in the PCR microchips presented in this thesis can readily be actuated by thermoelectric means instead of pneumatic means [7]. Rather than applying pressured air/vacuum to the control layer, it is filled instead with a low melting point polymer, such as paraffin or polyethylene glycol (PEG), which undergoes a significant volumetric expansion upon melting. The volumetric changes of the polymer as it undergoes phase transitions (between solid and liquid phases) are used to actuate the PDMS membrane (phase change microvalve). The thermal module developed in this thesis can readily be and has been applied to a polymer reservoir to form an electrically addressable microvalve.

With the proper thermal management strategies and design considerations in place to prevent thermal cross-talk, these microvalves have been integrated on a microchip with each other as well as with other thermally active components such as a thermal cycler for PCR. Preliminary results have shown that these polymer-based microvalves perform well enough to be suitable for PCR (can overcome the generated vapor pressures and confine the contents of the reaction chamber as it is thermally cycled for ~2 hours). Compared to the pneumatically acutated valves, the thermoelectrically actuated valves are one step ahead in terms of integration since their operation requires less components external to the microchip. Whereas the thermoelectrically actuated valves require only a power supply and electrical connections, the pneumatically actuated valves require sources of air pressure and vacuum (either external lines or from mini-pumps as in the TTK platform), tubing for directing the pressure/vacuum, external valves for switching between pressure or vacuum, and the electronics for controlling these external valves. As a result, the implementation of the thermoelectrically actuated valves is simpler, less expensive, and more amenable to further miniaturization.

However, since the operation of the thermoelectrically actuated valves relies on the propagation of heat, their response time tends to be slower compared to the pneumatically actuated valves, being on the order of a minute rather than less than a second. Shrinking the microvalve would solve this issue as described in 5.6.1. Furthermore, experiments with PEG have also revealed that the polymer is susceptible to thermal degradation over time. This degradation is believed to be due to oxidative effects and results in a breakdown of the PEG polymer chains into lower molecular weight chains, lowering the overall melting temperature of the polymer such that it becomes increasingly difficult to solidify using passive cooling means. As a result, the operation time of the thermoelectrically actuated valves is very limited (~2-3 hours) and is further shortened if it is operated at higher temperatures. Work is currently being done to explore engineering the actuating polymer to avoid this degradation effect, which would result in more useful microvalves. The use of other polymers, such as paraffin, is also being investigated (by Govind Kaigala and Sohayl Bhatti at AML). Preliminary experiments with paraffin have shown that its phase transitions occur faster than for PEG and that it does not appear to degrade with usage.

5.5.5 Laser induced breakdown spectroscopy

A major focus in this thesis has been temperature uniformity, but there are applications where temperature non-uniformities are desired as well. Chapter 2 described design guidelines for maintaining temperature uniformity on a resistive heating element in order to allow it to act as a temperature sensor. However, hot spots can also be deliberately generated by design. An application for such a heater is laser induced breakdown spectroscopy (LIBS), for which a microchip-based demonstration is being developed in conjunction with Yogesh Godwal, Siu-lung Lui, and Dr. Robert Fedosejevs at the University of Alberta (ECE Department). For this technique, a heater ring with notches can be used to heat a confined, unknown liquid sample. The notches in the heater ring become hot spots that reach very high temperatures (Figure 5-7), producing pressure that forces droplets of the sample to escape through a small opening (same principle as an ink jet printer). A laser impinging on the droplet then ablates a small amount of material, generating a plasma plume whose emission spectrum can be analyzed to identify the atomic components of the sample. Temperature non-uniformities in the resistive element are necessary to rapidly reach the very high temperatures required while using relatively low power.
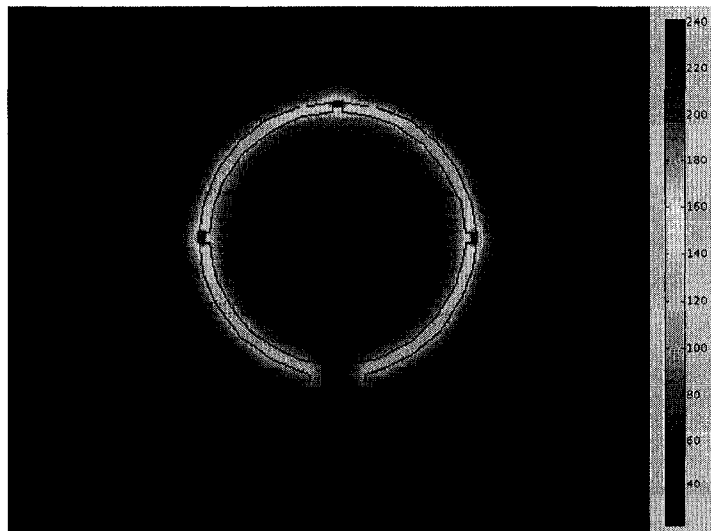
Figure 5-7. Simulation of the temperature distribution on a Pt/Ti heater ring with notches that are twice as narrow as the width of the ring. Temperatures at the notches are ~100°C higher than the temperature of the remainder of the heater ring.

5.6 Manufacturability aspects

5.6.1 Further miniaturization

Along with the functionality aspect of integration, the size aspect has been considered as well. Further miniaturization of the developed localized microfluidic heating system would allow more thermal modules (e.g. reaction chambers or microvalves) to be integrated into a given area, rendering more complex experimental protocols possible and/or allowing more experiments to be done in parallel to improve throughput (e.g. arrayed PCR). Also, reducing the overall size of the microchip would also increase the amount of microchips that can fit on a single substrate, greatly improving fabrication throughput and hence substantially reducing the individual cost of each microchip.

Miniaturization of the microfluidic heating system also leads to reduced power consumption and faster temperature transitions since a smaller volume is being heated. As described in chapter 4, we expect thermal resistance to scale proportionally with the ratio of length over cross-sectional area. Therefore, the thermal resistance should scale inversely with the size of the thermal management system. For example, halving all the dimensions in the system should double the thermal resistances involved. Applying an analogous form of Ohm's Law (potential differences are analogous to temperature differences and electrical currents are analogous to heat flow, i.e. $\Delta V = IR \Rightarrow \Delta T = \dot{Q}R$), we therefore expect that the heat (power) required to maintain a given temperature inside the reaction chamber will scale linearly with size of the system. For example, halving all dimensions of the system will halve its power consumption. As for the equilibration time of the thermal management system, the thermal capacitance of the system scales proportionally with the heated volume. Combining this with the dependence of the thermal resistance on length over surface area, we expect that the (RC) time constant and hence equilibration time of the thermal system will scale quadratically with its dimensions (i.e. $\tau \propto (L/A)(AL) = L^2$). For example, if all dimensions of the thermal system were halved, the equilibration time will be reduced by a factor of 4. Both these trends for power consumption and for the equilibration time were also observed in simulations of scaling down the microchip (Table 5-1).

Yet, although the thermal resistances increase as the system dimensions are scaled, their ratios remain the same if all dimensions are scaled equally. As a result, the spatial temperature distributions in the system are preserved and essentially just scaled down (a simple change of variables from (x, y, z) to a(x, y, z) in the heat conduction equation shown in Appendix A yields the same observation, i.e. the scaling constant, a, factors out). This trend was also observed in FE simulations. The temperature in the microchip decreases gradually as we move away from the chamber and resistive element, crossing certain temperatures at certain distances. As shown in Table 5-1, these distances are halved if all dimensions of the thermal management system are halved. Thus, the spacing that must be maintained between different thermal modules to ensure thermal independence is reduced, and as a result, they can be spaced more closely together. Additionally, the temperature required at the resistive element to maintain a given temperature in the chamber remains the same. Therefore, the T_h vs. T_c relationship required to control the temperature of the chamber remains unchanged and does not need to be recharacterized if all dimensions of the system are scaled equally.

Table 5-1. Simulation results for scaling the entire thermal management system
The chamber temperature is at ~97°C for all three cases.

Scaling factor	Applied power to maintain ~97°C in the chamber	Equilibration time (time to reach within 0.5°C of final temperature)	Distance from center of chamber for T <50°C	Distance from center of chamber for T <30°C	Distance from center of chamber for T = 22°C
1	2.08 W	~24 s	>4 mm	>6 mm	>12 mm
0.5	1.01 W	~6 s	>2 mm	>3 mm	>6 mm
0.25	0.52 W	~1.5 s	>1 mm	>1.5 mm	>3 mm

However, smaller volumes than the currently used design will also become more difficult to handle manually using micropipettors. A more automated and/or robotic system may be required to handle very small volumes. Earlier experiments have also shown that shallower chambers are more prone to air bubble formation and trapping. Furthermore, reducing the size of the chamber will greatly increase its surface area to volume ratio. Therefore, surface effects (discussed in section 5.3) will become much more significant and will have to be dealt with in order to preserve the functionality of the microchip.

Nevertheless, if the thermal management system is scaled while maintaining the same chamber height (i.e. only scale the radius of the chamber), the surface area to volume ratio of the chamber should not greatly increase until its radius becomes comparable to its height. Figure 5-8 shows that this limit means that the radius of the currently used chamber geometry can be scaled down up to four times before the surface area to volume ratio is substantially increased. As long as the height of the chamber still remains relatively much smaller than the microchip layer thicknesses, the temperature distributions in the thermal system should not vary significantly. As a result, the operation of the thermal management module developed in this thesis should remain unchanged if its dimensions, except the chamber height, are scaled down no more than four times.
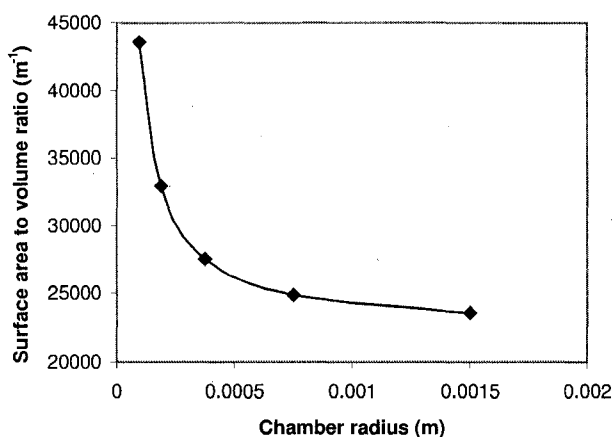
Figure 5-8. Surface area to volume ratio of a 90 μm deep reaction chamber as a function of its radius (original radius as presented in this thesis is 1.5 mm).

Using thinner microchip layers will also reduce thermal mass and hence improve temperature ramping rates and lower power consumption. However, the fact that thermal resistances (and hence thermal isolation) will change must be kept in mind (explored further in Appendix F). For example, thinning the bottom glass plate would change the thermal resistance between the vicinity on the reaction chamber and the heat sink, and hence, the optimal heat sink position would be altered. Thinning the top glass plate would reduce the thermal isolation between the reaction chamber and room temperature (discussed further in Appendix B). The temperature in the chamber would therefore become more susceptible to variations in room temperature, and the steady-state T_c vs. T_h relationship would be altered. Thinning the glass layers may also lead to the microchips being more prone to breakage, particularly during Dynasolve treatment (PDMS tends to swell and exert stress).

5.6.2 USB power operation

In order to move towards making genetic analysis systems more practical for widespread usage, finite element modeling was used to explore the possibility of adapting the current PCR chip design to USB power requirements (5 V and 500 mA as opposed to the present 20 V and 200 mA). With the current PCR chip architecture and without a heat sink implemented, the power required to maintain the reaction chamber at ~95°C is ~1 W, which is achievable with USB capabilities (2.5 W) while leaving a reasonable amount of power for accelerating heating rates (by applying maximum power). However, with the current resistive element design (~70 Ω at room temperature), voltages greater than 5 V are required to apply sufficient electrical current to maintain the temperatures required for PCR. To reduce this voltage requirement (and thus eliminate the need for DC-DC converters), the resistance of the element can be decreased. Given the same reaction chamber size and geometry, simulations have shown that increasing the width of the heater ring by four times (i.e. decreasing the resistance by four times) will allow PCR to be performed (i.e. can attain the required chamber temperatures) while remaining below USB power limitations (5 V and 500 mA). However, the sensitivity of the resistive element to temperature changes also becomes reduced by a factor of four when its resistance is reduced (the R vs. T slope is the product of the temperature coefficient of resistance and the resistance of the thin film element at room temperature). This relative reduction in sensitivity would have to be compensated by the temperature sensing electronic circuitry (e.g. the Wheatstone bridge, signal amplifiers, and RC filters for noise reduction) to ensure temperature can be measured with sufficient precision to allow for accurate control. With the source measurement unit circuitry currently in use, the sensitivity for measuring changes in resistance is ~18.5 mV/Ω when applying ~15 mA, the lowest current used for temperature sensing (larger applied currents improve the sensitivity). Coupled with the ~0.15 Ω/°C sensitivity of the Pt/Ti resistive element, the sensitivity for measuring changes in temperature is therefore ~2.8 mV/°C. Changes of 1°C in temperature therefore correspond to signals substantially larger than the noise currently in the circuitry, which is ~0.3 mV (standard deviation of mean over 500 samples measured at room temperature).

Another issue to consider is temperature uniformity. Simulations of the widened resistive element show that although temperature uniformity is still maintained within the reaction chamber and along the length of the resistive element, temperature variations along the width of the resistive element can be significant (~10°C) when it undergoes resistive heating. Because these temperature variations are not present in the resistance vs. temperature calibration of the resistive element (done in a water bath with uniform temperature), their effect on temperature sensing accuracy needs to be characterized.

With a heat sink is implemented, the power required to maintain the reaction chamber at ~95°C (for the current PCR microchip architecture) increases to ~2 W (discussed in chapter 4). This power requirement approaches the limitations of USB power (2.5 W). As a result, the maximum temperature that can be attained at the resistive element and hence the maximum heating rate of the reaction chamber (from applying maximum power) may be limited. Also, there may be insufficient power for operating other functionalities (e.g. thermoelectrically-actuated microvalves). As a result, with a heat sink implemented, the current microchip architecture may not be suitable for USB power. The reaction chamber would likely have to be miniaturized further to reduce the power requirements (as described earlier in 5.6.1).

5.6.3 Other resistive element materials

Platinum is a highly suitable material for building temperature sensors since its resistance depends strongly and linearly upon temperature over a large range. However, because it is expensive (~$240 for 200 nm thick film at the U of A Nanofab), moving towards more inexpensive metals would greatly reduce the manufacturing cost of the resistive element. Polysilicon [8, 9] and tungsten [10] are other materials that have been commonly used by others as thin film heaters in on-chip PCR devices. Preliminary work at the AML has explored the possibility of using a titanium tungsten (TiW) alloy, which is more readily available and much easier to pattern than Pt/Ti since etching processes are more readily employed. Resistive elements using the same design as presented in chapter 2 were fabricated out of TiW instead of Pt/Ti (thickness adjusted to maintain roughly the same

electrical resistance). Water bath calibrations of these resistive elements (as described in chapter 2) revealed they are not as sensitive to temperature as the Pt/Ti elements, and that their resistance vs. temperature relationship was quadratic rather than linear (Figure 5-9). Since typical operating temperatures for the resistive element exceed the temperature range of the water bath, an alternate method of calibrating the resistive elements (e.g. oil bath or oven) may be required to ensure accurate characterization since we cannot extrapolate a linear relationship like for Pt/Ti. Nevertheless, the results show less expensive materials can be used for the resistive element provided that the proper adjustments are made to the drive circuitry (e.g. Wheatstone bridge for a more accurate difference measurement, signal amplifiers for improving sensitivity, and RC filters for noise reduction) to account for the differences from Pt/Ti (e.g. lower sensitivity and non-linear resistance vs. temperature relationship). As described earlier in section 5.6.2, the currently used source measurement unit circuitry provides a sensitivity of at least ~18.5 mV/Ω (translates into ~2.8 mV/°C with Pt/Ti) with noise being ~0.3 mV.
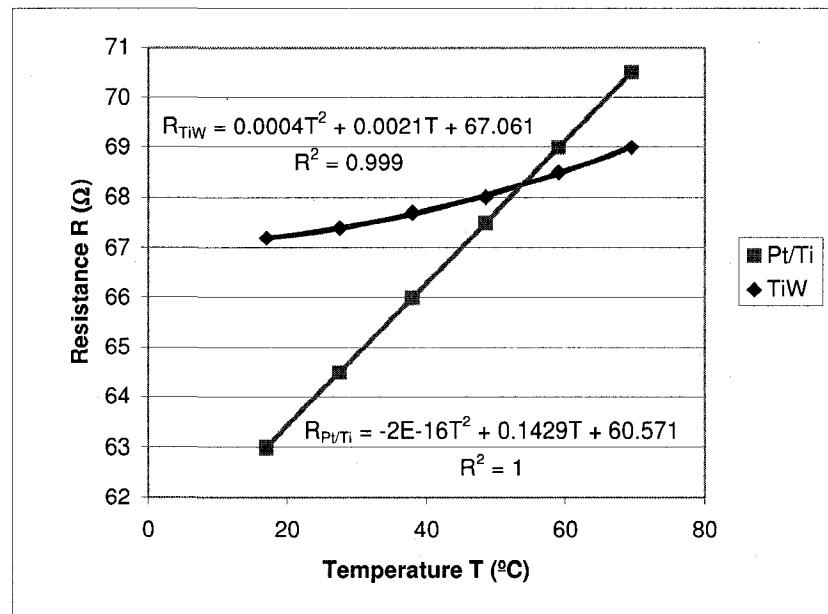
Figure 5-9. Resistance vs. temperature curves for a TiW and a Pt/Ti resistive element.

5.7 FINAL CONCLUSIONS

A microfluidic chip heating system utilizing a single resistive element to perform both heating and temperature sensing has been developed and demonstrated. FE modeling was used to design the geometry of the resistive element and of the microchip such that temperature uniformity is maintained on the resistive element (required for temperature sensing) and within the reaction chamber of the microchip (required for many biochemical reactions such as PCR). To control the temperature at the reaction chamber using the temperature measured at the resistive element, the linear relationship between them was determined using a combination of experimental measurements and finite element modeling. This relationship holds only at steady-state and was found to be accurate to 1°C. The developed microchip and temperature control approach were capable of performing the thermal cycling required for the genetic amplification of various templates relevant to cancer diagnostics and viral detection.

However, due to the inherently low thermal conductivity of the glass-based microchip, the passive cooling rate of the reaction chamber was quite slow and the cooling stage represented a significant portion of the time required to perform thermal cycling. Furthermore, the thermal equilibration time of the microchip was also relatively slow (on the order of minutes), resulting in significant overshoots/undershoots (±2-3°C) during transitions between temperature stages, which can adversely affect the quality of the genetic amplification. These problems were overcome by implementing a heat sink to greatly improve the passive cooling rate of the microchip and to substantially reduce the parasitic thermal capacitance (faster thermal equilibration time). To ensure heating rates and power consumption were not greatly affected by the heat sink, FE modeling was used to determine the optimum spacing required between the heat sunk area and the vicinity of the resistive element. With the heat sink in place, thermal cycling times were greatly improved (due to a much shorter cooling stage) and the overshoots/undershoots were eliminated. To further shorten the time required for performing genetic amplification, shorter temperature stages as well as a two-stage PCR protocol were implemented as well. With both instrumental and protocol improvements, 35 PCR cycles could be performed in ~30 minutes.

The single resistive element heating strategy developed in this thesis has been well tested, being used to amplify different clinically relevant templates and also readily adapted for use in other applications as well, such as fluorescence in situ hybridization and thermoelectrically actuated microvalves, particularly because the thermal module remains thermally independent of the rest of the microchip. It is now a useful building block that can be used to develop, for example, practical systems for performing genetic analyses in a clinical setting. Further miniaturization of the thermal system would substantially improve its temperature ramping rates, allow a larger number of thermal modules to be placed in a single given microchip size, and allow for more thermal modules to be operated simultaneously under the same power budget, making more complex microchip designs and protocols possible while remaining suitable for use in a portable and inexpensive platform. Work is currently underway to integrate other functionalities with the single resistive element heating unit as well as to further improve its manufacturability.

5.8 REFERENCES

[1]   Hjerten, S., "High-performance electrophoresis: elimination of electroendosmosis and solute adsorption", *Journal of Chromatography*, 1985. **347**: p. 191-198.

[2]   Toriello, N.M., C.N. Liu, and R.A. Mathies, "Multichannel reverse transcription-polymerase chain reaction microdevice for rapid gene expression and biomarker analysis", *Analytical Chemistry*, 2006. **78**: p. 7997-8003.

[3]   Kricka, L.J. and P. Wilding, "Microchip PCR", *Analytical and Bioanalytical Chemistry*, 2003. **377**: p. 820-825.

[4]   Vahedi, G., C. Kaler, and C.J. Backhouse, "An integrated method for mutation detection using on-chip sample preparation, single-stranded conformation polymorphism, and heteroduplex analysis", *Electrophoresis*, 2004. **25**(14): p. 2346-2356.

[5]   Kaigala, G.V., V.N. Hoang, A. Stickel, J. Lauzon, D.P. Manage, L.M. Pilarski, and C.J. Backhouse, "Fully portable and inexpensive microchip-based genetic analysis platform

for integrated RT-PCR and capillary electrophoresis", *The Analyst*, Accepted December 2007.

[6] Sieben, V.J., C.S. Debes-Marun, P.M. Pilarski, G.V. Kaigala, L.M. Pilarski, and C.J. Backhouse, "FISH and chips: chromosomal analysis on microfluidic platforms", *IET Nanobiotechnology*, 2007. **1**(3): p. 27-35.

[7] Song, W.H., J. Kwan, G.V. Kaigala, V.N. Hoang, and C.J. Backhouse, "Readily integrated, electrically-controlled microvalves", *Journal of Micromechanics and Microengineering*, Submitted Sept 2007.

[8] DeVoe, D.L., "Thermal Issues in MEMS and Microscale Systems", *IEEE Transactions on Components and Packaging Technology*, 2003. **25**(4): p. 576-583.

[9] Lee, C.-Y., G.-B. Lee, H.-H. Liu, and F.-C. Huang, "MEMS-based temperature control systems for DNA amplification", *International Journal of Nonlinear Sciences and Numerical Simulation*, 2002. **3**: p. 215-218.

[10] Liu, J., M. Enzelberger, and S. Quake, "A nanoliter rotary device for polymerase chain reaction", *Electrophoresis*, 2002. **23**(10): p. 1531-1536.

Appendix A

Analytical modeling

In this appendix, simplified electrically equivalent circuits of the thermal system of the developed PCR microchip are analyzed to corroborate some of the results derived from the finite element models used in this thesis, helping to verify their accuracy.

[I] Background

As described in chapters 2 and 4, temperature differences are analogous to voltage differences, heat flow is analogous to electrical current, and thermal conductivities and capacitances are analogous to their electrical counterparts.

Heat conduction in 3D is governed by the following partial differential equation (PDE) [1]:

$$\nabla^2 T + \frac{\dot{g}}{k} = \frac{1}{\alpha}\frac{\partial T}{\partial t} \tag{A-1}$$

where $T(x, y, z, t)$ is temperature as a function of space and time (K)

$\dot{g}$ is the rate of heat generation per unit volume (W/m³)

k is thermal conductivity (W/m·K)

α is the thermal diffusivity (m²/s) $\alpha = \dfrac{k}{\rho c}$

where ρ is the density (kg/m³) and c is the specific heat capacity (J/kg·K)

The same material properties as those used in the simulations are employed here:

Material	Thermal Conductivity k (W/m·K)	Specific Heat Capacity c (J/kg·K)	Density ρ (kg/m³)
Borofloat glass	1.11	830	2200
PDMS	0.18	1100	1030

100

In the steady-state case, the time derivative becomes zero and equation (A-1) is reduced to Poisson's equation:

$$\nabla^2 T = -\frac{\dot{g}}{k} \qquad\qquad (A\text{-}2)$$

The PDE governing electrostatics also has the same Poisson's equation form [2], demonstrating the analogy between heat transfer systems and electrical systems:

$$\nabla^2 V = -\frac{q}{\varepsilon} \qquad\qquad (A\text{-}3)$$

where V is the electric potential (V)

q is the electrical charge density (C/m^3)

ε is the permittivity (F/m)

Therefore, in the steady-state, a thermal system can be treated as a network of thermal resistances (resistive dividers), which are a function of k and of geometry. For certain simple geometries, thermal resistances can be calculated as follows [1]:

Conduction between two parallel planes   Conduction between two concentric spheres
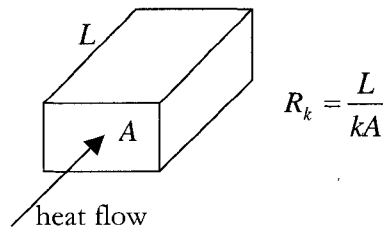
$$R_k = \frac{L}{kA}$$

$$R_k = \frac{r_2 - r_1}{4\pi k r_1 r_2}$$

Conduction between two concentric cylinders

$$R_k = \frac{\ln(r_2 / r_1)}{2\pi k l}$$
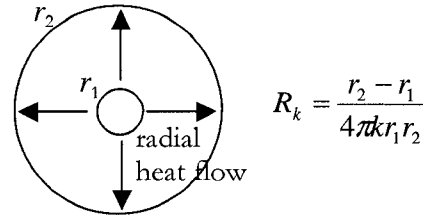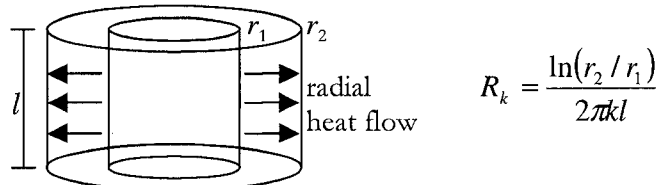
Convection is governed by Newton's Law of Cooling [1]:

$$\dot{Q} = hA(T - T_{ext}) \qquad\qquad (A\text{-}4)$$
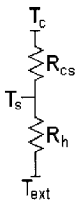
where $\dot{Q}$ is the rate at which heat is dissipated (W)

h is the heat transfer coefficient (depends on properties of the surrounding fluid such as its velocity, $h = 5.6$ W/m^2·K for natural convection in air)

A is the area of the surface through which convection occurs (m^2)

T is the temperature at the surface through which convection occurs (K)

T_{ext} is the temperature of the surrounding fluid (K)

Comparing this to I = ΔV/R (heat flow is analogous to electrical current and temperature is analogous to voltage), the thermal resistance due to convection can be defined as:

$$R_h = \frac{1}{hA} \qquad\qquad (A\text{-}5)$$

[II] Offset between T_c and T_s

In chapter 2, simulations were used to do a 'short' extrapolation of T_s to T_c. With the thermal resistance formulas above, we can estimate how large the offset between T_s and T_c should be. Using a resistive divider model, given T_c and T_{ext} (using 94°C and 22°C respectively here), we can calculate T_s using equation (A-6) if we know the ratio between the thermal resistances between T_c and T_s (R_{cs}) and T_s and T_{ext} (R_h):

$$T_s = T_{ext} + \left(T_c - T_{ext}\right)\frac{R_h}{R_{cs} + R_h} = T_{ext} + \frac{T_c - T_{ext}}{R_{cs}/R_h + 1}$$

(A-6)

Because of its geometry, the actual thermal resistance values for the microchip are difficult to calculate using first principles. Nevertheless, simpler geometries (as presented above) can be analyzed to provide an estimate of what should be expected:

Approximation 1. Infinite planes:

The simplest case to consider is one where heat from the reaction chamber flows vertically, conducting through the top glass layer and leaving the microchip via natural convection. The infinite planes are separated by the thicknesses of the corresponding microchip layers. Applying the R_k formula for infinite planes to equation (A-6), we obtain:

$$\frac{R_{cs}}{R_h} = \frac{L/kA}{1/hA} = \frac{hL}{k} = \frac{5.6(0.0011)}{1.11} = 0.0056$$

$$T_s = 22°C + \frac{94°C - 22°C}{0.0056 + 1} = 93.6°C$$

1.1 mm thick glass — T_s

0.254 mm thick PDMS — T_c

1.1 mm thick glass

T_s is therefore very close to T_c (0.4°C difference) in this geometry. Simulations of the actual microchip geometry show T_s and T_c differ by ~10°C when T_c is at 94°C. The discrepancy is due to the difference in the geometries considered (the chamber is not an infinite plane).

Approximation 2. Spherical planes:
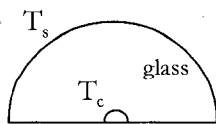
Because the chamber is finite in the actual microchip geometry, a more accurate approximation may be to consider it as a "point source" where heat propagates radially through a hemisphere. The outer radius is considered to be the thickness of the glass (1.1 mm) while the inner radius is considered to be the height of the chamber (0.09 mm). Applying the R_k formula for concentric spheres to equation (A-6), we obtain:

102

$$\frac{R_{cs}}{R_h} = \frac{\dfrac{r_2 - r_1}{2\pi k r_1 r_2}}{\dfrac{1}{hA}} = \frac{\dfrac{r_2 - r_1}{2\pi k r_1 r_2}}{\dfrac{1}{2\pi h r_2^2}} = \frac{h r_2}{k r_1}(r_2 - r_1) = \frac{5.6(0.0011)}{1.11(0.00009)}(0.0011 - 0.00009) = 0.062$$

$$T_s = 22^\circ C + \frac{94^\circ C - 22^\circ C}{0.062 + 1} = 90^\circ C$$

With this geometry, the offset between T_c and T_s (4°C) is larger than with the infinite planes, but is still smaller than in simulations of the actual microchip (10°C). The discrepancy is again due to the fact that the actual microchip geometry is different. Because in the actual microchip geometry, the top glass surface (where convection occurs) is a plane, most of the heat flow would have to travel through more glass to reach it than in the spherical model considered here. As a result, since R_{cs} would be larger, we would indeed expect the offset between T_c and T_s to be larger in the actual microchip geometry.

Nevertheless, the analytical models confirm that T_s should indeed be close to T_c as observed in the simulations of the microchip.

[III] Equilibration time of the microchip

Rearranging the heat conduction equation (A-1) into the following form provides a better idea of what the time derivative term represents:

$$\dot{g} = -k\nabla^2 T + \rho c \frac{\partial T}{\partial t} \tag{A-7}$$

$$I = \frac{V}{R} + C\frac{dV}{dt} \tag{A-8}$$
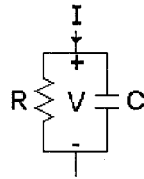
Bearing in mind the analogies of heat flow to electrical current and of temperature to voltage (as with equation A-4), the heat conduction equation (equation (A-7)) resembles the equation describing the electrical current flowing through a parallel RC circuit (equation (A-8)). In both equations, the first term describes the time independent resistive effects (like electrostatics) while the second term describes the time dependent capacitive effects. Equation (A-7) is in a spatially distributive form while equation (A-8) is in a discrete form. We can therefore treat the thermal problem as a network of parallel RC circuits.

When considering heat conduction and convection in a body, if the ratio of thermal resistance due to convection over thermal resistance due to conduction (defined as the Biot number) is small (<0.1), temperatures within the microchip will tend to equilibrate and become uniform, and as a result, the body can be treated as a lumped system with one R and one C (i.e. a single parallel RC circuit where R is the thermal resistance due to convection and C is the total heat capacity of body).

103

As discussed in chapters 2 and 4 (and shown above), this low Biot number case is indeed the situation in the PCR microchip. However, a lumped analysis assumes temperatures within the microchip are uniform, and is thus only accurate if this is the case. During active heating, because the resistive element is located inside the microchip, substantial temperature gradients are formed and the temperatures in the microchip cannot be considered uniform. Hence, the lumped system analysis cannot be expected to give accurate results.

Nevertheless, we can apply a lumped system analysis more accurately when the microchip is undergoing passive cooling since no active heating occurs. This analysis allows us to estimate the RC time constant of the microchip as it cools.

The thermal resistance of the microchip is attributed mainly to natural convection at all its external boundaries except the bottom surface of the microchip, which is insulated.

$$R = \frac{1}{hA} = \frac{1}{5.6[(0.05)(0.014) + 2(0.05)(0.002454) + 2(0.014)(0.002454)]} = 176 K / W$$

areas of each surface where convection occurs

The thermal capacitance of the microchip is the sum of the capacitances of each layer. The capacitance of each layer is calculated by multiplying the specific heat capacity of the layer by its density and its volume.

$$C = A\left[2(\rho c t)\big|_{glass} + (\rho c t)\big|_{PDMS}\right]$$

A is the area of the microchip, while t is the thickness of each layer

$$C = (0.05)(0.014)[2(2200)(830)(0.0011) + (1030)(1100)(0.000254)] = 3.0 J / K$$

$$\therefore RC = (176 K / W)(3.0 J / K) = 528 \sec = 8.8 \min$$

The time constant of the microchip is estimated to be ~8.8 min. As described in chapter 5, simulations show ~10 min. is required for the chamber temperature to reach room temperature when no heat sink is implemented. This is slightly faster than what the analysis here suggests. The discrepancy is due to the fact that the lumped system analysis here assumes the temperatures in the microchip are uniform throughout the duration of the cooling stage. On the other hand, in the simulations (and in actual experiments), cooling starts from a state where there is a large temperature gradient in the microchip (with the resistive element being at the highest temperature and regions far away from it at significantly lower temperatures). Nevertheless, the lumped system analysis confirms that an RC time constant on the order of minutes should be expected, and this is observed in the simulations (and experimentally as well).

[IV] Effect of heat sink on the equilibration time of the microchip

With a heat sink implemented (placed 3.5 mm from the center of the reaction chamber as described in chapter 4), to apply a lumped system analysis, we can consider the heated volume to be the region of the microchip enclosed by the heat sink (i.e. a cylinder with a radius of 3.5 mm).

During cooling, the dominant heat flow is via conduction from the chamber (radius of 1.5 mm) to the heat-sunk region (radius of 3.5 mm). Using the equation for the thermal resistance between two concentric cylindrical surfaces and considering the resistances of each microchip layer are in parallel, we obtain the following estimate for the thermal resistance of the heat-sunk microchip:

$$R = \left[2R_{glass}^{-1} + R_{PDMS}^{-1}\right]^{-1} = \left[2\left(\frac{2\pi(1.11)(0.0011)}{\ln(3.5/1.5)}\right) + \frac{2\pi(0.18)(0.000254)}{\ln(3.5/1.5)}\right]^{-1} = 54.2 K/W$$

The thermal capacitance can be estimated by again summing the capacitances of each layer, but considering only the area of the heated volume (radius of 3.5 mm) rather than the entire microchip:

$$C = A\left[2(\rho ct)\big|_{glass} + (\rho ct)\big|_{PDMS}\right]$$
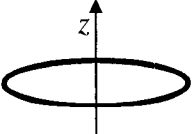
$$C = \pi(0.0035)^2\left[2(2200)(830)(0.0011) + (1030)(1000)(0.000254)\right] = 0.166 J/K$$

$$\therefore RC = (54.2 K/W)(0.166 J/K) = 9.0 \sec$$

The implementation of a heat sink therefore reduces the time constant of the microchip from the order of minutes to the order of seconds. Such an improvement was observed both experimentally and in simulations.

[V] Power consumption of the microchip

Electrostatics provide us with a simple analytical formula for the electrical potential along a perpendicular axis through the center of an electrically charged ring with a total charge Q and a radius R [3]:

$$V(z) = \frac{Q}{4\pi\varepsilon\sqrt{z^2 + R^2}} \qquad\qquad (A-9)$$

Using the analogy of electrostatic systems for steady-state thermal systems (i.e. comparing equations A-2 and A-3), we can substitute temperature T for voltage V, and P/k for Q/ε (k is the thermal conductivity, ε is the electrical permittivity, P is the rate of total heat

generated, i.e. power, and Q is the total electrical charge), yielding the following equation for the temperature along a perpendicular axis through the center of a ring-shaped heater:

$$\Delta T(z) = T - T_{ext} = \frac{P}{4\pi k \sqrt{z^2 + R^2}} \qquad\qquad (A-10)$$

Note though that in electrostatics (equation A-9), the reference electrical potential (at infinity) is considered to be zero. For our thermal system (equation A-10), the reference temperature (at infinity) is considered to be room temperature. Furthermore, equation A-10 assumes the heater ring is infinitely surrounded with one material (with one k). This is not the case for our microchip, where the heater ring is located between glass and PDMS layers of finite thickness, but nonetheless, equation A-10 can be used to provide an estimate of the power required to operate the microchip (maintain 94°C in the reaction chamber) with no heat sink implemented.

For PDMS:
$$P = 4\pi k \sqrt{z^2 + R^2}\,(T - T_{ext}) = 4\pi(0.18)\sqrt{0.000254^2 + 0.0025^2}\,(94 - 22) = 0.41\,\text{W}$$

For glass:
$$P = 4\pi k \sqrt{z^2 + R^2}\,(T - T_{ext}) = 4\pi(1.11)\sqrt{0.000254^2 + 0.0025^2}\,(94 - 22) = 2.5\,\text{W}$$

From simulations and experiment, with no heat sink implemented, the power required to maintain 94°C in the reaction chamber is ~1 W, which is between the values calculated above. The simulations and experimental results therefore match in order of magnitude with the analytical estimations.

The above formula also predicts that the power consumption of the microchip scales linearly with the size of the microchip (i.e. if the dimensions of the microchip are halved, so is the power consumption), an observation that is expected analytically and also corroborated by FEM simulations (section 5.6.1).

References

[1]   Lienhard IV, J.H. and J.H. Lienhard V, *A Heat Transfer Textbook*. 3rd ed. Cambridge: Phlogiston Press, 2005.
[2]   Griffiths, D.J., *Introduction to Electrodynamics*. 3rd ed. Upper Saddle River, NJ: Prentice Hall Inc., 1999.
[3]   Halliday, D., R. Resnick, and J. Walker, *Fundamentals of Physics*. 6th ed. New York: John Wiley & Sons, Inc., 2001.

Appendix B

Analysis of the effect of room temperature

on the chamber temperature

In an attempt to establish the effect of varying ambient temperature (T_{ext}) on the chamber temperature (T_c) during the PCR operation, we make use of a combination of simulation, experimental and analytical techniques as described below.

Simulation Results:

FE simulations (tri-layer microchip, all external surfaces have convection except the bottom surface which is thermally insulated) have shown that varying room temperature (T_{ext}) by 5°C (i.e. from 17°C to 27°C) results in a 0.5°C change in the chamber temperature (T_c) both at the 94°C and the 60°C stage.

Experimental Results:

Measurements of T_s using a thin wire thermocouple attached to the top of the microchip could vary by 1°C (variations due to thermal contact of the thermocouple, determined from successively reattaching it and measuring T_s). Day-to-day measurements of T_s did not vary by more than 1°C from the expected values (the value that our FE model predicts will be attained when the desired T_c is reached). Therefore, day-to-day variations in T_{ext} cause changes smaller than the error in measuring T_s (1°C). Since T_s is thermally closer to T_{ext} than T_c, we expect variations in T_{ext} to have an even smaller effect on T_c than T_s.

107

Analytical Model:

For an analytical explanation, using the electrically equivalent model (resistive divider model as in chapter 2), we estimate the effect of changing T_{ext} on T_c (at the steady-state case).
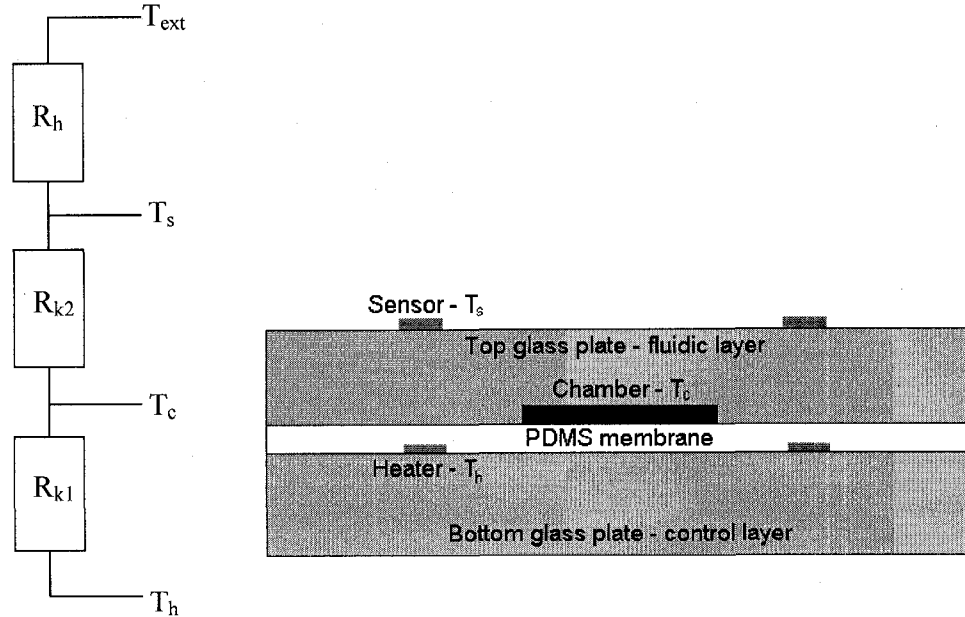
R_h is the thermal resistance due to convection between the top of the chip and air.
R_{k2} is the thermal resistance due to conduction between the chamber and the top of the chip.
R_{k1} is the thermal resistance due to conduction between the heater and the chamber.

- T_h is determined by the temperature controller and hence is always the same between different runs, but the room temperature T_{ext} can fluctuate.

- Heat conduction equation: $Q = \rho C \dfrac{\partial T}{\partial t} + \nabla \cdot (-k \nabla T) \Rightarrow R_k = f(k)$

  Heat convection equation: $Q = -hA(T_{ext} - T) \Rightarrow R_h = f(h, A)$

  The R_k values depend on geometrical factors and on the thermal conductivities of the glass and PDMS, which do not vary significantly with temperature. The R_h value depends on the surface area (A) exposed to air and the h value, and both also do not vary with temperature (the h value embodies all factors other than geometry and temperature that affect convection, e.g. airflow velocity). Therefore, the R_k and R_h values should be constant with fluctuations in T_{ext}, particularly for the small range of fluctuations in T_{ext} that we are considering.

- Though it is difficult to assign specific numbers to the R values (this would require either measurements of heat flux or a complicated spatial integration of thermal conductivities), we can readily determine the ratio between R values with the temperature measurements we have made (the data used to determine the T_c vs. T_h relationship, as in chapter 2).
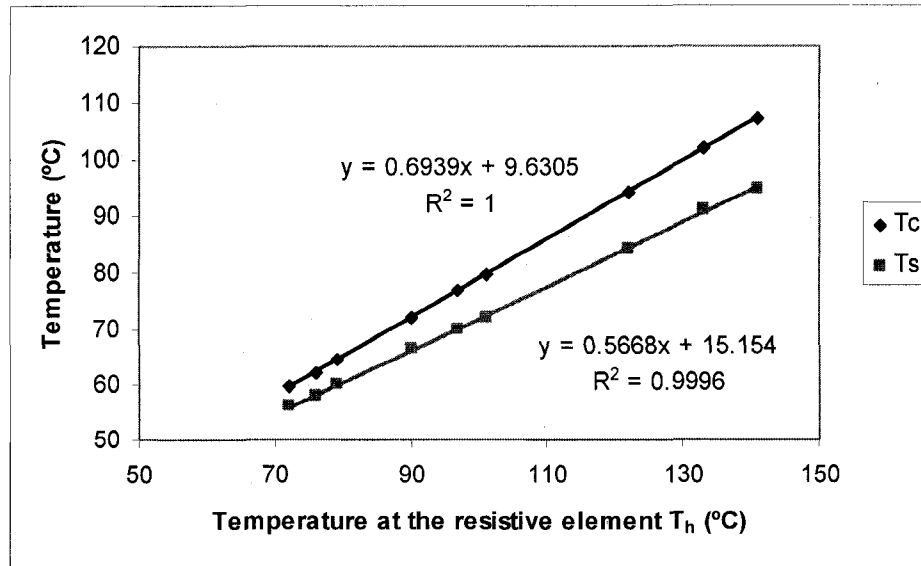
Define r = ratio of thermal resistance between T_h and T_c to thermal resistance between T_h and T_{ext}

$$r = \frac{R_{k1}}{R_{k2} + R_h} = \frac{T_h - T_c}{T_h - T_{ext}}$$

where T_h is the measured temperature at the resistive element, T_c is the calculated temperature, and T_{ext} is 22°C (typical room temperature).

A small r value implies T_c is thermally much closer to T_h than to T_{ext}, and thus T_{ext} has a minimal effect on T_c. Conversely, a large r value implies T_c is thermally much closer to T_{ext} than to T_h, and thus T_{ext} has a large effect on T_c.

From the data in chapter 2 (above plot), we can get the r value of our microchip:

T_h (Measured temperatures at the resistive element)	T_c (Chamber temperatures from FEM)	r (Ratio)
79	64.5	0.254386
101	79.6	0.270886
141	107.4	0.282353
133	102.1	0.278378
76	62.2	0.255556
97	76.9	0.268
122	94.2	0.278
72	59.7	0.246
90	72.2	0.261765
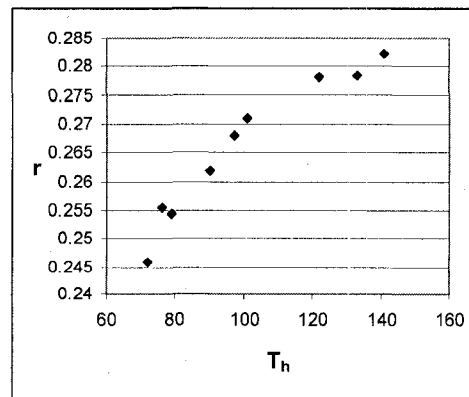
The average r value is 0.266 and it varies from 0.245 to 0.285, which tends to increases with rise in T_h. Since T_h is constant between different runs (because of the temperature controller), using r = 0.285 for the worst-case scenario, we get:

$$T_h - T_c = r(T_h - T_{ext}) \Rightarrow \Delta T_c = r\Delta T_{ext} \Rightarrow \Delta T_{ext} = \frac{\Delta T_c}{r} = \frac{1°C}{0.285} = 3.5°C$$

Therefore, with our experimental data and the analytical model (i.e. the resistive divider model), we can predict that in a worst-case scenario, when there is a change of 3.5°C in T_{ext}, this will result in a change of 1°C or less in T_c.

Discussion:

- The effect of fluctuations in T_{ext} on T_c essentially depends on the amount of thermal resistance separating these temperatures. In our case, since glass has a low thermal conductivity and we are relying only on natural convection (which is not very large), the chamber is sufficiently "insulated" from room temperature such that changes of 3.5°C in room temperature will not affect the chamber by more than 1°C (from experimental and analytical predictions). If, for example, we were using a silicon-based chip (higher thermal conductivity) with forced convection, fluctuations in T_{ext} would have a much larger effect on T_c since they are thermally much closer to each other (less "insulation").

- The T_c vs. T_h relationship we use to control T_c is specific to the microchip architecture used (i.e. the thermal resistances in the microchip) and the conditions under which it is characterized (i.e. room temperature and the thermal resistance to it and the microchip). The relationship we establish is accurate to 1°C as long as the room temperature does not fluctuate by more than 3.5°C from the temperature at which the relationship was characterized. If the microchip is to be operated at a substantially (>3°C) different T_{ext}, the T_c vs. T_h relationship needs to be recharacterized to maintain accuracy. Also, if we needed to regularly deal with large changes in T_{ext}, we could characterize the T_c vs. T_h relationship at various T_{ext} and obtain a 3D mapping of T_c vs. T_h and T_{ext}. With such a 3D mapping function, our control strategy should work for large changes in T_{ext}.

- Heat sink scenario – Including a heat sink tends to reduce the thermal resistance between the microchip and its surrounding environment and hence we can expect a greater increase in the effect of environmental fluctuations (i.e. T_{ext}) on T_c. However, we have designed our heat sink such that the area directly below the reaction chamber is not heat-sunk, allowing for some thermal resistance (due to the glass) between T_c and T_{ext}. By optimizing the spacing between the heat sink and the chamber, we ensure heating rates are not substantially hampered and that fluctuations in T_{ext} do not greatly affect T_c (we still experimentally observe that day to day variations in T_{ext} do not change the measured T_s by more than 1°C).

Appendix C

Protocols for microchip calibration and operation

[I] Resistance vs. Temperature calibration

Newly-fabricated Pt/Ti resistive elements (for temperature sensing) should undergo annealing and calibration. Annealing involves maintaining the temperature of the resistive element at a temperature significantly higher than its normal operating temperature to relieve the stresses built up in the thin film during deposition. Pt grains enlarge, and as a result of less grain boundaries, the overall resistivity of the thin film decreases. The annealing step ensures this change in resistivity will not occur during the normal operation of the resistive element. The resistive elements used in this thesis typically had a resistance of $70 \pm 5 \, \Omega$ at room temperature. Profilometer measurements have shown the variation is mainly due to thin film thickness variations across a substrate (thicker near the middle of the substrate). The annealing step typically reduces the resistance at room temperature by $\sim$2-3 Ω.

Annealing:
1) The resistive element should be annealed for at least 2 hours at $\sim$200°C (at atmosphere) since the highest operating temperature for performing PCR is $\sim$170°C (does not need to be exact, just needs to be substantially higher than the highest operating temperature). Note that PDMS will melt at $\sim$200°C so the annealing step must be performed on unbonded control layers.

2) This can be done by using a DC power supply to apply $\sim$12 V to the resistive element (crocodile clips were attached directly). A thin wire thermocouple can be used to monitor the temperature of the resistive element ($\sim$20°C difference if attached on the side without the element, measurements were reproducible to within $\sim$1°C with the error being due to thermal contact). This method was used for the work in this thesis.

3) Alternatively, the resistive elements can be placed in an oven maintained at $\sim$200°C for $\sim$2 hours, which would allow the annealing of several resistive elements at once.

Calibration, which is performed after annealing, involves determining the linear relationship between the resistance and the temperature of the resistive element. The slope of this relationship is required for temperature sensing (depends on TCR and on resistance at room temperature. Annealing and calibration only need to be performed once after the chip is fabricated, and are not required for subsequent runs or after rejuvenation/re-bonding of the chip (experiments have shown the slope does not change significantly in these cases).

Calibration:

1) Fill a water bath (Hakke C25P Circulator, this water bath has a circulating feature, which helps in maintaining more constant temperatures for calibrations) with deionized water.

2) Connect a multimeter (0.1 Ω precision or better) to the annealed resistive element for measuring resistance (crocodile clips were attached directly, measurements were reproducible to within 0.1 Ω).

3) Place the control layer inside a plastic bag along with some small weights (e.g. washers), and submerge the control layer in the water bath, squeezing as much air out of the bag as possible to ensure good thermal contact between the control layer and the water bath.

4) Set the temperature of the water bath. The water bath takes ~15 minutes to equilibrate at a set temperature (when heating up, it will overshoot the set temperature by ~0.5°C). The temperature of the water bath can be monitored with an external thermometer to ensure accuracy.

5) Once the temperature of the water bath settles at the set value (after ~15 minutes), use the multimeter to measure the resistance of the resistive element. Note that if the resistive element does not remain dry, erroneous measurements can be made. Typically, measurements are made at 10°C intervals from 20°C to 70°C (and using the least squares method to determine the slope), though the data gathered so far suggests that taking 2 or 3 measurements can still give just as accurate of a R vs. T slope due to the highly linear R vs. T relationship of Pt. For the resistive element design used in this thesis, the R vs. T slope was 0.15 ± 0.01 Ω/°C.

[II] T_h vs. T_c calibration

The Resistance vs. Temperature calibration above only allows the temperature of the resistive element to be determined from measuring its resistance. In practice, for performing PCR, the temperature in the reaction chamber is the temperature of interest, and hence a separate calibration must be made to determine the relationship between the temperatures at the chamber and at the resistive element. This calibration is more complex, involving a combination of measurements and finite element modeling, and the relationship is specific to the microchip architecture/environment. The relationship only needs to be redetermined if a different microchip architecture is used (e.g. different microchip materials or layer thicknesses), or if the operating environment is significantly changed (e.g. implementing a heat sink). Also, if a microchip is scaled equally in all dimensions (i.e. including the thicknesses of its layers), the steady-state relationship will not change.

112

1) Using a thermocouple adhesive label, attach a thin wire (40 gauge) thermocouple (5TC-TT-K-40-36, Omega Engineering, Laval, Quebec, Canada) to the top of the microchip directly above the reaction chamber. A small drop of silicone heat transfer compound (MG Chemicals, Toronto, ON, Canada) should be used to ensure good thermal contact.

2) Place the microchip in its operating environment (e.g. TTK stage).

3) Apply various currents to the resistive element and once thermal equilibrium is reached (i.e. when measured temperatures become constant with time, can take ~15 mins.), record the resulting temperatures at the resistive element (T_h as measured from the resistance of the element) and at the top of the microchip (T_s measured by the thermocouple). The relationship between the steady-state T_s and T_h should be linear.

On a TTK (see the TTK/ folder in the supplementary data DVD for more details on the command line interface and its operation), this step can be done by entering the command "t2   *" in a HyperTerminal window (fill the 20 character window with spaces and with the last character being the checksum). This command will start a program that allows the user to set the DAC value (0-4095). The DAC value controls the applied current and can be thought of as a digitized form of the current. For the circuitry used in this thesis, the applied current in mA is roughly equal to the DAC value divided by 20. DAC values that yield temperatures in the operating conditions of the microchip (e.g. PCR temperatures) should be used.

4) The measured T_h and T_s values are then entered into a finite element model of the microchip (see Appendix E for modeling details) as temperature boundary conditions at the resistive element and at the top of the microchip respectively. Solving the model under the steady-state condition yields an estimate for the temperature in the reaction chamber, T_c. The obtained T_h vs. T_c relationship should be linear ($T_c = mT_h + b$) and holds true in the steady-state condition. For the thermal management system presented in chapter 4 (with a heat sink), it was found that difference between T_c and T_h is roughly 90% of the difference between T_s and T_h. The obtained T_h vs. T_c relationship is $T_h = 2T_c - 26$.

A second approach would be to consider a resistive divider model as in Appendix B, use the finite element model of the microchip to determine the ratios between the thermal resistances involved (by using simulated values of T_h, T_c, T_s, and T_{ext}), and use these ratios (like r in Appendix B) to determine T_c from the measured T_h and T_s. However, as shown in Appendix B, we found the thermal resistance ratios could vary significantly (e.g. $r = 0.26 \pm 0.02$) with temperature, and therefore the first approach described above was used instead.

5) The T_h vs. T_c relationship is used to determine the T_h required to maintain the desired T_c. It can be programmed into the TTK using the following HyperTerminal commands (xxxxxxxxxxxx represents the number that must be entered along with spaces to fill the 20 character window, and C is the corresponding checksum):
   For the slope (m):   dctslp#xxxxxxxxxxxxC   (e.g. dctslp#2.0   1)
   For the intercept (b):   dctint#xxxxxxxxxxxxC   (e.g. dctint#-26.0   0)

[III] T_h vs. DAC (initial PI values)

The data from the calibration test performed in [II] is also used to estimate the necessary initial PI controller parameter values for each temperature stage. These values are used by the PI temperature controller as the initial guess for determining the DAC value (i.e. electrical current) that should be applied to the resistive element, and should be close to the DAC value required to maintain the desired T_c at each temperature stage. The DAC value (0-4095) controls the current applied to the resistive element (like a digitized version of the current). The applied current vs. DAC value relationship is linear, but can vary slightly between different TTKs (due to slight differences in electrical components, it is characterized and entered into every TTK). As with the T_h vs. T_c relationship, the T_h vs. applied current relationship is specific to the microchip architecture and operating environment, but because the applied current vs. DAC relationship varies with circuitry, the T_h vs. DAC value relationship is specific to the circuitry as well.

1) From the data gathered in step 3 of [II], plot the T_h vs. the applied DAC value.

2) Apply a quadratic trendline and use the relationship to determine the DAC values (0-4095) required to obtain the T_h values required to maintain the desired T_c at each temperature stage (determined in [II]). A representative T_h vs. DAC relationship is the following: $T_h = 1.677 \times 10^{-5} (DAC)^2 - 0.01495 (DAC) + 35.08$.

3) These DAC values are the initial PI controller parameters and can be programmed into the TTK using the following HyperTerminal commands (xxxxxxxxxxxx represents the number that must be entered along with spaces to fill the 20 character window, and C is the corresponding checksum):

    RT stage: dIptRT#xxxxxxxxxxxxC
    94°C stage: dIpt94#xxxxxxxxxxxxC
    60°C stage: dIpt60#xxxxxxxxxxxxC
    72°C stage: dIpt72#xxxxxxxxxxxxC

[IV] Heating stages

As discussed in chapter 2, the T_h and the duration of the heating stages can be estimated using finite element modeling. The following procedure details how to experimentally adjust these values to ensure that temperature overshoots and undershoots are minimized.

1) Using a thermocouple adhesive label, attach a thin wire (40 gauge) thermocouple (5TC-TT-K-40-36, Omega Engineering, Laval, Quebec, Canada) to the top of the microchip directly above the reaction chamber. A small drop of silicone heat transfer compound (MG Chemicals, Toronto, ON, Canada) should be used to ensure good thermal contact.

2) Monitor the temperature overshoots/undershoots measured at the top of the microchip (T_s) by the thermocouple as thermal cycling is performed. As described in chapter 2, simulations have shown that overshoots/undershoots measured in T_s are ~1°C smaller than those experienced by T_c (they behave similarly over time).

3) Adjust the T_h and duration of the heating stages to minimize the overshoots/undershoots measured in T_s. For the TTK, these values can be adjusted using the following hyperterminal commands (xxxxxxxxxxxx represents the number that must be entered along with spaces to fill the 20 character window, and C is the corresponding checksum):

T_h of initial 94°C stage:	dtp94i#xxxxxxxxxxxxC
T_h of subsequent 94°C stages:	dtp_94#xxxxxxxxxxxxC
T_h of 72°C stages:	dtp_72#xxxxxxxxxxxxC
duration of initial 94°C stage:	dti94i#xxxxxxxxxxxxC
duration of subsequent 94°C stages:	dti_94#xxxxxxxxxxxxC
duration of 72°C stages:	dti_72#xxxxxxxxxxxxC

Note that the T_h for the initial 94°C stage is entered as is (e.g. 170, but for the other two cases, it is entered as the difference between T_h for the heating stage and the T_h during the PCR stage (e.g. 15). As for the durations, the number of seconds desired must be multiplied by ten and then entered (the TTK uses a sampling rate of ~100 ms).

[V] PCR microchip operation on a TTK

The following procedure outlines how to operate the PCR microchip in a TTK. The graphical user interface (GUI) used to operate the TTK can be found in the TTK/ folder in the supplementary data DVD along with a more detailed guide to its set-up and operation (the TTK related files in this folder are of the latest version available at the time of this thesis). The room temperature, the resistance of the heater at room temperature, and its pre-determined R vs. T slope are required inputs.

1) After turning on the TTK and starting the TTK GUI, position the chip inside the stage, making sure the o-rings and heater electrode pins are in place.

2) Go to RT-PCR tab of the TTK GUI, enter the heater resistance and slope, and click "Set the heater".

3) If this is the first time the heater is being used, the Wheatstone bridge needs to be balanced. Click on "calibrate", go to the terminal tab of the TTK GUI, and adjust the potentiometer until the voltage signal is on the edge of reading 0 V (i.e. moving the potentiometer a little bit will make the reading non-zero). "Calibrate" can be clicked as many times as necessary since the calibration signal is being activated only for a few seconds after this button is clicked, and it might happen that the user is unable the zero the Wheatstone bridge within that time frame. Note that the Wheatstone bridge should be balanced only when the heater is at room temperature.

4) The "calibrate" function can also be used to check if proper electrical contact is being made with the heater. If the electrical contact is good, the voltage signal in the terminal will read 0 V if heater is at room temperature or close to 0 V if the heater is slightly hotter. It will read 0.5 V if there is no electrical contact. In this case, the chip must be manually re-positioned.

5) Turn on the pressure and vacuum lines (external lines or mini-pumps). If hissing can be heard, the o-rings are not properly sealing and the chip must be repositioned. A few pumping cycles can be run to visually check that the valves actuate properly.

6) Pipet ~3 μL of PCR mix into the PCR input well of the chip and pump it into the PCR chamber using 2-3 1000 ms pumping cycles (see the TTK GUI handbook in the TTK/ folder of the supplementary data DVD for details on operating the valves). Check to ensure that there are no air bubbles in the PCR chamber (if there are, empty the chip using the pumping option again and retry), ensure all valves are sealed shut, and remove excess PCR mix from the PCR input well.

7) Choose RTPCR or PCR and enter the desired thermal cycling program parameters (sample, protocol, temperatures, times, number of cycles). Parameters from an earlier run can be loaded using the "load a file" option.

8) Once all parameters are entered, click on the "Load" button to input them and click on "Run" to start the thermal cycling. The run can be monitored by clicking on the terminal tab (this information is recorded in the RTPCR text file). The last column shows the cycle number while the second last column shows the heater temperature (not chamber temperature).

9) The run can be aborted by clicking the "Cancel" button.

10) After the run is completed, load the CE mix into the PCR input well, and use ten 1000 ms pumping cycles to flush the contents of the PCR chamber into the PCR output well (which is the CE input well). CE can then be performed to analyze the products (protocols for performing CE on a TTK and producing electropherograms can be found in the TTK/ folder in the supplementary data DVD).

Appendix D

TLC data analysis

[I] Data acquisition

- The PCR chamber is filled with a 1:2 dilution of the stock TLC suspension and placed in a plexi-glass stage. To view the colour changes, a black background is required and the TLCs should be viewed from directly above (a fiber optic cable connected to a spectrometer was suspended perpendicularly above the TLCs). The TLCs were illuminated by a white LED in conjunction with the fluorescent room lights.
- The raw reflected spectra of the TLCs were collected over time using the spectrometer (Ocean Optics USB2000, Dunedin, FL, USA) software (2 PCR cycles at sampling rate of ~100 ms), resulting in a 3D plot (absolute intensity vs. wavelength and time).
- Spectrometer data was collected before thermal cycling started. Therefore, the first spectrum collected is the background spectrum (i.e. when the TLCs are white).
    - o Comparing the background spectra from 5 different runs (Figure D-1b) under the same experimental set-up shows that there is significant variation in the absolute intensities (up to 10-20%).
    - o The raw data is also noisy (~5%).

Figure D-1 – Background spectrum
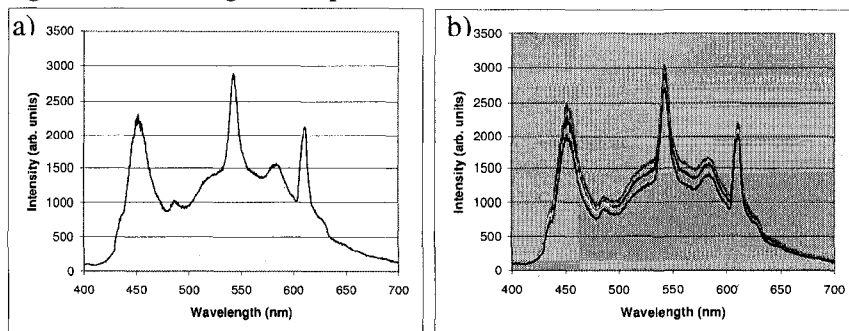
- To account for these variations in the background between runs, all the collected spectra were divided by the background spectrum (for every timepoint, the intensity at each wavelength is divided by the corresponding background wavelength intensity). We refer to the subsequent resulting data as the "divided data".
  - o The "divided data" is still a 3D plot, but is now a plot of relative/divided intensity vs. wavelength and time. A relative/divided intensity = 1 indicates no change from background. Any increases in intensity from background will have a relative/divided intensity > 1.
  - o This division step causes the red and green peaks in the spectrum to become indistinct.

[II] Extracting T vs. t trajectories

- Start with the divided data. To be able to compare the changes in different runs, we need to perform a normalization.
  - o This normalization is performed against the blue peak since it is the largest intensity peak, and also undergoes the largest changes with change in temperature. Red and green peaks do not change as significantly, but can be used as a consistency check for whether or not we are on the cooler side or the hotter side of the TLC colour change range.
  - o To reduce noise, the intensities over a ~15 nm bandwidth centered on the blue peak (roughly its FWHM) are averaged. These averaged, divided intensities are plotted over time (i.e. the blue peak has been extracted from the 3D plot of the divided data to produce a 2D plot of averaged, divided blue intensity vs. time).
  - o The same is done for the red and green peaks for use as a consistency check.
  - o In some of the data collected and plotted (roughly half), we observe a slight downward slope in the baseline, likely resulting from changing incident light (a dying battery in the LED used). If this is the case, the slope is removed (baseline adjusted to be flat) before moving on.
- The maximum value reached by the averaged, divided intensity of the blue peak throughout the entire run is determined. This value is referred to as B_{max}.
  - o B_{max} values ranged from 1.4-1.6 (1 = no change from background).
  - o Within a run (i.e. between two different PCR cycles), the **B_{max} value varied by less than 0.01.**
- The entire averaged, divided blue intensity vs. time plot is scaled by (divided by) B_{max}, yielding a 2D plot of normalized blue intensity vs. time. B_{max} is now represented by 1 (max value on this graph) and all other normalized blue intensities are now a fraction of 1.
  - o The same is done for the red and green peaks for use as a consistency check.
  - o Note that the normalized intensity is the same whether or not the background was divided or not for the blue peak. However, for the red and green peaks, dividing out the background affects the normalized intensity (normalized to blue).

118

o The value at which the normalized blue intensity settles (steady-state) for two different runs done with the same controller set-point **does not vary by more than 0.01** (Figure D-2, note that there is a shift in time between the two runs because they were not started at exactly the same time).

Figure D-2 – Comparison of normalized blue intensity vs. time plots for two different runs done with a 72°C set-point.
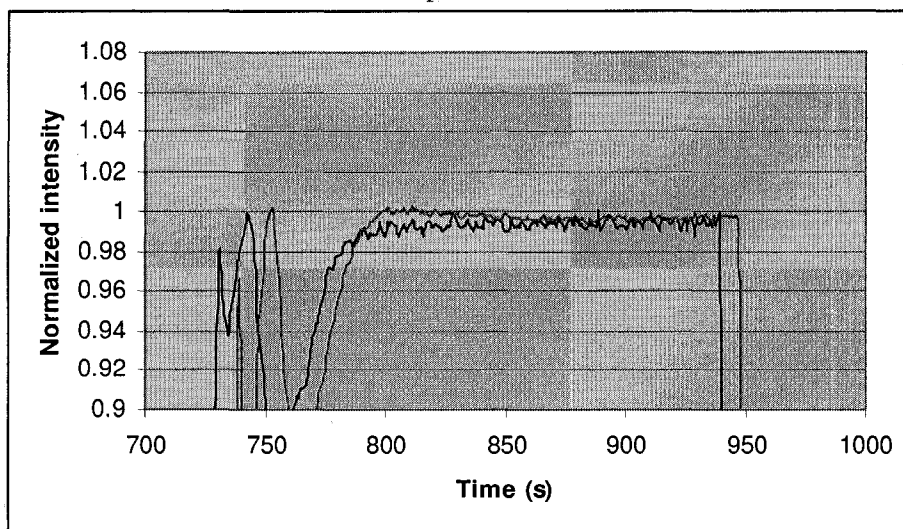
- The normalized blue intensity vs. time plots for runs done at different controller set-points are analyzed. The value at which the normalized blue intensity settles at (N_x) is correlated the set-point being used (T_x), yielding Table D-1.

Table D-1: Correlation of the normalized blue peak intensity to temperature

Set-point temperature (T_x)	Normalized blue peak intensity (N_x)
70°C	0.9014
72°C	0.9965
74°C	0.9632

o One assumption that we make in all of this is that the temperature of the TLCs inside the chamber is the same as the controller set-point.
o We know this assumption is justified because:
   - Predictions of T_s using simulations had matched with experimental measurements to 1°C.
   - Because of the small bandwidth of the TLCs used, we know if we see any colour at all (which we do), we must be within 2°C of the middle of the TLC colour change range (and within 1°C if we see blue).
o We have observed that the middle of the TLC colour change range (e.g. 72°C) gives an N value close to 1. As the temperature moves slightly higher or slightly lower, the N value decreases (Figure D-3).
o Therefore, **the behaviour of the normalized blue intensity vs. time as it settles down can tell us whether or not it is settling at a temperature on the**

119

higher or lower side of the TLC colour change range (e.g. higher or lower than 72°C).

- For example, if we are heating up and the **N value reaches 1** as it is settling (see a "hump"), the temperature is settling at a temperature higher than 72°C. If this does not occur, the temperature is settling at a temperature lower than 72°C. This can be used as a consistency check.

- Further we can also look at the behaviour of the normalized intensities of the red and green peaks as a consistency check. For example, the red and green normalized intensities are enhanced for temperatures below 72°C, but are at baseline for temperatures above 72°C.

- We can also tell which way the temperature is going by the order in which the peaks appear: red to blue means heating up, while blue to red means cooling down.

o It was found that in comparing different runs done with the same controller set-point and also in comparing the data from the two different cycles in one run, **the N_x values can vary by up to 0.01.**

- **This is smaller than the difference between the N_x values for different set-points,** but still comparable to the difference between the N_x values for set-points 1°C apart (e.g. 71°C and 73°C had N values of ~0.98, compare to Table D-1 above).

- Therefore, for plotting the T vs. t trajectories, temperature crossing points from T_x values separated by 2°C (rather than 1°C) were used.

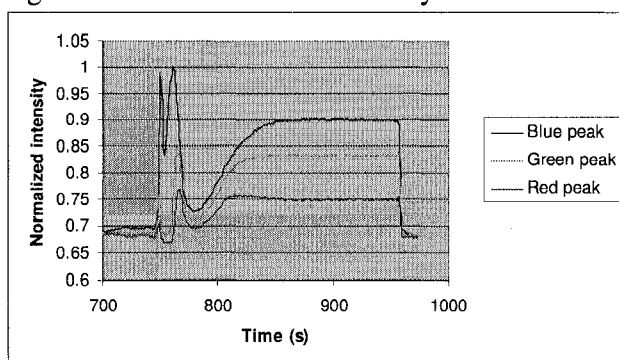Figure D-3a - Normalized intensity vs. time for 70°C set-point

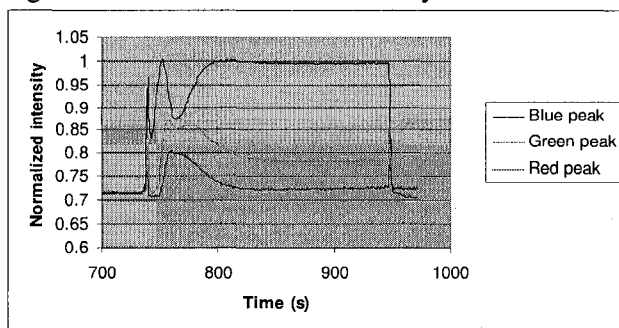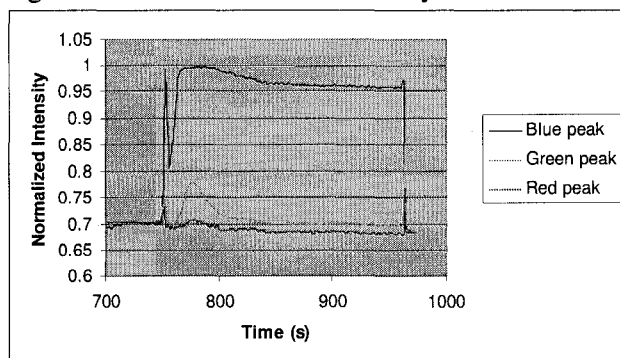Figure D-3b - Normalized intensity vs. time for 72°C set-point

Figure D-3c - Normalized intensity vs. time for 74°C set-point

- The times at which the normalized blue intensity crosses the N_x values determined above (Table D-1) are recorded and translated into temperature crossing points (T_x) (Figure D-4).
    - o Our smallest change in N_x between set-points 1°C apart is ~0.02. With this guideline, the variation of 0.01 in our N_x values (for the same given set-point) translates into a maximum variation of ~0.5°C. **Hence, the temperature as measured from the TLCs is within 0.5°C of the set-point temperature.**
- A clamped cubic spline is fitted to these temperature crossing points to give us our T vs. t trajectory.
    - o A slope of 0 is specified for the end (since T should be levelling off) and the slope at the beginning is estimated by using the slope between the first two temperature crossing points (roughly 1).
    - o Trajectories obtained in this manner yield an estimate of 3-4°C for our overshoots/undershoots.

Figure D-4 – Determining temperature crossing points for 72°C stage
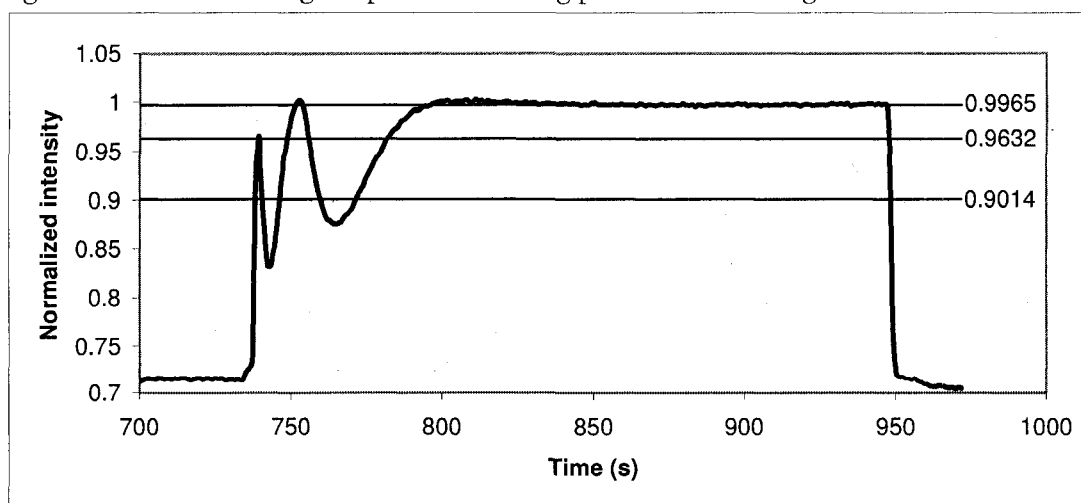
[III] MATLAB code for extracting TLC data

```
function AnTLC(N,h,r)
% extracts data from Ocean Optics spectrometer files, divides
  background, and extracts RGB relative intensities vs. time
% Ocean Optics spectrometer files are saved as "time.TimeAcquisition"
  (contains intensity vs. time) and "spectrum.time.xxxxx.Maser.Scope"
  (contains spectrum at each timepoint)
% N = number of optical spectra files to analyze
% h = number of lines to skip when extracting optical spectra
% r = number of lines to read when extracting optical spectra
% h and r define the range of wavelengths over which the optical
  spectra will be graphed
% Viet Hoang AML July 12, 2007

% default values (extracts all data)
if nargin < 3, r = 2048; end
if nargin < 2, h = 19; end

% getting time vector t (and total intensity I)
fid = fopen('time.TimeAcquisition');
t = textscan(fid, '%f %f', N, 'headerlines', 1);
fclose(fid);

% getting background
fid = fopen('spectrum.time.00000.Master.Scope');
b = textscan(fid, '%f %f', r, 'headerlines', h);
fclose(fid);

% getting spectra and normalizing changes to background
I = zeros(r,N);
for n=0:N-1
    filename = sprintf('spectrum.time.%05d.Master.Scope', n);
    fid = fopen(filename);
    data = textscan(fid, '%f %f', r, 'headerlines', h);
    fclose(fid);
    I(:,n+1) = data{:,2}./b{:,2};
end

% plotting normalized optical spectra changes over time
% [T, L] = meshgrid(t{:,1}, b{:,1});
% surf(T,L,I,'EdgeColor','none'), view(2), colorbar
% xlabel('Time (s)'), ylabel('Wavelength (nm)'), zlabel('Intensity')

%extracting red peak (averaged over ~15nm) over time
R = zeros(1,N);
for n=565:605
    R = R+I(n,:);
end
R = R/41;

%extracting green peak (averaged over ~15nm) over time
G = zeros(1,N);
for n=375:415
    G = G+I(n,:);
```

```
end
G = G/41;

%extracting blue peak (averaged over ~15nm) over time
B = zeros(1,N);
for n=120:160
     B = B+I(n,:);
end
B = B/41;

% plotting RGB peaks over time
plot(t{:,1}, B, t{:,1}, G, t{:,1}, R)

% recording data file
diary('AnTLC')
disp([t{:,1} B' G' R'])
diary off
```

Appendix E

Finite element modeling guide

The following describes the general methodology for simulating resistive heating and heat transfer in microfluidic devices using COMSOL Multiphysics 3.2:

1) Select the geometries and modes to be employed in the model using the "Multiphysics > Model Navigator" menu. For 2D axisymmetric models, only the General Heat Transfer mode (htgh) of the Heat Transfer Module is required. For 3D models with resistive heating, the Shell, Conductive Media DC mode (emdcsh) of the Electromagnetics Module is also required in addition to the htgh mode. After being selected, the "Multiphysics" menu can be used to switch between the two modes. These modes automatically define "T" as temperature, "V" as voltage, and "t" as time.

2) Draw the desired geometry of the model using the CAD tools provided. Merging and difference functions can be used to draw complex structures. For 3D models, it is useful to draw structures in a 2D geometry (included using the "Multiphysics > Model Navigator"), and then use the "Embed", "Extrude", and "Revolve" functions in the "Draw" menu to extrapolate them into 3D. The "Draw > Modify" menu also includes functions for readily translating, rotating, and scaling structures. Very thin structures (e.g. resistive element) should be drawn as a boundary to allow them to be meshed (dealt with in setting up boundary conditions). It should be noted that units in COMSOL Multiphysics are implicit and must be kept consistent by the user. All material properties and dimensions must have the same units. Therefore, for example, if the material properties use meters, the unit of length in the geometries drawn is also in meters.

3) The "Options > Constants" menu can be used define commonly used parameters/variables in the model (e.g. room temperature). In this manner, if the parameter must be adjusted, the user only needs to change the value in this menu. Similarly, the "Options > Expressions" menu can be used to define commonly used expressions in the model (e.g. resistivity of platinum as a function of temperature).

4) In the htgh mode (select using the "Multiphysics" menu), use the "Physics > Subdomain settings" menu to assign thermal properties (thermal conductivity, density, specific heat capacity, initial temperature) to the domains in the geometry. It is simplest to define groups (e.g. glass, PDMS), and then assign each domain the appropriate group. If the chamber is modeled as a domain, the properties of water are used. Thermal properties can be entered as expressions (e.g. dependence on temperature).

The mesh element type can be set in this menu as well. The element type used for the simulations in this thesis was the Lagrange Quadratic element, which is the default setting. Other element types are available and were tried (e.g. Lagrange Cubic and Lagrange Quartic), but they did not yield significantly different results (less than 1°C difference).

5) Use the "Physics > Boundary settings" menu to assign boundary conditions. Again, it is simplest to define groups and assign them to each boundary. Expressions can also be entered. A particularly useful function is flsmhs($t - t_0$, s), which is a smoothed Heaviside function (t_0 is the time at which the function switches, and s is the window over which smoothing is done). Boundary conditions used in this thesis included:

- Thermal insulation: Note that the "axial symmetry" option in 2D axisymmetric models is essentially the same as thermal insulation (i.e. no heat flow).
- Heat flux: Natural convection is included by entering the heat transfer coefficient and the ambient temperature. Radiation can be included by entering the emissivity and the ambient temperature (radiation is negligible for the temperatures considered in this thesis).
- Heat sink: A temperature boundary is used, set to the temperature of the heat sink.
- Continuity: Interior boundaries other than the resistive element and the chamber are set to continuous temperature.
- Chamber: In 3D models, if the chamber is modeled as a boundary, it is set to continuous temperature, and in addition, the "Highly conductive layer" tab is enabled and used to assign thermal properties (for water) as well as the thickness/height of the chamber (this mode assumes the temperature is constant across the thickness of the chamber). In 2D models, the chamber can be modeled as a domain (as in step 4) without greatly hindering meshing.
- Resistive element: In 3D models, the resistive element is modeled as a 2D boundary and therefore also requires enabling the "Highly conductive layer" tab to assign thermal properties (for platinum) and a thickness (temperature is again assumed constant across the thickness of the element). Additionally, to simulate resistive heating, the heat source term is set to "Q_emdcsh*d", where Q_emdcsh is the resistive heat generated per volume (a variable defined and calculated by the emdcsh mode) and d is the thickness of the resistive element. In 2D models, the resistive element is a 1D boundary with a set temperature (possibly time-varying).

6) For 3D models with resistive heating, in the emdcsh mode (select using the "Multiphysics" menu), use the "Physics > Boundary settings" menu to assign electrical properties (assign groups). This mode should be inactivated for all boundaries except the resistive element. For the resistive element, enter the conductivity (should be an expression that depends on temperature), its thickness, and its initial voltage.

7) Use the "Physics > Edge settings" menu to assign boundary conditions. All edges should be set to insulation except the two edges of the electrode pads. One edge of an electrode pad should be set to ground. The edge on the other electrode pad should be set to the desired applied voltage or current (enter as a current density).

8) Use the "Mesh > Mesh parameters" menu to change mesh settings. For the simulations in this thesis, the default values were used:

Parameter	2D model	3D model
Pre-defined mesh size	normal	normal
Size scaling	1	1
Element growth rate	1.3	1.4
Curvature factor	0.3	0.4
Curvature cut-off	0.001	0.01
Resolution of narrow region	1	1

9) Once all material properties and boundary conditions have been set, use the "Solve > Solver parameters" menu to define the solving method. For a steady-state solution, choose the stationary non-linear solver. For a time dependent solution, choose the time dependent solver and enter the range of times over which the model is to be solved (e.g. 0:1:120 will solve the model from 0 s to 120 s in steps of 1 s). Use the "Solve" button to mesh and solve the model. The relative tolerance (convergence criteria) used for the simulations in this thesis was the default value of 1e-6.

10) Use the "Post-processing" menu to analyze the results. COMSOL Multiphysics offers a wide variety of plotting tools, including videos, under the "Plot parameters" menu. The value plotted can be defined here (e.g. enter "T – 273" to plot temperatures in °C since T is in K). The slice plot is particularly useful in visualizing temperature distributions. Use the "Cross-section parameters plot" menu to graph the temperature along a defined line, or the temperature at a defined point over time. Use the "Domain plot parameters" menu to plot temperatures on boundaries in the model. For example, to obtain the temperature distribution along the length of the heater ring, include a circle in the model that runs along the middle of the heater ring, and use the "Domain plot parameters" menu to plot the temperature along this circle.

The following are examples of model M-files used to perform finite element analysis simulations of the PCR microchip using COMSOL Multiphysics 3.2

[I] 2D axisymmetric model (time dependent)
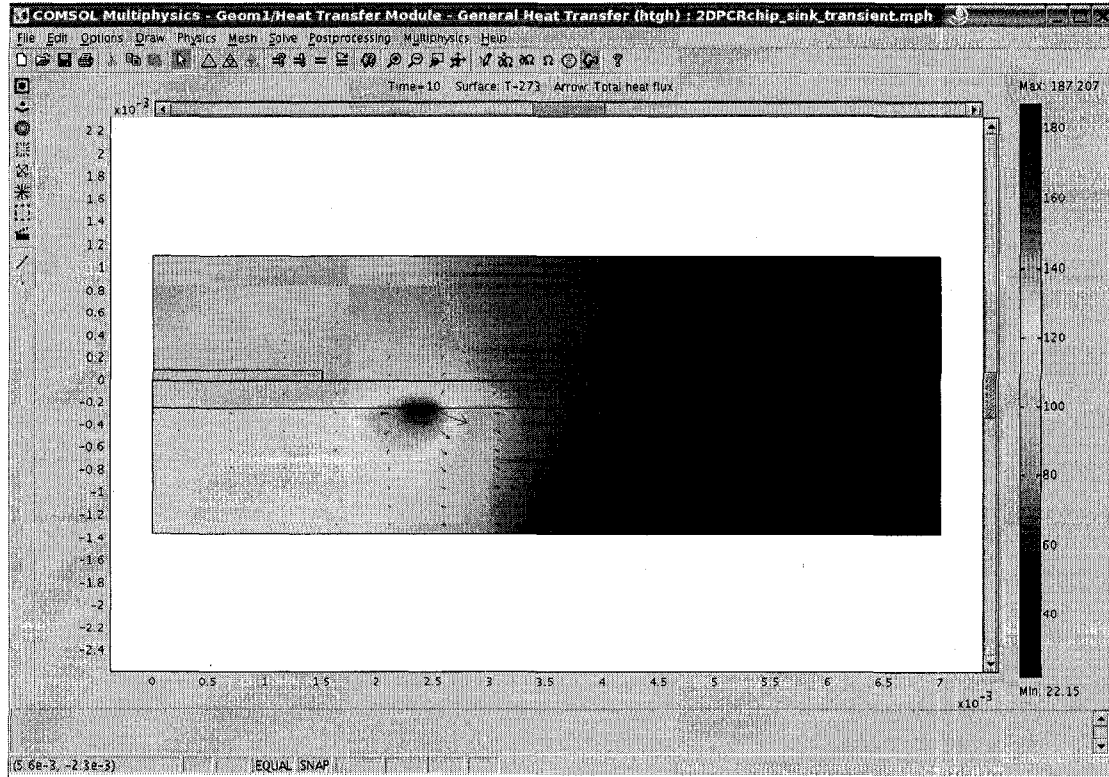

```
% COMSOL Multiphysics Model M-file
% Generated by COMSOL 3.2 (COMSOL 3.2.0.222, $Date: 2005/09/01 18:02:30 $)

flclear fem

% COMSOL version
clear vrsn
vrsn.name = 'COMSOL 3.2';
vrsn.ext = '';
vrsn.major = 0;
vrsn.build = 222;
vrsn.rcs = '$Name:    $';
vrsn.date = '$Date: 2005/09/01 18:02:30 $';
fem.version = vrsn;

% Geometry
g1=rect2('7e-3','1.1e-3','base','corner','pos',{'0','0'},'rot','0');
g2=rect2('7e-3','1.1e-3','base','corner','pos',{'0','-1.1e-3-254e-6'},'rot','0');
g3=rect2('7e-3','254e-6','base','corner','pos',{'0','-254e-6'},'rot','0');
g4=rect2('1.5e-3','90e-6','base','corner','pos',{'0','0'},'rot','0');
g5=curve2([0.0023,0.0025],[-2.54E-4,-2.54E-4]);
g6=curve2([0.0035,0.0070],[-0.001354,-0.001354]);
clear c s
c.objs={g5,g6};
c.name={'heater','sink'};
c.tags={'g5','g6'};
```

127

```
s.objs={g1,g2,g3,g4};
s.name={'top_glass','bottom_plate','membrane','chamber'};
s.tags={'g1','g2','g3','g4'};

fem.draw=struct('c',c,'s',s);
fem.geom=geomcsg(fem);

% Constants
fem.const = {'h_air','5.6', ...
   'Text','22+273.15', ...
   'Th','150+273.15', ...
   'time','10'};

% Initialize mesh
fem.mesh=meshinit(fem);

% (Default values are not included)

% Application mode 1
clear appl
appl.mode.class = 'GeneralHeat';
appl.mode.type = 'axi';
appl.module = 'HT';
appl.shape = {'shlag(1,''J'')','shlag(2,''T'')'};
appl.border = 'on';
appl.assignsuffix = '_htgh';
clear bnd
bnd.Tamb = {0,0,0,'Text','Text',0};
bnd.radType = {'none','none','none','surf2amb','none','none'};
bnd.type = {'ax','q0','cont','q','T','T'};
bnd.shape = 1;
bnd.h = {0,0,0,'h_air','h_air',0};
bnd.T0 = {273.15,273.15,273.15,'Text','Th*flsmhs(t,0.01)+(T-Th)*flsmhs(t-time,0.01)', ...
   'Text'};
bnd.Tinf = {273.15,273.15,273.15,'Text','Text',273.15};
bnd.epsilon = {0,0,0,1,1,0};
bnd.name = {'axial symmetry','insulated','continuous T','convection','heater - heating
and cooling', ...
   'heat sink'};
bnd.ind = [1,2,1,3,1,3,1,3,4,3,3,5,3,6,4,4,4];
appl.bnd = bnd;
clear equ
equ.k = {1.11,0.18,0.58};
equ.init = {{'Text';0}};
equ.shape = 2;
equ.name = {'borofloat glass','PDMS','water'};
equ.rho = {2200,1030,1000};
equ.C = {830,1100,4187};
equ.ind = [1,2,3,1];
appl.equ = equ;
fem.appl{1} = appl;
fem.sdim = {'r','z'};
fem.border = 1;
fem.outform = 'general';
fem.units = 'SI';

% Descriptions
clear descr
descr.const= {'time','duration of heating stage','Text','ambient
temperature','h_air','heat transfer coefficient for natural convection in
air','Th','heater temperature during heating stage'};
fem.descr = descr;

% Multiphysics
fem=multiphysics(fem);

% Extend mesh
fem.xmesh=meshextend(fem);
```

```
% Evaluate initial value using current solution
init = asseminit(fem,'u',fem0.sol);

% Solve problem
fem.sol=femtime(fem, ...
                'init',init, ...
                'solcomp',{'T'}, ...
                'outcomp',{'T'}, ...
                'tlist',[0:0.01:60], ...
                'tout','tlist');

% Save current fem structure for restart purposes
fem0=fem;

% Plot solution
postplot(fem, ...
        'tridata',{'T-273.15','cont','internal'}, ...
        'trimap','jet(1024)', ...
        'arrowdata',{'tflux_r_htgh','tflux_z_htgh'}, ...
        'arrowxspacing',15, ...
        'arrowyspacing',15, ...
        'arrowtype','arrow', ...
        'arrowstyle','proportional', ...
        'arrowcolor',[1.0,0.0,0.0], ...
        'solnum','end', ...
        'title','Time=60    Surface: T-273.15    Arrow: Total heat flux [W/m^2]', ...
        'refine',3, ...
        'axis',[-3.50000010803342E-4,0.00735000022687018,-
0.0025269454082283,0.00227294556962277,-1,1]);

% Plot solution
postplot(fem, ...
        'tridata',{'T-273.15','cont','internal'}, ...
        'trimap','jet(1024)', ...
        'arrowdata',{'tflux_r_htgh','tflux_z_htgh'}, ...
        'arrowxspacing',15, ...
        'arrowyspacing',15, ...
        'arrowtype','arrow', ...
        'arrowstyle','proportional', ...
        'arrowcolor',[1.0,0.0,0.0], ...
        'solnum',1001, ...
        'title','Time=10    Surface: T-273.15    Arrow: Total heat flux [W/m^2]', ...
        'refine',3, ...
        'axis',[-3.50000010803342E-4,0.00735000022687018,-
0.0025269454082283,0.00227294556962277,-1,1]);

% Plot in cross-section or along domain
postcrossplot(fem,0,[0;45e-6], ...
                'pointdata','T-273.15', ...
                'title','T-273.15', ...
                'axislabel',{'Time','T-273.15'});
```
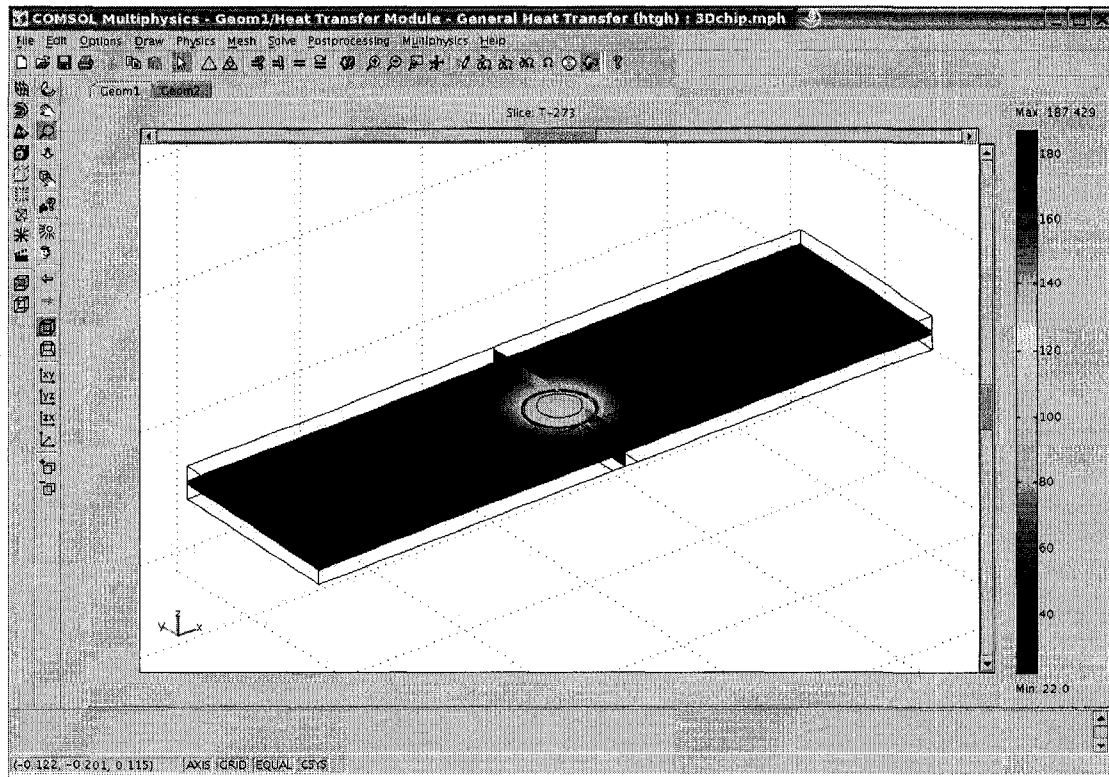
129

[II] 3D model (steady-state)


```
% COMSOL Multiphysics Model M-file
% Generated by COMSOL 3.2 (COMSOL 3.2.0.222, $Date: 2005/09/01 18:02:30 $)

flclear xfem

% COMSOL version
clear vrsn
vrsn.name = 'COMSOL 3.2';
vrsn.ext = '';
vrsn.major = 0;
vrsn.build = 222;
vrsn.rcs = '$Name:  $';
vrsn.date = '$Date: 2005/09/01 18:02:30 $';
xfem.version = vrsn;

% Constants
xfem.const = {'h_air','5.6', ...
  'Text','22+273.15', ...
  'd','200e-9', ...
  'geom','5e-8/(6*pi)', ...
  'slope','0.15', ...
  'intercept','66.7'};

% Geometry 2
g1=rect2('50e-3','14e-3','base','center','pos',{'0','0'},'rot','0');
g2=circ2('1.5e-3','base','center','pos',{'0','0'},'rot','0');
g3=circ2('2.3e-3','base','center','pos',{'0','0'},'rot','0');
g4=circ2('2.4e-3','base','center','pos',{'0','0'},'rot','0');
g5=circ2('2.5e-3','base','center','pos',{'0','0'},'rot','0');
g6=circ2('3.5e-3','base','center','pos',{'0','0'},'rot','0');
g7=rect2('2e-3','5e-3','base','corner','pos',{'-1e-3','-7e-3'},'rot','0');
g8=geomcomp({g6,g7},'ns',{'g6','g7'},'sf','g6+g7','edge','none');
g9=geomdel(g8);
```

```
g10=rect2('0.2e-3','0.5e-3','base','corner','pos',{'-0.1e-3','-2.6e-3'},'rot','0');
g11=rect2('0.4e-3','0.2e-3','base','corner','pos',{'0.1e-3','-2.6e-3'},'rot','0');
g12=rect2('0.4e-3','0.2e-3','base','corner','pos',{'-0.5e-3','-2.6e-3'},'rot','0');
g13=rect2('6e-3','4.4e-3','base','corner','pos',{'0.1e-3','-7e-3'},'rot','0');
g14=rect2('6e-3','4.4e-3','base','corner','pos',{'-6.1e-3','-7e-3'},'rot','0');
g15=geomcomp({g5,g3},'ns',{'g5','g3'},'sf','g5-g3','edge','none');
g16=geomcomp({g15,g10},'ns',{'g15','g10'},'sf','g15-g10','edge','none');
g17=geomcomp({g11,g12,g13,g14,g16},'ns',{'g11','g12','g13','g14','g16'},'sf','g11+g12+g13
+g14+g16','edge','none');
g18=geomdel(g17);
gg=geomedit(g18);
gg([6])={[]};
gg([9])={[]};
gg([11])={[]};
gg([5])={[]};
gg([7])={[]};
gg([12])={[]};
gg{8}=beziercurve2([-1.0E-4,-1.0E-4],[-0.0070,-0.00229782505861521],[1,1]);
gg{13}=beziercurve2([1.0E-4,1.0E-4],[-0.0070,-0.00229782505861521],[1,1]);
g19=geomedit(g18,gg);
g20=extrude(g1,'distance',[2.2e-3+254e-
6],'scale',[1;1],'displ',[0;0],'twist',[0],'face','none','wrkpln',[0 0.001354 0;0 0
0.001354;-0.001354 -0.001354 -0.001354]);
g21=embed(g9,'Wrkpln',[0 0.001354 0;0 0 0.001354;-0.001354 -0.001354 -0.001354]);
g22=embed(g19,'Wrkpln',[0 2.54E-4 0;0 0 2.54E-4;-2.54E-4 -2.54E-4 -2.54E-4]);
g23=embed(g4,'Wrkpln',[0 2.54E-4 0;0 0 2.54E-4;-2.54E-4 -2.54E-4 -2.54E-4]);
g24=extrude(g1,'distance',[254e-
6],'scale',[1;1],'displ',[0;0],'twist',[0],'face','none','wrkpln',[0 2.54E-4 0;0 0 2.54E-
4;-2.54E-4 -2.54E-4 -2.54E-4]);
g25=embed(g2,'Wrkpln',[0 1 0;0 0 1;0 0 0]);

% Geometry 1
flclear fem
clear f s
f.objs={g21,g22,g23,g25};
f.name={'EMB1','EMB2','EMB3','EMB4'};
f.tags={'g21','g22','g23','g25'};

s.objs={g20,g24};
s.name={'EXT1','EXT2'};
s.tags={'g20','g24'};

fem.draw=struct('f',f,'s',s);
fem.geom=geomcsg(fem);

% Initialize mesh for geometry 1
fem.mesh=meshinit(fem);
xfem.fem{1}=fem;

% (Default values are not included)

fem=xfem.fem{1};

% Application mode 1
clear appl
appl.mode.class = 'GeneralHeat';
appl.module = 'HT';
appl.shape = {'shlag(1,''J'')','shlag(2,''T'')'};
appl.border = 'on';
appl.assignsuffix = '_htgh';
clear prop
prop.analysis='static';
appl.prop = prop;
clear bnd
bnd.rhos = {8700,8700,8700,21500,8700,1000};
bnd.ks = {400,400,400,72,400,0.58};
bnd.Tamb = {'Text',0,0,0,0,0};
bnd.radType = {'surf2amb','none','none','none','none'};
bnd.type = {'q','T','cont','dq','q0','cont'};
bnd.shape = 1;
```

```
bnd.h = {'h_air',0,0,0,0,0};
bnd.Cs = {385,385,385,133,385,4187};
bnd.T0 = {273.15,'Text',273.15,273.15,273.15,273.15};
bnd.Tinf = {'Text',273.15,273.15,'Text',273.15,273.15};
bnd.q0 = {0,0,0,'Q_emdcsh*d',0,0};
bnd.ds = {0,0,0,'d',0,90e-6};
bnd.epsilon = {1,0,0,0,0,0};
bnd.name = {'natural convection','heat sink','continuous T','heater','insulated', ...
    'chamber'};
bnd.hclOn = {0,0,0,1,0,1};
bnd.ind = {1,1,2,1,1,3,1,1,3,1,1,1,1,4,5,4,3,6,3,1,1,1};
appl.bnd = bnd;
clear equ
equ.k = {1.11,0.18};
equ.init = {{'Text';0}};
equ.shape = 2;
equ.name = {'glass','PDMS'};
equ.rho = {2200,1030};
equ.C = {830,1100};
equ.ind = [1,2,1];
appl.equ = equ;
fem.appl{1} = appl;

% Application mode 2
clear appl
appl.mode.class = 'CondMediaShell';
appl.module = 'EM';
appl.assignsuffix = '_emdcsh';
clear prop
clear weakconstr
weakconstr.value = 'off';
weakconstr.dim = {'lm2'};
prop.weakconstr = weakconstr;
appl.prop = prop;
clear bnd
bnd.d = {1,'d'};
bnd.sigma = {5.99e7,'1/rho'};
bnd.usage = {0,1};
bnd.name = {'inactive','heater'};
bnd.ind = [1,1,1,1,1,1,1,1,1,1,1,1,1,2,1,2,1,1,1,1,1,1];
appl.bnd = bnd;
clear edg
edg.V0 = {0,0,0,13.5};
edg.Jn = {0,0,'150/4.4',0};
edg.type = {'nJ0','V0','nJ','V'};
edg.name = {'insulation/continuity','ground','applied current','applied voltage'};
edg.ind = [1,1,1,1,1,1,1,1,1,1,1,1,1,1,1,1,1,1,4,1,1,1,1,1,1,1,1,1,1, ...
    1,1,1,1,1,1,1,1,1,1,1,1,1,1,1,1,1,1,1,1,1,1,1,1,2,1,1,1,1,1,1,1, ...
    1,1,1];
appl.edg = edg;
fem.appl{2} = appl;
fem.border = 1;
fem.outform = 'general';
fem.units = 'SI';

% Global expressions
fem.expr = {'rho','geom*(slope*(T-Text)+intercept)'};
xfem.fem{1} = fem;

flclear fem
fem.sdim = {'x','y'};
fem.border = 1;
fem.units = 'SI';

% Global expressions
fem.expr = {'rho','geom*(slope*(T-Text)+intercept)'};
xfem.fem{2} = fem;

% Descriptions
clear descr
```

```
descr.const= {'geom','A/L geometrical factor for resistive element','d','thickness of
resistive element','slope','slope of R vs. T relationship','Text','external room
temperature','h_air','heat transfer coefficient for natural convection in
air','intercept','intercept of R vs. T relationship'};
xfem.descr = descr;

% Multiphysics
xfem=multiphysics(xfem);

% Extend mesh
xfem.xmesh=meshextend(xfem,'geoms',[1]);

% Solve problem
xfem.sol=femnlin(xfem, ...
                'solcomp',{'T','V'}, ...
                'outcomp',{'T','V'}, ...
                'linsolver','gmres', ...
                'prefun','amg');

% Save current fem structure for restart purposes
fem0=xfem;

% Plot solution
postplot(xfem, ...
        'slicedata',{'T-273.15','cont','internal'}, ...
        'slicexspacing',1, ...
        'sliceyspacing',0, ...
        'slicezspacing',[0 -254e-6], ...
        'slicemap','jet(1024)', ...
        'title','Slice: T-273.15', ...
        'refine',2, ...
        'grid','on', ...
        'campos',[-13.7022605208766,-17.8571335760868,12.9825448112317]);

% Geometry 2
fem=xfem.fem{2};
clear s
s.objs={g1,g2,g4,g9,g19};
s.name={'R1','C1','C3','CO2','CO3'};
s.tags={'g1','g2','g4','g9','g19'};

fem.draw=struct('s',s);
xfem.fem{2}=fem;
```

Appendix F

Further scaling considerations

Here, finite element modeling is used to explore the expected outcomes of miniaturizing the thermal management system in different manners (modified versions of the models in the FE_models/ folder in the supplementary data DVD).

[I] Maintaining the same microchip layer thicknesses

Section 5.6.1 showed that scaling all dimensions of the developed thermal management system can be highly advantageous. However, thinning the layers of the microchip may not be a readily available option (particularly the PDMS membrane). As a result, scaling the system while maintaining the current microchip layer thicknesses was explored.

The radii of the reaction chamber and the resistive element were halved, keeping the height of the chamber the same (to avoid increasing the surface area to volume ratio, and also because shallower chambers are more prone to air bubble formation and trapping). However, to avoid substantially affecting the heating rate, the position of the heat sink could not simply be halved like when microchip layer thicknesses are also halved, and had to be maintained at least ~2.5 mm away from the center of the reaction chamber. The size of the thermal module therefore cannot be reduced as much as in the first scenario where the microchip layer thicknesses are also scaled.

Furthermore, because the area heated by the resistive element relative to the microchip volume it must heat is now much smaller, a higher temperature is required on the resistive element to maintain a given temperature in the reaction chamber. As shown in chapter 2 (Figure 2-4b), for the microchip layer thicknesses considered, the original resistive element size (outer radius of 2.5 mm) had been closer to the optimal case which minimized the temperature required on the resistive element to maintain a given temperature at the middle of the reaction chamber. In order to ensure the operating temperature of the thermal

module would not exceed the melting point of PDMS (~220°C), simulations showed that the heat sink position had to be moved back to being 3.5 mm from the center of the reaction chamber (same position as in the original design presented in chapter 4). At this spacing and with the radii of the reaction chamber and resistive element halved, simulations showed that a temperature of ~200°C is required on the resistive element to maintain ~95°C in the reaction chamber. The size of the thermal module (i.e. the heated volume) therefore does not change significantly, and thus its equilibration time remains ~20 s. Nevertheless, the power consumption of the system is still halved, requiring ~1 W to maintain ~95°C in the reaction chamber.

[II] Using thinner glass layers

In an attempt to lower the operating temperature of the resistive element, another scenario was considered where 500 μm thick glass layers are employed with same PDMS thickness (thinner glass is readily available, but not thinner PDMS). Again, the radii of the reaction chamber and the resistive element were halved. The thinner glass ensures that the microchip size scales down somewhat along with the resistive element. In this manner, the area heated by the element relative to the microchip volume it must heat does not decrease as drastically as in the previous scenario. Simulations showed that to avoid substantial reductions in heating rate, the heat sink has to be located ~2.5 mm from the center of the chamber.

In this scenario, a temperature of ~160°C is required on the resistive element to maintain ~95°C in the reaction chamber. The operating temperature of the resistive element is therefore lower than in the second scenario, as expected. The power consumption and the equilibration time are reduced as well, requiring ~0.75 W to maintain 95°C in the reaction and reaching steady-state in ~10 s after a step response. Compared to the scenario in section 5.6.1 where the PDMS thickness is scaled too, this case provides a lower power consumption, but a longer equilibration time.

However, unlike in the first two scenarios, the temperature uniformity in the reaction chamber was not maintained, varying by ~3°C across the radius of the chamber. To keep temperature variations in the chamber smaller than ~1°C, two approaches could be taken. First, the radius of the reaction chamber could be halved further (reduced by a factor of 4 from the original) so that it remains within the region where the temperature does not vary by more than 1°C. However, if the chamber cannot be shrunk further (e.g. to ensure enough starting template is present for PCR), the resistive element (along with the heat sink position) would have to be moved further away from the chamber, but this second approach defeats the original purpose of miniaturizing the thermal module.

In summary, the results obtained for scaling down the thicknesses of all microchip layers (section 5.6.1) are better than the two cases presented above. Both power consumption and equilibration time are improved, but spatial temperature profiles are not altered. The two cases here show that the thicknesses of microchip layers have a very substantial effect on the heat transfer within the microchip, and hence cannot be ignored when scaling down the geometry. It is better to scale all three dimensions and not just in two dimensions (though the above cases are still provide some advantages).

[III] Plastic-based microchips

Another option to consider is the use of plastic-based microchips as opposed to glass-based ones. Plastic-based microchips can be much less expensive than glass-based ones since they can be fabricated using much simpler processes (e.g. injection molding or hot embossing as opposed to etching), making them perhaps more suitable for making disposable microchips. However, the thermal conductivity of plastics tends to be much lower than that of glass, inherently leading to slower thermal transitions and a larger gap between the temperatures at the chamber and at the resistive element. Nonetheless, the lower thermal conductivity may be counteracted by using thinner layers, which are also more readily available for plastics. The heat transfer and optimal geometries for plastic-based microchips still needs much further characterization.

The patterning of resistive elements onto plastic may also be difficult or problematic (e.g. thin film does not adhere well, or plastic cannot withstand deposition temperatures). Additionally, the cost of patterning resistive elements may be too high for producing disposable microchips (though this cost is reduced if thermal modules are miniaturized to increase fabrication throughput). An alternative would be to use disposable plastic-based microchips with an external Peltier element instead of integrating a microheater in the chip to reduce its fabrication cost. The Peltier element would also readily allow active cooling for faster cooling rates. However, Peltier elements are not as amenable for portable and inexpensive platforms since they are power intensive (e.g. require an applied current on the range of amps) and not as readily scalable. Having the heating element external to the microchip may also lead to problems with poor thermal contact between the two. Hence, in the context of developing complex microchips that require many independent thermal modules, thin film resistive elements remain more advantageous (particularly when miniaturizing further).

Appendix G

List of data in manuscripts

The work presented in this thesis has led to three manuscripts. The following lists the data included in each of these manuscripts. Related raw data files, COMSOL files, and reports can be found in the supplementary data DVD (VNH_thesis/thesis_data/ with references, including μTK timestamps, to other folders such as uTK_data/ and FE_models/). Also included in the supplementary data DVD are the manuscripts themselves, related conference posters/presentations, lab reports and presentations, references, programs, protocols, mask designs, and TTK related files. Text files throughout the DVD contain more detailed descriptions and notes regarding the contents.

[I] V. N. Hoang, G. V. Kaigala, C. J. Backhouse, "Thermal management in microfluidic lab-on-a-chip devices using a single resistive element approach." Manuscript in preparation.
- Figure 2-1b) & c)
- Figure 2-2
- Figure 2-5
- Figure 2-6
- Figure 2-7
- Table 2-1

[II] V. N. Hoang, G. V. Kaigala, C. J. Backhouse, "Dynamic temperature measurement in microfluidic devices using thermochromic liquid crystals." Accepted for publication in *Lab on a Chip*, December 2007.
- Figure 3-1
- Figure 3-3
- Figure 3-4
- Table 3-1
- Table 3-2

[III] V. N. Hoang, G. V. Kaigala, A. Atrazhev, L. M. Pilarski, C. J. Backhouse, "Practical strategies for enhancing the speed of microchip genetic amplification implementations." Manuscript in preparation.

- Figure 4-1
- Figure 4-2
- Figure 4-4
- Figure 4-6
- Figure 4-7
- Table 4-1